MULTIMODE INPUT FOR ENHANCED DISSIPATIVE SENSING IN WHISPERING-GALLERY MICRORESONATORS

By

SREEKUL RAJ RAJAGOPAL

Bachelor of Science in Physics
Kannur University
Kannur, Kerala
2010

Master of Science in Physics
Oklahoma State University
Stillwater, Oklahoma
2020

Submitted to the Faculty of the
Graduate College of the
Oklahoma State University
in partial fulfillment of
the requirements for
the Degree of
DOCTOR OF PHILOSOPHY
May, 2021

MULTIMODE INPUT FOR ENHANCED

DISSIPATIVE SENSING IN WHISPERING-GALLERY

MICRORESONATORS

Dissertation Approved:

Dr. Albert T. Rosenberger

Dissertation Adviser

Dr. Gil Summy

Dr. Mario F. Borunda

Dr. James C. West

ACKNOWLEDGEMENTS

First of all, my sincere thanks to everyone at Oklahoma State University who has helped me throughout this long and exciting journey of learning. I would like to thank my family, friends, and everyone at the Department of Physics for their encouragement and support throughout these years.

I would like to thank my advisor Dr. Albert T. Rosenberger for being patient with me and helping me throughout these years. No words are enough to express my gratitude towards him. During these years, I have learnt a lot from him. His broad spectrum of knowledge in various disciplines, ability to build model with minimum parameters, and expertise in the field of microresonators is the basis of this dissertation.

Next I would like to thank my committee members: Dr. Mario Borunda, Dr. James C. West and Dr. Gil Summy for their valuable suggestions and guidance. I would also like to thank everyone in my lab: Dr. Khoa V. Bui for teaching me the experimental techniques; Dr. Limu Ke for being the best colleague and encouraging me throughout my work; Karleyda Sandoval for her help in setting up a Python program which makes the data analysis a lot simpler; Mohmad Junaid ul Haq for his generous support in the lab. In addition, I would like to thank the amazing staff of the Physics Department Susan Cantrell, Alisha Leach, Tamra Raymond, Elizabeth Bridenstine, Megan Treanor, Melissa Edwards and Warren Grider.

I would like to thank my mother (Geetha M. K), father (A. C. Rajagopalan), and my brother (Dr. Gokul Raj R) who stood with me throughout my life. Special thanks to my wife (Amrutha Kottath) and my daughter (Sritha Sreekul) for their unconditional love and support.

Finally, I would like to thank all the teachers who taught me to date. Special thanks to Dr. K. V. Devadasan, Sandhya teacher, and Dr. Ramesh Babu who has inspired me to pursue my dream.

Name: SREEKUL RAJ RAJAGOPAL

Date of Degree: MAY, 2021

Title of Study: MULTIMODE INPUT FOR ENHANCED DISSIPATIVE SENSING IN WHISPERING-GALLERY MICRORESONATORS.

Major Field: PHOTONICS

Abstract: In this dissertation, we demonstrate a novel sensing technique for enhancing the sensitivity of dip-depth based dissipative sensing. First, we introduce two different sensing techniques (dispersive and dissipative) related to sensors based on optical whispering gallery mode (WGM) microresonators and show analytically that in an adiabatic tapered fiber coupled microresonator system, where a single mode is incident on the microresonator, the dissipative sensing based on the dip depth change can provide better sensitivity than dispersive sensing based on frequency shift measurements. However, the sensitivity can be further improved by making multiple fiber modes incident on the microresonator using an asymmetric tapered fiber. Next, the process of fabricating of asymmetric tapered fiber is explained and then an empirical model which predicts the radius of the fabricated asymmetric tapered fiber is developed. Based on the beat length measurements, the empirical model is validated and the correct delineation curve which determines the adiabaticity criteria is decided. Next, a simplified model which explains the behavior of an asymmetric tapered fiber coupled microresonator system is developed. Based on two experimentally determined input parameters, the model predicts the enhancement factor. In addition, the model allows us to compare the two dissipative sensing mechanisms, (based on fractional change in linewidth and fractional change in dip depth) and the absolute sensitivity of an asymmetric tapered fiber coupled microresonator system with multiple modes incident on the microresonator to the absolute sensitivity of an ideal adiabatic tapered fiber coupled microresonator system with a single mode incident on the microresonator. Finally, we show the experimental results which validate our model predictions; three orders of magnitude enhancement in dip depth sensing, two orders of magnitude more sensitivity in the dip depth based dissipative sensing signal compared to dissipative sensing signal based on the relative change in the linewidth, and the absolute sensitivity of an asymmetric tapered fiber coupled microresonator system with a quality factor (Q~10^7) is found to be comparable to the absolute sensitivity of an ideal adiabatic tapered fiber coupled microresonator system with a Q approximately equal to 10^9.

TABLE OF CONTENTS

Chapter Page

LIST OF TABLES

Table Page

LIST OF FIGURES

Figure Page

Figure Page

Figure Page

CHAPTER I

INTRODUCTION

1.1. Whispering-gallery mode sensors

Optical whispering-gallery mode (WGM) microresonators have proven their ability to enhance light-matter interaction and hence have been widely used for sensing various physical quantities. Owing to their high sensitivities and low detection limits, chemical sensors based on optical whispering gallery mode microresonators enable the detection of various chemicals and, thereby, are of great importance for many practical applications such as environmental monitoring. From an operational point of view, most optical WGM sensors are based on either the shift in resonant mode frequency (dispersive) or change in the linewidth (dissipative) of the mode of interest. However, previously it was demonstrated that WGM sensors based on the relative change in the resonant throughput dip depth (dissipative) could offer better sensitivity under certain conditions while being more immune to environmental perturbations. In this dissertation, we propose and demonstrate a novel method for enhancing the sensitivity of resonant throughput dip depth based dissipative sensing. Traditionally a symmetric (adiabatic) tapered fiber is used to couple light into a microresonator and hence a single fiber mode is incident on the microresonator.

An enhancement in dip depth sensitivity by approximately three orders of magnitude is achieved by having multiple modes incident on a microresonator using an asymmetric (non-adiabatic) tapered fiber. In addition, with the multimode input, the dissipative sensing signal based on the relative change in throughput dip depth was found to be approximately 40-100 times (nearly two orders of magnitude) more sensitive than the dissipative sensing signal based on the relative change in the linewidth. In general, the absolute sensitivity of a tapered fiber coupled microresonator system will depend on the interacting WGM mode fraction *f* and the quality factor *Q* of the WGM. For an ideal adiabatic tapered fiber coupled microresonator system where a single fiber mode is incident on the microresonator, in order to have equal absolute sensitivity with that of the absolute sensitivity of an asymmetric tapered fiber coupled microresonator, the minimum intrinsic quality factor Q_i needs to be approximately of the order of 10^9 which is extremely hard to achieve in a fused silica microresonator without taking any extraordinary measures.

During the past few decades, the photonics industry has witnessed a revolution in terms of new materials and devices which can enhance the light-matter interaction. The devices which allow confinement of light into small volumes have become vital parts of any photonics design. Whispering gallery mode based optical dielectric resonators are devices with tiny mode volume, very narrow linewidth, and a high power density. Hence these devices have been attracting scientists from various disciplines. In 1910, Lord Rayleigh first explained WGMs for the sound waves at St. Paul's Cathedral in London [1]. A bit earlier, in 1909, the equations for resonant eigenfrequencies of free metallic and dielectric spheres were derived by Debye [2]. A study by R. D. Richtmyer [3] in 1939 pointed out the possibility of the existence of modes with high quality (*Q*) factor in axially symmetric open dielectric resonators. In 1961, the first experimental observation of optical whispering gallery modes was reported in a spherical sample of CaF_2: Sm^{++} [4]. Revolutionary work on fabricating a microresonator (silica microsphere) which can support WGMs with high *Q*, was demonstrated in 1989 by Braginsky, Gorodetsky and Ilchenko [5]. This

work stimulated a series of rigorous scientific explorations of WGM microresonators which eventually led to the development of various cutting edge technologies based on WGM microresonators.

The light coupled into a microresonator will be confined, and it will circulate along the circumference of the microresonator by successive total internal reflections. Resonances are achieved when the effective path length is equal to an integral number of wavelengths. These resonances are the whispering gallery modes.

Optical resonators are devices which trap the light in such a way that light can travel in a closed path. They are among the major components of lasers, some interferometers, and optical parametric oscillators. Optical resonators are designed and fabricated in such a manner that they have a significant quality factor, Q. The quality factor is defined as 2π times the ratio of stored energy to energy loss per optical period. There are different types of whispering gallery microresonators, based on the geometry of the resonator, as shown in Fig. 1.1. They are mainly classified as microspheres, microtoroids, microdiscs, microrings, bottle resonators, hollow bottle resonators, and microbubble resonators.

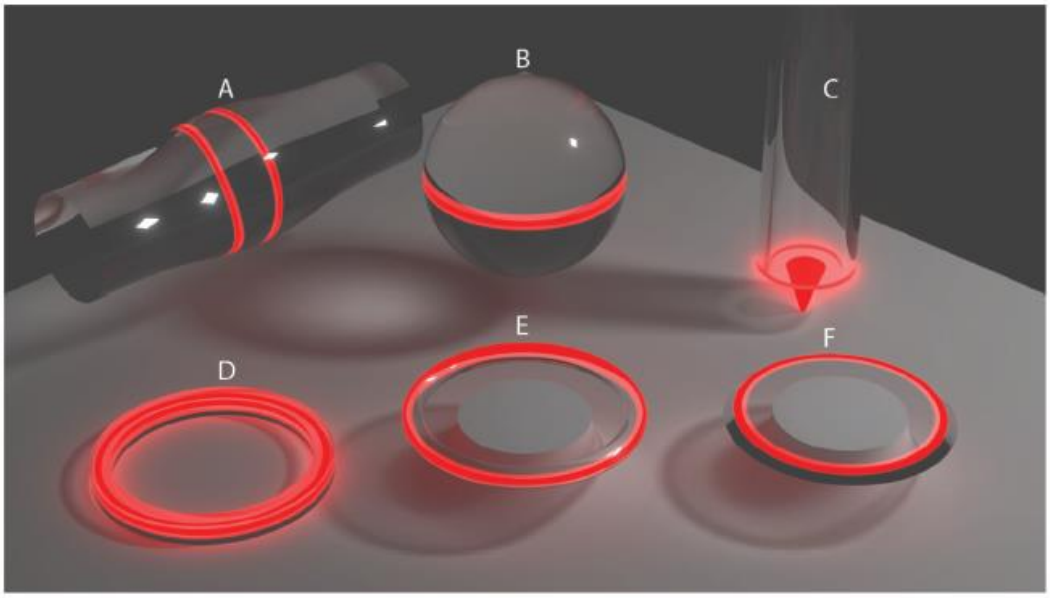

Figure 1.1. Different types of WGM microresonators. A) Microbottle, B) Microsphere, C) Fabry-Perot, D) Microring, E) Microtoroid, F) Microdisk [6].

One significant application of optical resonators is *sensing*. The hollow bottle resonator (HBR) was identified as a good candidate for sensing purposes [7-9]. WGMs inside an HBR can be defined in terms of three mode numbers *m, p, q,* and the polarization of the mode, TE for polarization parallel to the surface (axial direction) and TM for polarization normal to the surface (radial direction). The azimuthal mode number *m* specifies the number of wavelengths around the equator of the HBR. The mode number *p* represents the number of intensity maxima along the radial direction. The mode number *q* specifies the number of field nodes in the axial direction. The radial field distribution of the fundamental WGM of an HBR is shown in Fig. 1.2. Many of these resonators employ the technique of evanescent coupling to couple light into and out of the WGMs of the resonator. In addition to enabling the coupling of light into and out of the WGMs of the

microresonator, the evanescent fraction of a WGM also enables the interaction of light with the surrounding medium.

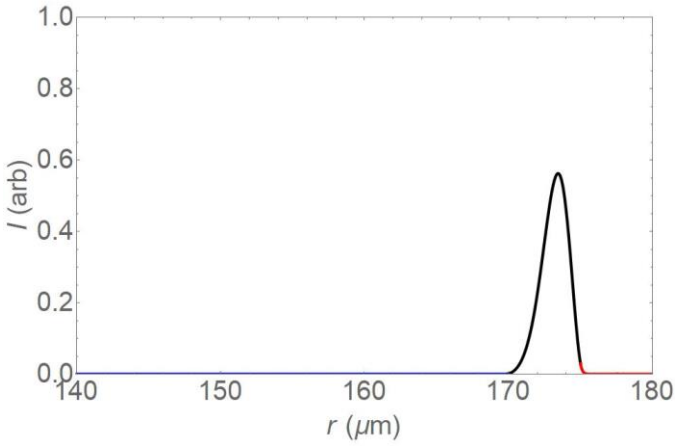

Figure 1.2. The radial intensity distribution of the fundamental TE ($p = 1, q = 0$) WGM of an HBR. Here the wavelength λ = 1550 nm, the outer boundary is at 175 μm, and the inner boundary is at 170 μm. The red (external) portion of the profile is nonzero near the outer boundary, representing the external evanescent fraction. The blue (internal) portion is zero so there is no internal evanescent fraction in this case.

Tapering an optical fiber to a diameter of few microns or less provides an efficient way to couple light into whispering gallery mode resonators. The coupling of light is made possible by using the evanescent fractions of fiber modes of a tapered optical fiber. Light injected at one end of the tapered fiber from a frequency scanned diode laser is evanescently coupled into WGMs of a microresonator, and the throughput spectrum is detected at the other end. A Lorentzian dip with finite linewidth $(\Delta\upsilon)$ is observed in the throughput spectrum corresponding to each excited WGM. The linewidth of a dip is proportional to the total round-trip loss suffered by light circulating in that WGM. There are two types of loss, namely intrinsic and extrinsic loss. The former includes surface scattering, absorption, and radiation loss whereas coupling loss is the extrinsic loss. The fractional dip depth M depends on the ratio of extrinsic loss to intrinsic loss.

In general, fiber tapers can be broadly classified as adiabatic or non-adiabatic [10]. If the light propagating in the tapered fiber remains in the local fundamental mode at any point along the taper transition, then such a taper is known as an adiabatic taper; however, for a non-adiabatic taper, in addition to the local fundamental mode, higher order fiber modes are also excited, and hence light gets distributed among local fundamental and higher order modes as it travels along the tapered fiber. Different fiber modes will have different spatial profiles, different evanescent fractions, different effective indices, and different propagation constants [11-14]. The throughput spectral profile of a resonator mode is no longer a symmetric Lorentzian dip when a non-adiabatic tapered fiber (or multimode waveguide) is used for coupling light to a microresonator [15-21]. The throughput spectral profile depends on the relative strength and phase of the fiber modes as they couple into a single resonator mode.

WGM based optical sensors are highly sensitive because of their high quality factors and small mode volumes. In recent times, WGM based optical sensors have been used for sensing various quantities [22-24] such as pressure, temperature, weak force, chemicals, biomolecules, magnetic field, electric field, and so on. From the operational point of view, optical WGM sensors detect through the registration of changes in their spectral response due to perturbations in the surrounding environment. The sensing mechanism of an optical WGM sensor can be categorized as dispersive or dissipative. Dispersive sensing relies on measuring the shift in WGM resonance frequency with a change in the refractive index of the surrounding medium [25-28]. Dissipative sensing is predominantly studied by monitoring the change in linewidth [29-31] of a WGM induced by a lossy (absorbing) analyte. However, in addition to the change in linewidth, the introduction of a lossy analyte into the surrounding environment of an optical WGM sensor will also induce a change in the resonant throughput dip depth. Thus a comprehensive study on dissipative sensing can be performed by detecting the change in the resonant throughput dip depth of a WGM [32,33].

Previously it was shown that under certain conditions the response to dissipative sensing based on change in relative dip depth can be more sensitive than dispersive response [34]. However, the sensing protocol of most of the optical WGM mode sensors has been dispersive. Lately, studies on dissipative sensing based on the transmittance dip for two different configurations, a waveguide side coupled to a circular microresonator [35] and self-interference microring resonator [36-39] has once again attracted scientific interest due to their potential to achieve better results than dispersive sensing. In all dissipative sensing configurations discussed to date, the input to the microresonator consists of a single waveguide mode or fiber mode. In this dissertation, we demonstrate, both theoretically and experimentally, a novel method for enhancing the sensitivity of resonant transmittance dip based dissipative sensing using multimode input to the microresonator. The enhancement demonstrated in this dissertation is relative to the change in resonant transmission dip depth that would be observed if only one fiber or waveguide mode were incident on the microresonator.

1.2. Dissertation organization

An outline of this dissertation is as follows. In the rest of Chapter 1, an overview of WGM based sensing is provided, especially absorption sensing using an adiabatically tapered fiber where only the fundamental fiber mode is incident on the microresonator.

In Chapter II, a detailed discussion about adiabatic and non-adiabatic tapered fibers is provided. The use of non-adiabatic tapered fibers to couple light into the microresonator is the highlight of all the experiments described in this dissertation. Hence an empirically useful treatment of design of the non-adiabatic tapered fiber is presented. Chapter III sets out to provide a theoretical framework for calculating the enhancement in sensitivity and a computational model of a non-adiabatic (asymmetric) tapered fiber coupled microresonator system. The computational model depends only on three parameters which can be experimentally determined. Chapter IV

provides experimental details and verification of the theoretical framework put forward in Chapter III. Our experimental results confirm an enhancement by three orders of magnitude. In Chapter V, the summary of experimental findings and the future scope of this work are presented.

1.3. Absorption sensing using an adiabatically tapered fiber

Often an adiabatically tapered fiber is used to excite WGMs of a microresonator. As explained earlier, the throughput spectrum of an adiabatically tapered fiber coupled to a WGM microresonator consists of symmetric Lorentzian dips, one per WGM as shown in Fig. 1.3. The quality factor of a WGM is defined as

$$Q = \frac{\upsilon}{\Delta\upsilon} = \omega\tau = \frac{2\pi nL}{\lambda(\alpha L + T)}, \tag{1.1}$$

where $\upsilon = \frac{\omega}{2\pi}$ is the frequency of light, $\Delta\upsilon$ is the full width at half maximum (FWHM), τ is the lifetime of a photon in a mode, λ is the wavelength of light, n is the refractive index of the host medium of the resonator, T is the outcoupling intensity loss per round trip, and αL represents the effective intrinsic intensity loss per round trip where α is the effective loss coefficient and L is the microresonator circumference. It is worth noting that a high quality factor mode will have a narrow linewidth whereas a low quality factor mode will have a broad linewidth. The two factors that contribute to the linewidth are coupling loss and intrinsic loss. Thus the linewidth $(\Delta\upsilon)$ can be written as

$$\Delta\upsilon = (\Delta\upsilon)_c + (\Delta\upsilon)_i, \tag{1.2}$$

where $(\Delta\upsilon)_c$ represents the contribution corresponding to the coupling round-trip loss (T) and $(\Delta\upsilon)_i$ represents the contribution due to intrinsic round-trip loss (αL) Substituting Eq. (1.2) in Eq. (1.1),

$$\frac{1}{Q}=\frac{1}{Q_c}+\frac{1}{Q_i}, \tag{1.3}$$

where the overall Q is determined by Eq. (1.3) in terms of the extrinsic quality factor Q_c and the intrinsic quality factor Q_i :

$$Q_c=\frac{\upsilon}{(\Delta\upsilon)_c}=\frac{2\pi nL}{\lambda T}, \tag{1.4}$$

and

$$Q_i=\frac{\upsilon}{(\Delta\upsilon)_i}=\frac{2\pi nL}{\lambda(\alpha_i L)}. \tag{1.5}$$

Figure 1.3. Symmetric Lorentzian dip. This WGM has $\Delta\upsilon = 20.7$ MHz, Q = 9.1×10^6, and M = 0.83.

For an adiabatic tapered fiber coupled microresonator, the resonant throughput dip depth can be written as

$$M = \frac{4x}{(1+x)^2}, \tag{1.6}$$

where x represents the ratio of coupling loss T to the effective intrinsic loss αL of the microresonator. The dip depth *M* is measured by taking the ratio of the voltage difference between the bottom of the dip and the off-resonance voltage (40 mV in Fig. 1.3) to the total off-resonance voltage (48 mV). The effective intrinsic loss coefficient can be written as $\alpha L = \alpha_i L + f\alpha_s L + f\alpha_a L$, where $\alpha_i L$ represents the intrinsic loss, f represents the evanescent fraction (interacting fraction), $f\alpha_a L$ represents the absorption of the analyte and $f\alpha_s L$ represents the absorption of the solvent (if a solvent is present). While keeping the transmission loss T constant, the effective intrinsic loss αL can be modified by introducing an analyte into the surroundings of a WGM microresonator. This changes x and hence the resonant throughput dip depth gets modified. In analogy with Beer's law, when the analyte absorption is weak, the fractional change in dip depth $\left(\frac{dM}{M}\right)$ is assumed to be proportional to the change in the analyte absorption coefficient. Using the effective intrinsic loss coefficient and Eq. (1.6), the fractional change in dip depth can be written as

$$\frac{dM}{M} = -\left(\frac{1-x}{1+x}\right)\frac{fLd\alpha_a}{(\alpha_i + f\alpha_s + f\alpha_a)L}. \tag{1.7}$$

Under the conditions for low analyte absorption limit $(\alpha_i \gg f\alpha_s + f\alpha_a)$, the above equation becomes

$$\frac{dM}{M} = -\left(\frac{1-x}{1+x}\right)\frac{fLd\alpha_a}{\alpha_i L} = -\left(\frac{1-x}{1+x}\right)\frac{d\alpha L}{\alpha_i L}. \tag{1.8}$$

Now when the modes are strongly overcoupled or undercoupled $\left(x \gg 1 \text{ or } T \gg \alpha L\right)$ or $\left(x \ll 1 \text{ or } T \ll \alpha L\right)$, the fractional change in dip depth as a function of analyte concentration depends only on the intrinsic loss $\alpha_i L$.

$$\left|\frac{1}{M}\frac{dM}{d\alpha L}\right| = \frac{1}{\alpha_i L}. \tag{1.9}$$

Now let us analyze the change in linewidth as we change the analyte concentration. It is worth remembering that the linewidth $\left(\Delta\upsilon\right)$ of a mode is proportional to the sum of coupling loss $\left(T\right)$ and absorption loss $\left(\alpha L\right)$. Hence the fractional change in linewidth is given by

$$\frac{d\Delta\upsilon}{\Delta\upsilon} = \frac{fd\alpha_a L}{T+\alpha L} = \frac{fd\alpha_a L}{T+\left(\alpha_i + f\alpha_s + f\alpha_a\right)L}. \tag{1.10}$$

Under the conditions for low analyte absorption limit, the above expression becomes

$$\frac{d\Delta\upsilon}{\Delta\upsilon} = \frac{fd\alpha_a L}{T+\alpha_i L} = \frac{d\alpha L}{T+\alpha_i L}. \tag{1.11}$$

When the modes are strongly overcoupled $\left(T \gg \alpha L\right)$, the fractional change in linewidth as we change the analyte concentration depends only on the transmission loss T.

$$\frac{1}{\Delta\upsilon}\frac{d\left(\Delta\upsilon\right)}{d\alpha L} = \frac{1}{T}. \tag{1.12}$$

Thus for overcoupled modes, the fractional change in linewidth as we change the analyte concentration is independent of the intrinsic loss, whereas Eq. (1.9) suggests that the fractional

change in dip depth as we change the analyte concentration depends only on the intrinsic loss. Hence in such cases measuring the fractional change in dip depth provides greater sensitivity.

When the modes are strongly undercoupled $(T \ll \alpha L)$,

$$\frac{1}{\Delta\upsilon}\frac{d(\Delta\upsilon)}{d\alpha L} = \frac{1}{\alpha_i L}. \tag{1.13}$$

Thus for undercoupled modes, the fractional change in dip depth or linewidth as we change the analyte concentration depends only on the intrinsic loss and hence we get the same sensitivity for both methods.

1.4. Hollow bottle resonator and mode profiles

A silica capillary is used for making a hollow bottle resonator, shown in Fig. 1.4. There are three stages in the fabrication process [9]. They are

I. Etching of the silica capillary - The etching process (using an HF-methanol mixture) is done to achieve the desired wall thickness for the silica capillary.

II. Chemical treatment of the etched capillary - The chemical treatment using hot sulfuric acid (H_2SO_4) is done to remove the polymer coating from the silica capillary.

III. Making bulge - A bulge is formed in the capillary by heating and pressurizing the capillary.

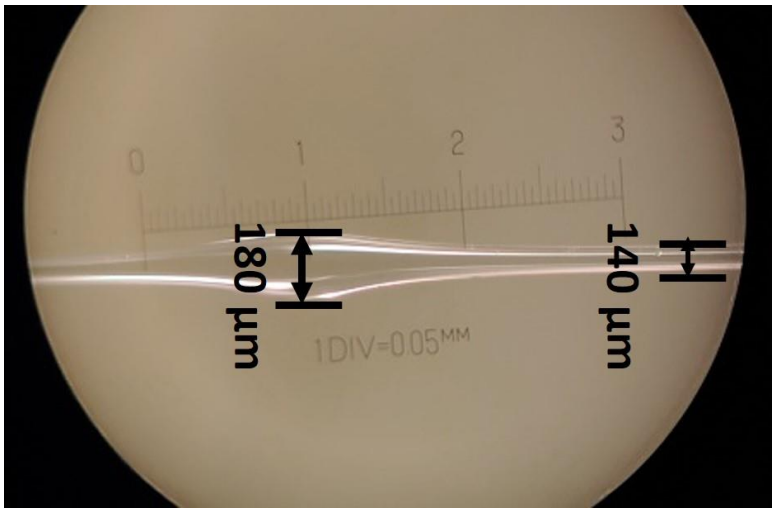

Figure 1.4. Hollow Bottle Resonator. Initial diameter of capillary is 140 µm and the bulge is about 180 µm. The wall thickness is about 15 µm. It is worth noting that the bulge and the end of capillary are not at focus of the microscope simultaneously.

In cylindrical coordinates, the amplitude of a WGM in an HBR is given by,

$$E_{mpq}(r,\phi,z) \approx R_{mp}(r) Z_{mq}(z) \exp(im\phi). \tag{1.14}$$

Let $\beta_0 = \frac{2\pi}{\lambda}$ represent the vacuum propagation constant, n_1, n_2, and n_3 represent the refractive indices in the three radial regions – interior, within the silica wall, and exterior respectively. The radial part in Eq. (1.14) takes different Bessel function forms in the three different regions of an HBR and hence can be written as [40],

$$R_{mp}(r) \propto \begin{Bmatrix} J_m(n_1\beta_0 r) \\ J_m(n_2\beta_0 r) + c_{mp} Y_m(n_2\beta_0 r) \\ H_m^{(1)}(n_3\beta_0 r) \end{Bmatrix}. \tag{1.15}$$

The radial mode intensity profile of a WGM for an HBR (with external and internal wall at 175 and 165 µm respectively) is shown in Fig. 1.5.

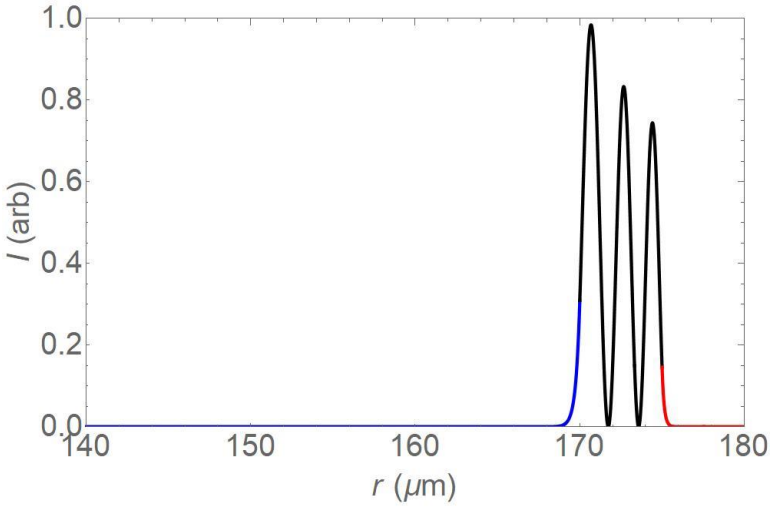

Figure 1.5. TE mode profile of a WGM in an HBR filled with water with an outer boundary at 175 μm and inner boundary at 170 μm; n = 1.444, m = 1000, p = 3, f_{ext} = 0.008, f_{int} = 0.03.

As mentioned earlier, in addition to coupling light into and out of the resonator, the external evanescent fraction enables the interaction of light with the surroundings of the resonator. The sensitivity of WGM sensors depends on the evanescent fraction of the mode. Besides the external evanescent fraction, microresonators such as HBRs provide an internal evanescent fraction. Some WGMs in a thin-walled HBR can have internal evanescent fractions that are significantly larger than their external evanescent fractions, thereby improving the detection threshold. Hence the internal evanescent fraction (also referred to as "interacting fraction") of a WGM is defined, for absorption measurements, to be the ratio of the power circulating in the inner region to the total power circulating in the mode, whereas the external evanescent fraction is the ratio of the power circulating in the outer region to the total power in the mode. The internal evanescent (interacting) fraction (indicated by blue) of the mode is much greater than the external (indicated by red). In addition to having large interacting fractions, the HBR requires a very small amount of analyte, making the HBR an ideal candidate for internal sensing.

CHAPTER II

ADIABATIC AND NON-ADIABATIC TAPERED FIBERS

2. 1. Criteria for adiabatic and non-adiabatic tapers

An optical fiber is a cylindrical dielectric waveguide made by drawing silica. An optical fiber consists of a core which is surrounded by a cladding. Light injected at one end of an optical fiber is transmitted to other end by the process of total internal reflection. For a typical optical single-mode fiber such as SMF-28, the radii of core and cladding at $\lambda = 1550$ nm are 4.1 μm and 62.5 μm respectively, and the corresponding refractive indices of core and cladding are $n_{core} = 1.45205$ and $n_{cladding} = 1.44681$. A mode propagating through an optical fiber is said to be core guided if the effective index $\left(n_{eff}\right)$ of the mode lies between the refractive index of core and cladding. A plot of the normalized propagation constant as a function of normalized frequency is shown in Fig. 2.1.

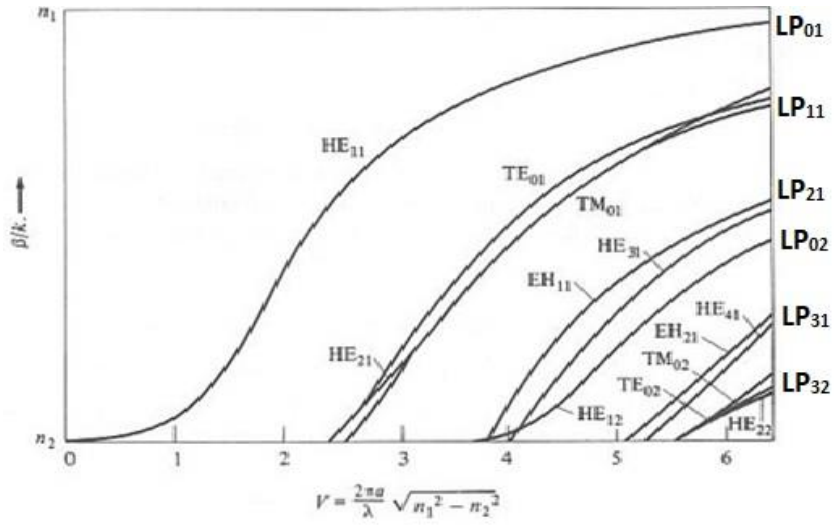

Figure 2.1. Normalized propagation constant as a function of the normalized frequency [41]. Here $\beta/k = n_{\text{eff}}$, $n_1 = n_{\text{core}}$, $n_2 = n_{\text{cladding}}$, and mode families are labelled with the equivalent linearly polarized (LP) designation.

For an optical fiber, the normalized frequency parameter or V number determines the number of modes that may propagate $\left(n_2 < n_{eff} < n_1\right)$ at a given radius and wavelength. The V number for a core guided mode with $n_1 = n_{core}$, $n_2 = n_{cladding}$, $a = 4.1\,\mu\text{m}$, and $\lambda = 1.55\,\mu\text{m}$ was calculated and found to be $V = 2.04$. In Fig. 2.1, at V = 2.04, the fundamental mode HE_{11} is the only mode able to propagate and hence the light remains in the fundamental mode as it propagates through an untapered optical fiber.

A tapered fiber is made by stretching a heated optical fiber, and it consists of a narrow stretched filament called the taper waist, each end of which is linked to the unstretched fiber by a section known as the taper transition. Tapered optical fibers are used in many applications. Tapered optical fibers can efficiently couple light into microresonators. They can also be used as fiber couplers, splitters, absorption sensors and so on. A sketch of a tapered optical fiber is given in Fig. 2.2.

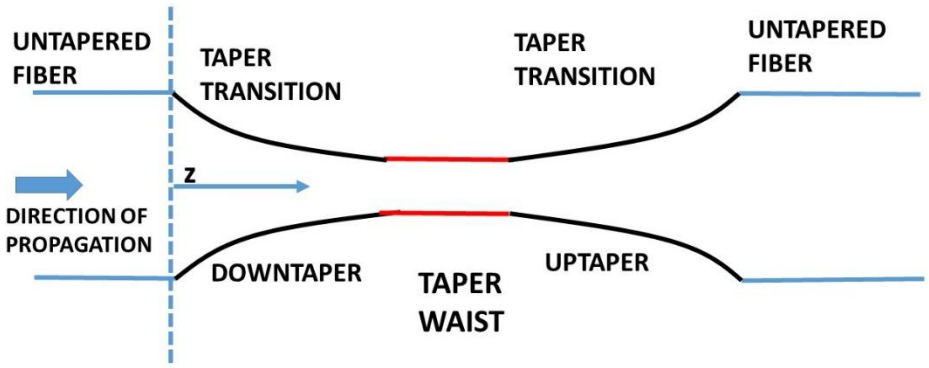

Figure 2.2. Sketch of a tapered optical fiber.

When an optical fiber is tapered down to a small enough diameter, the core can be neglected. Hence at the taper waist, the mode is entirely guided by the cladding-air interface. A mode is said to be cladding guided when the n_{eff} of the mode lies between the refractive indices of cladding and air. At the taper waist, the V number for a cladding guided mode with $n_1 = n_{cladding}$ and $n_2 = n_{air}$, waist radius $a = 1.15$ μm, and $\lambda = 1.55$ μm was calculated and found to be $V = 4.9$. In Fig. 2.1, at $V = 4.9$, in addition to the fundamental mode HE_{11}, other modes such as TE_{01}, TM_{01}, HE_{21}, EH_{11}, HE_{31}, and HE_{12} are able to propagate and thus the taper waist is multimode. Although Fig. 2.1 is for a weakly guiding fiber, in which $n_1 - n_2 \ll n_1$, unlike the taper waist, the allowed modes remain the same. For convenience TE_{01}, TM_{01}, and HE_{21} are considered as one mode – LP_{11}. Hence for the light propagating through a tapered fiber, in the untapered region, the light remains in the fundamental HE_{11} mode of the untapered fiber whereas in the taper waist, multiple fiber modes can be excited. The taper transition region "transforms" the local fundamental mode from

being guided by the core-cladding interface in an untapered fiber to being guided by the cladding-air interface in the taper waist.

A taper transition is said to be adiabatic if light in the single mode of the untapered fiber couples only to the HE_{11} mode at the taper waist. On the contrary, a taper transition is said to be non-adiabatic if light in the single mode of the untapered fiber also couples to higher order fiber modes at the taper waist. Tapered fibers are analogous to the finite square well. Consider a particle in the ground state of the finite square well with dimension *a*. If the dimension of the well is reduced adiabatically, then the particle will remain in the ground state, whereas if the dimension of the well is reduced non-adiabatically, in addition to the ground state, higher energy states are also excited. Consider the propagation of light through the downtaper, waist, and uptaper of an adiabatic tapered fiber. Since the downtaper is adiabatic, on the downtaper taper transition, light in the single mode of the untapered fiber will predominantly couple only to the local HE_{11} mode. At the taper waist, light will remain only in the HE_{11} mode of taper waist. Since the uptaper is also adiabatic, on the uptaper taper transition, light will remain in the local HE_{11} mode and eventually will couple to the single mode of the untapered fiber. Now let us discuss the propagation of light through the downtaper, waist, and uptaper of a non-adiabatic tapered fiber. Since the downtaper is non-adiabatic, light in the single mode of the untapered fiber can couple to the local fundamental (HE_{11}) and higher order modes (mainly LP_{11}) of the taper waist. These two modes don't couple to each other as they travel along the taper waist. Since the uptaper transition is adiabatic, only light in the HE_{11} waist mode can eventually couple to the single mode of the untapered fiber. Previously, it was shown in [42] that by choosing a particular ratio of resonator size to the diameter of the tapered fiber, only the HE_{11} and LP_{11} modes can significantly interact with the WGMs of a microresonator. The following discussion describes the delineation criteria which ensure adiabatic and non-adiabatic taper transitions for different taper profiles.

For a taper transition to be adiabatic, the cladding taper angle Ω_{cl} must be less than some maximum value [12,43] at all values of the inverse taper ratio $\frac{r(z)}{r_0}$ where z is the distance from the untapered fiber to the point of interest, as shown in Fig. 2.2, and $r(z)$ is the local cladding radius, with $r_0 = r(0)$. The local cladding taper angle Ω_{cl} is defined as the angle between the fiber axis and the tangent to the taper profile at the point of interest:

$$\Omega_{cl}(z) \approx \left|\frac{dr(z)}{dz}\right|. \tag{2.1}$$

If the taper transition is adiabatic,

$$\Omega_{cl}(z) \approx \left|\frac{dr(z)}{dz}\right| << (\beta_f - \beta_h)\, r_{cl}, \tag{2.2}$$

where $\beta_f = \beta_f(z)$ and $\beta_h = \beta_h(z)$ are the propagation constants of the fundamental and the higher order mode and $\beta = \frac{2\pi}{\lambda} n_{eff}$. Now we define $\Omega_{\max}$ as the maximum cladding taper angle for the evolution of β from $\beta_{untapered}$ to β_{waist} to be adiabatic:

$$\Omega_{\max} = \frac{r_{cl}}{z_b} = \frac{r_{cl}(\beta_f - \beta_h)}{2\pi}, \tag{2.3}$$

where the beat length z_b is given by:

$$z_b = \frac{2\pi}{\beta_f - \beta_h}. \tag{2.4}$$

$\Omega_{\max}\left(\frac{r(z)}{r_0}\right)$ thus provides a delineation curve with which the cladding taper angle can be compared to determine the adiabaticity.

Now let us take a detour and check how the propagation constants involved in the expression for $\Omega_{\max}$ are calculated. The propagation constant in a step-index dielectric waveguide is obtained by solving the characteristic equation [41] shown below.

$$\left(\frac{J_l'(ha)}{haJ_l(ha)}+\frac{K_l'(qa)}{qaK_l(qa)}\right)\left(\frac{n_1^2J_l'(ha)}{haJ_l(ha)}+\frac{n_2^2K_l'(qa)}{qaK_l(qa)}\right)=l^2\left(\frac{1}{(qa)^2+(ha)^2}\right)^2\left(\frac{\beta}{k_0}\right)^2, \quad (2.5)$$

where J_l and K_l represent the Bessel function of first kind and modified Bessel function with order l, and the prime indicates the derivative with respect to the argument of the Bessel function. In those arguments, *h* and *q* are defined below and *a* is the local core or cladding radius for core or cladding guidance, respectively. From Eq. (2.5), using the Bessel function relations, the solution for HE_{lm} modes can be deduced as follows [44]:

$$\frac{J_{l-1}(ha)}{haJ_l(ha)}=-\left(\frac{n_1^2+n_2^2}{2n_1^2}\right)\frac{K_l'(qa)}{qaK_l(qa)}\left(\frac{1}{(ha)^2}-R\right), \quad (2.6)$$

where

$$R=\left(\left(\frac{n_1^2-n_2^2}{2n_1^2}\right)^2\left(\frac{K_l'(qa)}{qaK_l(qa)}\right)^2+\left(\frac{1}{(qa)^2+(ha)^2}\right)^2\left(\frac{\beta}{k_0}\right)^2\frac{l^2}{n_1^2}\right)^{\frac{1}{2}}.$$

In Eq. (2.6),

$$h^2=n_1^2k_0^2-\beta^2, \quad (2.7)$$

$$q^2 = \beta^2 - n_2^2 k_0^2, \tag{2.8}$$

where $\beta = n_{eff} k_0$ represents the propagation constant and k_0 represents the vacuum wavenumber. For $HE_{l=1,m}$ modes, the solution can be obtained graphically by finding the intersection point of the left and right hand sides of Eq. (2.6), as shown in Fig. 2.3. When the modes are core guided ($n_1 = n_{core}$, $n_2 = n_{cladding}$), $\beta = \beta_f$ is the propagation constant of the core guided HE_{11} mode and $\beta = \beta_h = k_0 n_2$ is the propagation constant of a hypothetical core guided higher-order LP_{11} mode. The intersection point along with Eqs. (2.7) and (2.8) allow us to find the propagation constants for both core and cladding guidance conditions.

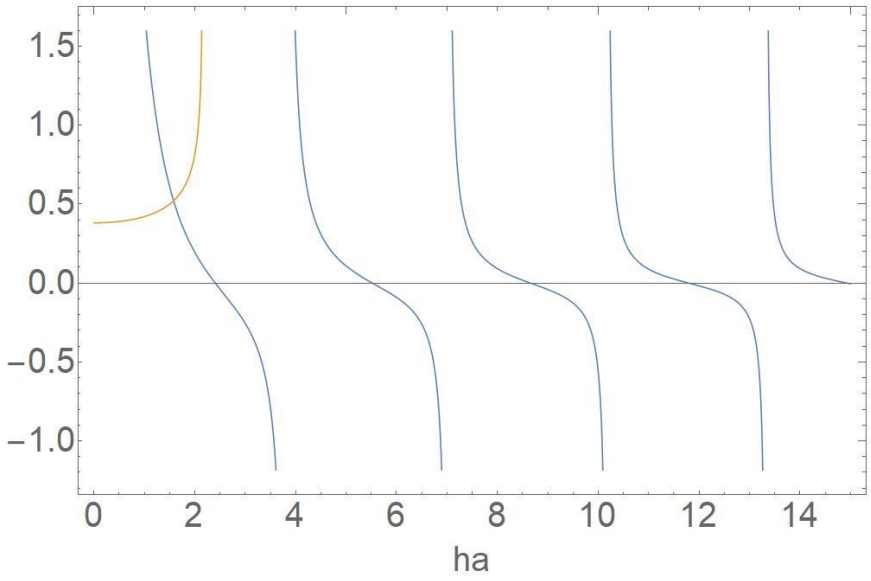

Figure 2.3. Graphical solution for the HE_{l1} mode plotted under core guidance in the untapered fiber. The blue curves represent the LHS and the yellow curve represents the RHS of Eq. (2.6).

When the modes are cladding guided ($n_1 = n_{cladding}$, $n_2 = n_{air}$), $\beta = \beta_f$ is the propagation constant of the cladding guided HE_{11} mode and $\beta = \beta_h$ is the propagation constant of the cladding guided LP_{11} mode. It is worth recollecting that for convenience TE_{01}, TM_{01}, and HE_{21} are considered as one mode – LP_{11}. The characteristic equations [44] for TE and TM modes are

$$\frac{J_1(ha)}{haJ_0(ha)} = \frac{-K_1(qa)}{qaK_0(qa)}, \qquad (\text{TE}) \qquad (2.9)$$

and

$$\frac{J_1(ha)}{haJ_0(ha)} = -\frac{n_2^2}{n_1^2}\frac{K_1(qa)}{qaK_0(qa)}. \qquad (\text{TM}) \qquad (2.10)$$

Once again, the LHS and RHS of Eq. (2.9) and Eq. (2.10) are plotted for increasing values of *ha*. The intersection point along with Eqs. (2.7) and (2.8) allow us to determine the propagation constant of TE_{01} and TM_{01} modes – LP_{11} mode. The calculated propagation constants β_f and β_h assuming core and cladding guidance are shown in Table 1, along with the maximum cladding taper angle from Eq. (2.3).

Table 1. Ω_{max} as a function of inverse taper ratio – delineation curve I.

$\frac{r}{r_0}$	Core guidance			Cladding guidance		
	HE_{11} $\beta_f \times 10^6$ m^{-1}	LP_{11} $\beta_h \times 10^6$ m^{-1}	Ω_{max}	HE_{11} $\beta_f \times 10^6$ m^{-1}	LP_{11} $\beta_h \times 10^6$ m^{-1}	Ω_{max}
1	5.86718	5.85633	0.10792	5.85621	5.85601	0.00199
0.9	5.86566	5.85633	0.08351	5.85618	5.85594	0.00215
0.8	5.86373	5.85633	0.05886	5.85614	5.85583	0.00247
0.7	5.86176	5.85633	0.03778	5.85608	5.85568	0.00278
0.6	5.85970	5.85633	0.02008	5.85598	5.85544	0.00322
0.5	5.85769	5.85633	0.00673	5.85583	5.85506	0.00383
0.4	5.85663	5.85633	0.00116	5.85555	5.85435	0.00478
0.3				5.85496	5.85282	0.00639
0.2				5.85326	5.84847	0.00953
0.1				5.84435	5.82536	0.01889
0.024				5.66167	5.36944	0.06980
0.022				5.65265	5.30497	0.07751
0.0208				5.62262	5.22419	0.08247
0.0192				5.58849	5.12250	0.08904
0.0176				5.54382	5.01057	0.09340
0.0160				5.48497	4.85767	0.09988

Now since we know the propagation constants, using Eq. (2.4) the beat length can be calculated for various taper radii. In order to plot the delineation curve, the larger of the Ω_{max} values for core and cladding guidance at different values of inverse taper ratio was used. These Ω_{max} corresponding to different inverse taper ratios were fitted to a polynomial (red curve) $\left(-0.076x^5 - 0.173x^4 + 0.571x^3 - 0.179x^2 - 0.062x + 0.026\right)$ as shown in Fig. 2.4.

It is worth recalling that for $V = 4.9$ the taper waist is multimode. So far, while calculating Ω_{max} using Eq. (2.3), the difference in propagation constants $\left(\beta_f - \beta_h\right)$ was calculated by finding the propagation constant $\left(\beta_f\right)$ of the local fundamental mode (HE_{11}) and the propagation constant $\left(\beta_h\right)$ of the first family of higher order modes shown in Fig. 2.1 – namely LP_{11}. Now let us relax this and calculate Ω_{max} by considering the propagation constants of the second ($LP_{02} = HE_{12}$, and $LP_{21} = HE_{31}$, EH_{11}) and third family of higher order modes ($LP_{31} = EH_{21}$ and HE_{41}). Since the propagation constants are close, for convenience we will treat the second family of modes as one mode, namely HE_{12}, and the third family of modes as one mode, namely HE_{41}. Thus, depending on the of choice of $\beta_h\left(LP_{11} / HE_{12} / HE_{41}\right)$ in Eq. (2.3), we will have three delineation curves.

As mentioned before, for $HE_{l=1,m}$ modes, the solution can be obtained graphically by finding the intersection point of the left and right hand side of Eq. (2.6). Since we are interested in finding the propagation constant of HE_{12} modes, the left- and right-hand side of Eq. (2.6) are plotted and the second intersection point is considered. The calculated propagation constants β_f and β_h assuming core and cladding guidance are shown in Table 2.

Table 2. Ω_{max} as a function of inverse taper ratio – delineation curve II.

$\frac{r}{r_0}$	Core guidance			Cladding guidance		
	HE_{11} $\beta_f \times 10^6$ m^{-1}	LP_{11} $\beta_h \times 10^6$ m^{-1}	Ω_{max}	HE_{11} $\beta_f \times 10^6$ m^{-1}	HE_{12} $\beta_h \times 10^6$ m^{-1}	Ω_{max}
1	5.86718	5.85633	0.10792	5.85621	5.85615	0.00059
0.9	5.86566	5.85633	0.08351	5.85618	5.8552	0.00877
0.8	5.86373	5.85633	0.05886	5.85614	5.8553	0.00668
0.7	5.86176	5.85633	0.03778	5.85608	5.85498	0.00766
0.6	5.85970	5.85633	0.02008	5.85598	5.8545	0.00883
0.5	5.85769	5.85633	0.00673	5.85583	5.8537	0.01059
0.4	5.85663	5.85633	0.00116	5.85555	5.85223	0.01321
0.3				5.85496	5.84906	0.01761
0.2				5.85326	5.84011	0.02617
0.1				5.84435	5.79285	0.05125
0.024				5.66167	4.86148	0.19112
0.022				5.65265	4.73411	0.20477
0.0208				5.62262	4.58326	0.21515
0.0192				5.58849	4.41877	0.22351
0.0176				5.54382	4.23679	0.22893
0.0160				5.48497	4.09274	0.22169

The delineation curve plotted by using the larger of the Ω_{max} values for core and cladding guidance at different values of inverse taper ratio, fitted to a polynomial $\left(-1.21x^5 + 3.13x^4 - 3.05x^3 + 1.72x^2 - 0.574x + 0.094\right)$ is shown in Fig. 2.4 (green curve)**.**

For the third family of modes (HE_{41}) the solution can be obtained graphically by finding the intersection point of the left and right hand side of Eq. (2.6). The calculated propagation constants β_f and β_h assuming core and cladding guidance are shown in Table 3. The Ω_{max} values corresponding to different inverse taper ratios were fitted to a polynomial $\left(-2.09x^5 + 5.72x^4 - 5.91x^3 + 3.21x^2 - 0.96x + 0.141\right)$ as shown in Fig. 2.4 (yellow curve).

Table 3. Ω_{max} as a function of inverse taper ratio – delineation curve III.

$\frac{r}{r_0}$	Core guidance			Cladding guidance		
	HE_{11} $\beta_f \times 10^6$ m^{-1}	LP_{11} $\beta_h \times 10^6$ m^{-1}	Ω_{max}	HE_{11} $\beta_f \times 10^6$ m^{-1}	HE_{41} $\beta_h \times 10^6$ m^{-1}	Ω_{max}
1	5.86718	5.85633	0.10792	5.85621	5.85545	0.00756
0.9	5.86566	5.85633	0.08351	5.85618	5.85524	0.00841
0.8	5.86373	5.85633	0.05886	5.85614	5.85495	0.00947
0.7	5.86176	5.85633	0.03778	5.85608	5.85454	0.01072
0.6	5.85970	5.85633	0.02008	5.85598	5.85389	0.01248
0.5	5.85769	5.85633	0.00673	5.85583	5.85282	0.01497
0.4	5.85663	5.85633	0.00116	5.85555	5.85087	0.01863
0.3				5.85496	5.84465	0.03078
0.2				5.85326	5.83466	0.03702
0.1				5.84435	5.77144	0.07256
0.024				5.66167	4.44795	0.28990
0.022				5.65265	4.2447	0.31387
0.0208				5.62262	4.0396	0.32769
0.0192				5.58849	-	-
0.0176				5.54382	-	-
0.0160				5.48497	-	-

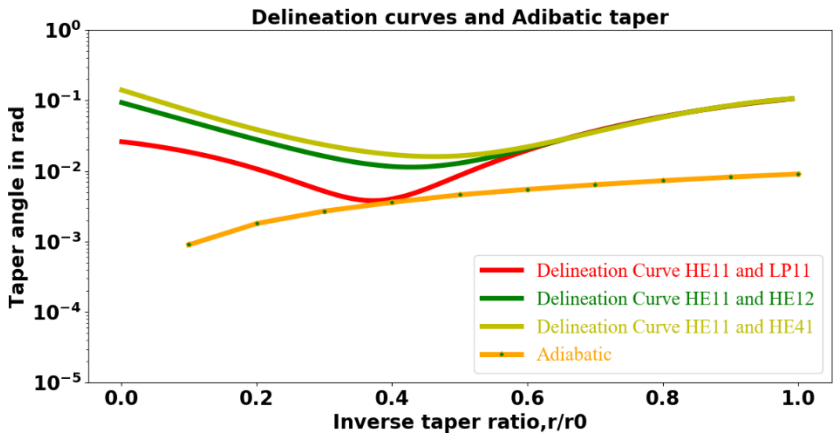

Figure 2.4. Delineation curves and the plot of cladding taper angle Ω_{cl} as a function of inverse taper ratio for an adiabatic taper.

In Fig. 2.4, the red, green, and yellow curves represent different delineation curves. The red curve represents the delineation curve plotted by assuming β_h to be the propagation constant of the LP_{11} mode under the cladding guidance condition. In contrast, the green and yellow curves represent the delineation curves plotted by assuming β_h to be the propagation constant of the HE_{12} and HE_{41} modes under the cladding guidance condition respectively**.** For all values of inverse taper ratio, an adiabatic taper will have a taper angle Ω_{cl} which is less than the delineation curves (red/green/yellow curves) whereas, for a non-adiabatic taper, the plot of the taper angle will pass above the delineation curve for at least some values of the inverse taper ratio. The correct delineation curve is determined by experimental measurement of beat length, as described in the next section. Previously in our lab the taper fiber puller system was designed for an adiabatic taper, and for such a taper the taper angle was calculated and is incorporated (orange curve) in Fig. 2.4.

A detailed discussion about fabrication of tapered fibers and calculation of taper angle Ω_{cl} is provided in the next two sections.

2. 2. Fabrication of adiabatic and non-adiabatic tapers

A sketch of a symmetric adiabatic tapered fiber is depicted in Fig. 2.5. For a symmetric adiabatic tapered fiber, the taper transitions (downtaper and uptaper) are gradual and mirror images of each other about the center of the taper waist and hence the taper transition lengths are equal. Thus in an adiabatic tapered fiber, a single mode of the waist will be excited independent of the direction of propagation of light, provided no other perturbations such as a resonator's WGM coupled to the fiber mode, are present.

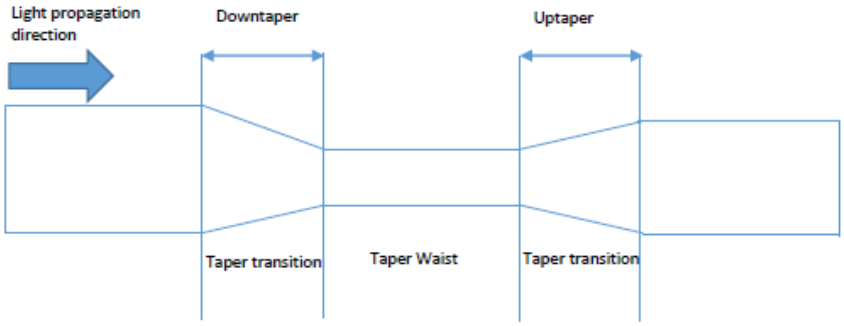

Figure 2.5. Sketch of an adiabatic tapered fiber.

The "flame brush" technique is used to fabricate tapered fibers in our lab. A sketch of the fiber puller device used to fabricate both symmetric adiabatic and asymmetric non-adiabatic tapered fibers in our lab is shown in Fig. 2.6. An optical fiber with its jacket removed is attached to the motorized translation stages A and B. Underneath the stripped area of the fiber a hydrogen torch is installed on another motorized translation stage and the hydrogen flame continuously

brushes the stripped fiber along its length back and forth over a distance known as the brushing length L. Much previous work has been done on fabrication and characterization of symmetric tapered fibers [11-14, 45-51]. In order to produce an asymmetric tapered fiber, stages A and B are pulled with different speeds, whereas an adiabatic tapered fiber is fabricated by pulling stages A and B with the same speed. A sketch of an asymmetric tapered fiber is shown in Fig. 2.7 and a detailed explanation is given in the next section.

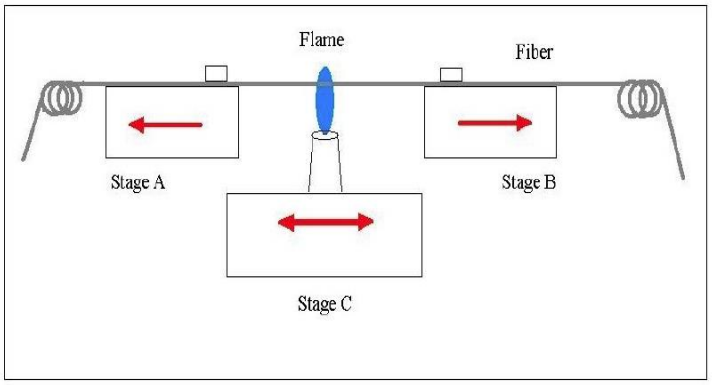

Figure 2.6. Fiber puller apparatus [52].

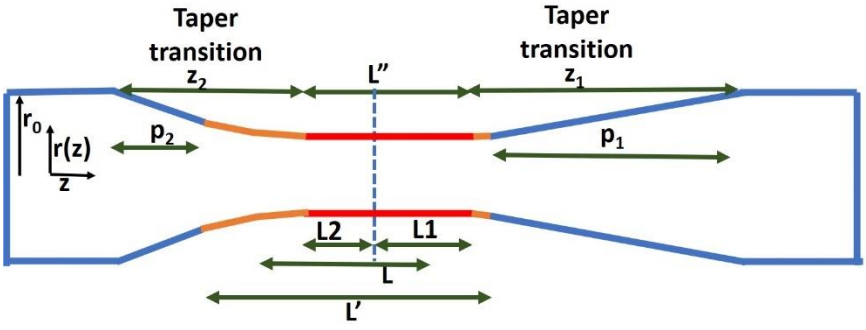

Figure 2.7. An asymmetric taper with a non-adiabatic downtaper and an adiabatic uptaper.

For an asymmetric tapered fiber as shown in Fig. 2.7, the taper transition on one side is abrupt whereas the other is gradual. Thus, the tapered fiber is asymmetric about the center of the

taper waist, and hence the direction of propagation of light through the asymmetric tapered fiber needs to be defined. If the light initially travels through a non-adiabatic downtaper, in addition to the fundamental fiber mode higher order fiber modes will be excited at the taper waist. However, when propagating through the adiabatic uptaper the higher order fiber modes will be lost in the cladding.

A non-adiabatic downtaper permits the light propagating down the waist to be multimode. Thus depending on the radius of the asymmetric tapered fiber, along with the fundamental mode different higher order fiber modes will be excited, which leads to beating of the modes. Since we know the propagation constants of the various order fiber modes at any taper radius, it is possible to calculate the beat length using Eq. (2.4). The calculated beat length for different taper radii is shown in Table 4, along with the measured beat length for three different asymmetric taper profiles.

Table 4. Beat length for various taper waist radii.

Taper waist radius in μm	Calculated beat length in μm $z_b = \frac{2\pi}{\beta_f - \beta_h} = \frac{2\pi}{\Delta\beta}.$			Measured beat length in μm		
	HE_{11} and LP_{11}	HE_{11} and HE_{12}	HE_{11} and HE_{41}	Profile 1	Profile 2	Profile 3
1.5	21.49	7.85	5.17	-	20.08	
1.4	18.06	6.84	4.46	-		
1.3	15.76	6.04	3.97	-	-	
1.2	13.47	5.37	-	12.98	-	12.76
1.1	11.48	4.80	-		-	

For any taper profile, it is possible to measure the beat length by translating the point of fiber – microresonator contact along the waist of the asymmetric tapered fiber. As mentioned earlier, when an asymmetric tapered fiber is used to couple light into a microresonator, the throughput spectral profile is no longer symmetric, and it depends on the relative strength and phase of the fiber modes as they couple into a single resonator mode. Upon translating the point of

contact, the relative phase of the two fiber modes changes and hence the throughput profile changes periodically (from dip to peak or vice versa). The distance which the fiber needs to be translated for the throughput profile to change from a peak or dip to the next peak or dip is defined as one beat length. In our lab, for different asymmetric taper profiles, the average beat length of an asymmetric tapered fiber coupled microresonator system is measured by using a screw-gauge attached 3D stage to which the asymmetric taper is mounted. The experimentally measured beat lengths for three different taper profiles are shown in Table 4 and all are consistent with HE_{11} and LP_{11} being the two fiber modes, and the waist radii are thus determined to be 1.16 μm, 1.47 μm, and 1.16 μm, for Profiles 1, 2, and 3 respectively.

2. 3. Asymmetric tapered fiber – model

A schematic diagram of an asymmetric tapered fiber is shown in Fig. 2.7. The radius of the untapered fiber and brushing length are represented by r_0 and L respectively. The assumptions for the model are as follows:

a) The flame has a definite width and hence the heated region L' extends 0.260 mm beyond the flame brush length L on each end.
b) The end of the uniform waist is not at the limit of the heated region, but inside it by a distance that is inversely proportional to the pulling distance.

The total length of the heated region is given by

$$L' = L + 2(0.260). \tag{2.11}$$

Since the fiber is heated and pulled at the same time, the limit of the waist is recessed from the end of the heated region by a distance estimated to be $rec = 0.131$ mm for the standard symmetric taper. The length of the uniform waist is given by

$$L'' = L' - rec \times \left(\frac{26.88}{p_1} \right) - rec \times \left(\frac{26.88}{p_2} \right), \tag{2.12}$$

where p_1 and p_2 represent the pull distances of the two stages. (The number 26.88 mm is the pull distance for fabricating a symmetric tapered fiber of nominal radius 1 μm). The taper transition lengths on each side are given by

$$z_1 = p_1 + rec \times \left(\frac{26.88}{p_1} \right), \tag{2.13}$$

$$z_2 = p_2 + rec \times \left(\frac{26.88}{p_2} \right). \tag{2.14}$$

For any tapered fiber, in general, its radius in the transition region, $r(z)$, can be written as

$$r(z) = r_0 \, e^{\frac{-z_i}{2L_i}}, \tag{2.15}$$

where z_i is the distance into the transition region from the untapered fiber and L_i is the length of the corresponding part of the taper waist. For the full left side transition length z_2 Eq. (2.15) can be written as

$$r_w = r_0 \, e^{\frac{-z_2}{2L_2}}, \tag{2.16}$$

where r_w is the radius of the taper waist. Similarly for the full right-side transition length z_1,

$$r_w = r_0 \, e^{\frac{-z_1}{2L_1}}. \tag{2.17}$$

We assume that we have a uniform waist of length $L'' = L_1 + L_2$ and hence

$$\frac{z_1}{L_1} = \frac{z_2}{L_2}. \tag{2.18}$$

The taper angle Ω_{cl} is given by the following equation,

$$\Omega_{cl}(z) = \left|\frac{dr(z)}{dz}\right| = \frac{1}{2L_i} r(z_i). \tag{2.19}$$

For the symmetric taper, $p_1 = p_2 = p = 26.88$ mm, $z_1 = z_2 = z = 27.011$ mm, $L_1 = L_2 = \frac{L''}{2}$, and the brushing length is $L = 6.50$ mm, so the heated region length is $L' = 6.50 + 2(0.260) = 7.02$ mm. Since the distance from the heated limit to the end of the uniform waist is 0.131 mm, $L'' = 7.02 - 2(0.131) = 6.758$ mm. Thus Eqs. (2.16) and (2.17) become,

$$r_w = r_0 e^{\frac{-z}{L''}}. \tag{2.20}$$

Since $z = 27.011$ mm and $r_0 = 62.5$ μm, the radius of the waist is given by

$$r_w = r_0 e^{\frac{-z}{L''}} = 1.16 \text{ μm}.$$

For the first asymmetric taper (Profile 1 in Table 5), $p_1 = 27.64$ mm and $p_2 = 3.12$ mm. Using Eq. (2.13) and Eq. (2.14), $z_1 = 27.77$ mm and $z_2 = 4.25$ mm were calculated. Since $L_1 = \frac{z_1}{z_2} L_2 = \frac{z_1}{z_2}(L'' - L_1)$,

$$L_1 = \frac{\left(\frac{z_1}{z_2}\right)}{1 + \frac{z_1}{z_2}} L'' = \frac{6.53}{7.53} L''.$$

Now the brushing length is $L = 4.75$ mm, so $L' = 4.75 + 2(0.260) = 5.27$ mm, and $L'' = 5.27 - 0.131\left(\frac{26.88}{27.64}\right) - 0.131\left(\frac{26.88}{3.12}\right) = 4.01$ mm. Then

$$L_1 = \frac{6.53}{7.53} 4.01 = 3.48 \text{ mm},$$

and

$$r_w = r_0 e^{\frac{-z_1}{2L_1}} = 62.5 e^{\frac{-27.77}{6.96}} = 1.16 \text{ μm}.$$

Before we proceed further, let us try to validate this asymmetric tapered fiber model. To validate the model, we fabricate an asymmetric tapered fiber for a given set of parameters (Profile 1: $p_1 = 27.64$ mm, $p_2 = 3.12$ mm, $L = 4.75$ mm, $L_1 = 3.48$ mm, $L_2 = 0.53$ mm, $z_1 = 21.77$ mm, $z_2 = 4.24$ mm) using an in-house taper puller system. Later the same asymmetric tapered fiber is used to couple light into the microresonator, and the beat length is measured as explained in the previous section. For Profile 1, the beat length was found to be 12.98 μm and is recorded in Table 4. A beat length of 12.98 μm suggests that

a) the modes responsible for beating are HE_{11} and LP_{11} and hence the delineation curve of interest is the red curve shown in Fig 2.8.
b) the radius of the fabricated asymmetric tapered fiber (estimated from Table 4 to be 1.16 μm) is very close to that predicted by the asymmetric tapered fiber model ($r_w = 1.16$ μm).

Using Eq. (2.19) the cladding taper angles for the adiabatic and non-adiabatic taper transitions of an asymmetric taper for Profile 1 are calculated and plotted along with the delineation curves in Fig. 2.8.

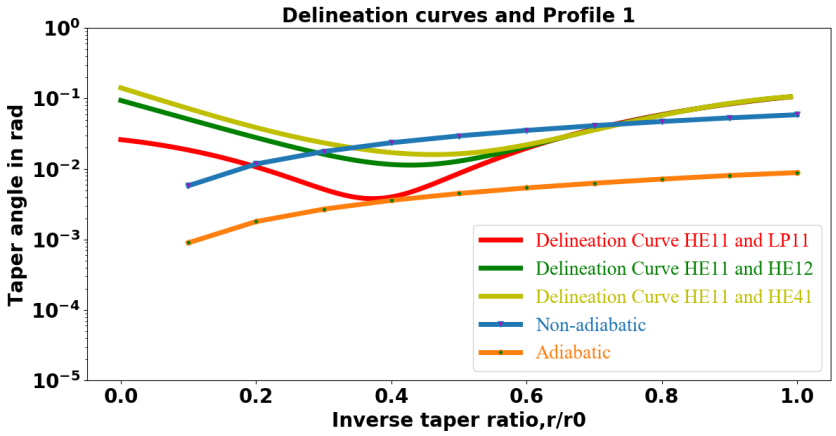

Figure 2.8. Delineation curves and cladding taper angles plotted as a function of inverse taper ratio for an asymmetric tapered fiber with waist radius = 1.16 μm.

The red, green, and yellow curves represent the delineation curves. The inverse taper ratio corresponding to the smallest taper angle in a delineation curve gives a rough estimate of the inverse taper ratio around which transition from core guidance to cladding guidance occurs. For the blue curve in Fig. 2.8, the downtaper angles are above the minimum of the red delineation curve, which indicates that the downtaper will be non-adiabatic. The orange curve representing the uptaper angles passes barely below the red delineation curve indicating that the uptaper is adiabatic. Figure 2.8 thus suggests that the fabricated asymmetric tapered fiber has a non-adiabatic downtaper (abrupt) and an adiabatic uptaper (gradual). This can be compared to Fig. 2.4, which shows the taper angle and delineation curves for an adiabatic tapered fiber with the following set of parameters: $p_1 = p_2 = 26.88$ mm, $L = 6.50$ mm, $L_1 = L_2 = \frac{L}{2} = 3.38$ mm, $z_1 = z_2 = z = 27.01$ mm, and $r_w = 1.15$ μm.

Using Eq. (2.20) the cladding taper angles of asymmetric tapers for two different sets of parameters (Profile 2: $p_1 = 26.35$ mm, $p_2 = 3.35$ mm, $L = 4.78$ mm, $L_1 = 3.53$ mm, $L_2 = 0.59$ mm, $z_1 = 26.48$ mm, $z_2 = 4.40$ mm; Profile 3: $p_1 = 28.20$ mm, $p_2 = 3.45$ mm, $L = 4.74$ mm, $L_1 = 3.55$ mm, $L_2 = 0.56$ mm, $z_1 = 28.32$ mm, $z_2 = 4.47$ mm) are calculated. They are plotted along with the corresponding delineation curve in Fig. 2.9 and Fig. 2.10. A summary of taper parameters for the three different taper profiles is shown in Table 5.

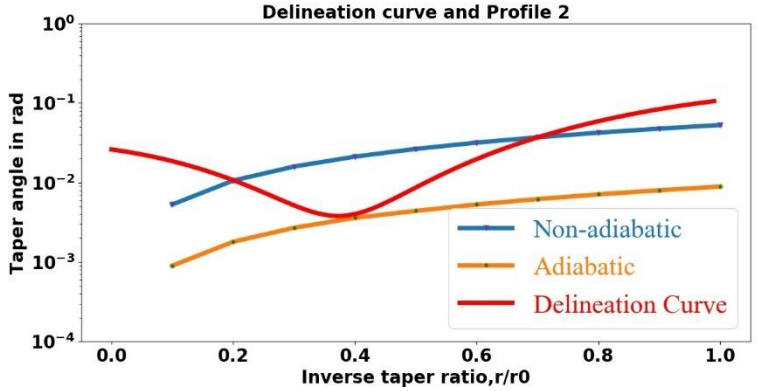

Figure 2.9. Delineation curve and taper angles plotted as a function of inverse taper ratio for an asymmetric tapered fiber with waist radius = 1.47 μm.

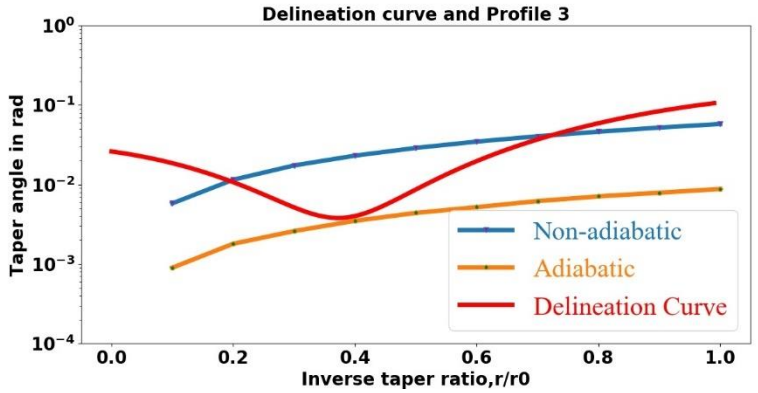

Figure 2.10. Delineation curve and taper angles plotted as a function of inverse taper ratio for an asymmetric tapered fiber with waist radius = 1.16 μm.

Table 5. Summary of taper parameters for various taper profiles.

Taper parameters	Asymmetric tapered fibers			Symmetric tapered fibers		
	Profile 1	Profile 2	Profile 3	Profile 1	Profile 2	Profile 3
Brushing Length L	4.75 mm	4.78 mm	4.74 mm	6.50 mm	6.50 mm	6.50 mm
Waist length L_1	3.48 mm	3.53 mm	3.55 mm	3.38 mm	3.38 mm	3.38 mm
Waist Length L_2	0.53 mm	0.59 mm	0.56 mm	3.38 mm	3.38 mm	3.38 mm
Taper transition length z_1	27.77 mm	26.48 mm	28.32 mm	27.01 mm	25.26 mm	27.01 mm
Taper transition length z_2	4.24 mm	4.40 mm	4.47 mm	27.01 mm	25.26 mm	27.01 mm
Radius of waist r_w	1.16 μm	1.47 μm	1.16 μm	1.15 μm	1.47 μm	1.15 μm

In Fig. 2.8, the red, green, and yellow curves represent the delineation curves. For the blue curve, the downtaper angles are above the minimum of the red, green, and yellow delineation curves, which indicates that in addition to the HE_{11}, LP_{11}, HE_{12} and HE_{41} modes are excited. The blue curve in Fig 2.8 is farther away from the red curve, followed by the green, and yellow curve. This indicates that LP_{11} is strongly excited, followed by HE_{12} and HE_{41}. It is worth noting that the amount of power transferred from HE_{11} mode to $LP_{11}/HE_{12}/HE_{41}$ is not linearly proportional to the distance between the red/green/yellow and blue curves shown in Fig. 2.8. Among all the excited modes, LP_{11} will be the most excited mode, since the fiber sags slightly during the pulling [53] and hence there will be more power in LP_{11} compared to HE_{12} and HE_{41}. This agrees with our beat

length measurements shown in Table 4. Previously it was shown that [42] by choosing a particular ratio of resonator size to the diameter of the tapered fiber, only the HE_{11} and LP_{11} modes can significantly interact with the WGMs of a microresonator and thereby the weak excitation of HE_{12} and HE_{41} can be neglected. Thus, when different asymmetric tapered fibers (Profile 1, Profile 2, Profile 3) are used to couple light into the microresonator, only two modes namely HE_{11} and LP_{11} will interact with the WGMs of a microresonator.

Non-adiabatic tapered optical fibers can be used as sensors themselves. They have been used as refractive index sensors, biosensors, strain and temperature sensors, and magnetic field sensors [54-57].

CHAPTER III

THEORETICAL ASPECTS

3. 1. Simplified model

A model which could precisely describe the behavior of WGMs inside a microresonator would consume vast computational resources and also would be very intricate as it would include a lot of parameters. This complexity would only be compounded in a model that could also precisely treat the interaction between a WGM and multiple coupling-fiber modes. Adding to all this, the ability to give a full description of the effects of an absorbing analyte, inside an HBR, interacting with the WGM, would make the model effectively intractable. However, the behavior of a fiber-coupled microresonator-based dissipative sensor system can be explained adequately using a simplified model [58].

Light from the single mode untapered fiber couples into two modes in the non-adiabatic downtaper. In this model, the two fiber modes are considered as two orthogonal (spatially, not in polarization) guided waves incident on the microresonator, having the same frequency but different propagation constants and thus a variable relative phase β. The reflection and transmission coefficients of fiber-resonator input/output coupling are taken to be real and imaginary, respectively.

The amplitudes of the two incident fiber modes at the point where light gets coupled into the microresonator are given by E_{i1} and $E_{i2}e^{i\beta}$ respectively. The total incident power will be proportional to the sum of the squares of these mode amplitudes. The transmission coefficients of the two fiber modes are it_1 and it_2. The two incident fiber modes couple into a single whispering gallery mode of the resonator as shown in Fig. 3.1, and the WGM couples out into both fiber modes. It is assumed that there is no intermode coupling in the adiabatic uptaper after the microresonator and only the first of the fiber modes, whose amplitudes are E_{r1} and E_{r2} after light couples out of the WGM, is captured as measurable throughput as shown in Fig. 3.1.

The fact that energy needs to be conserved in such a process will induce some constraints on the coupling coefficients. Coupling is assumed to be lossless and hence the coefficients have the following relationships.

$$T_1 = t_1^2 = 1 - r_1^2, \tag{3.1}$$

$$T_2 = t_2^2 = 1 - r_2^2, \tag{3.2}$$

where r_1 and r_2 represent reflection coefficients for the two fiber modes. Energy conservation then says that

$$1 - r^2 = t_1^2 + t_2^2 = T_1 + T_2, \tag{3.3}$$

where r is the internal reflection coefficient for the cavity mode and T_n is the transmissivity for mode *n*. The transmissivities are assumed to be small, i.e., $T_n << 1$.

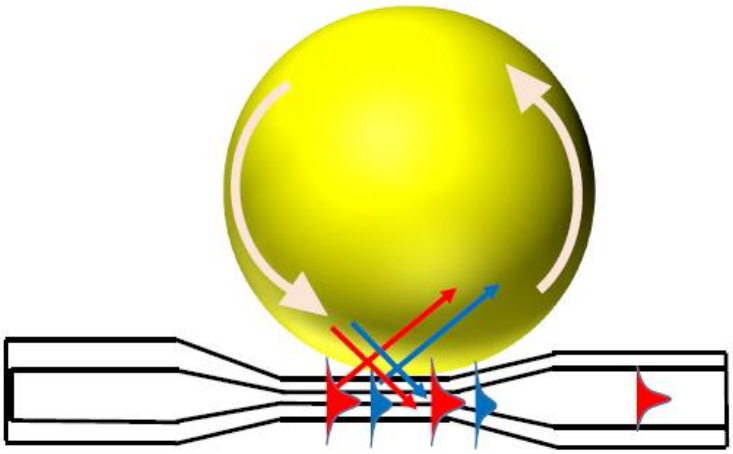

Figure 3.1. Non-adiabatic tapered fiber and a microsphere in contact. The two fiber modes, fundamental (red) and higher order (blue) get coupled into a single whispering gallery mode. The WGM couples out into both fiber modes. The higher order mode gets lost and only the fundamental mode is captured in the detector.

We take E_{i1} and $E_{i2}e^{i\beta}$ to be the amplitudes of the two incident modes, with β their relative phase. The relative phase β will depend on the position of the microresonator along the taper waist of the fiber. The intracavity WGM amplitude E, just after the input coupling point is given by

$$E = \sum_{n=0}^{\infty}\left(it_1E_{i1} + it_2E_{i2}e^{i\beta}\right)\left(re^{-\frac{\alpha L}{2}}e^{i\delta}\right)^n, \tag{3.4}$$

where n represents the number of round trips, L represents the cavity round-trip length, αL is the intrinsic round-trip power loss, and $\delta = kL$ is the round-trip phase accumulation. The throughput mode amplitudes can be then written as

$$E_{r1} = r_1 E_{i1} + it_1 E e^{-\frac{\alpha L}{2}} e^{i\delta}, \tag{3.5}$$

$$E_{r2} = r_2 E_{i2} + it_2 E e^{-\frac{\alpha L}{2}} e^{i\delta}. \tag{3.6}$$

Since we assume that no intermode coupling occurs in the second transition region, and that mode 2 is lost while mode 1 gets captured by the fiber core, mode 2 $\left(E_{r2}\right)$ will be completely neglected from this point onwards. We know that

$$\sum_{n=0}^{\infty} \left(re^{-\frac{\alpha L}{2}} e^{i\delta} \right)^n = \frac{1}{1 - re^{-\frac{\alpha L}{2}} e^{i\delta}}. \tag{3.7}$$

Hence the throughput amplitude of mode 1 can be written as

$$E_{r1} = r_1 E_{i1} - \frac{\left(t_1^2 E_{i1} + t_1 t_2 E_{i2} e^{i\beta}\right) e^{-\frac{\alpha L}{2}} e^{i\delta}}{1 - re^{-\frac{\alpha L}{2}} e^{i\delta}}. \tag{3.8}$$

$$E_{r1} = \frac{\left(r_1 - rr_1 e^{-\frac{\alpha L}{2}} e^{i\delta} - T_1\right) E_{i1} - \sqrt{T_1 T_2} E_{i2} e^{i\beta} e^{-\frac{\alpha L}{2}} e^{i\delta}}{1 - re^{-\frac{\alpha L}{2}} e^{i\delta}}. \tag{3.9}$$

We evaluate to lowest order in the small quantities $T_n << 1$, $\alpha L << 1$, $\delta << 1$. So we can write

$$1 - re^{-\frac{\alpha L}{2}} e^{i\delta} = \frac{T_1 + T_2 + \alpha L}{2} - i\delta, \tag{3.10}$$

$$r_1 - rr_1 e^{-\frac{\alpha L}{2}} e^{i\delta} - T_1 = \frac{T_2 - T_1 + \alpha L}{2} - i\delta. \qquad (3.11)$$

Thus the throughput amplitude of mode 1 becomes

$$E_{r1} = \frac{\left(\frac{T_2 - T_1 + \alpha L}{2} - i\delta\right)E_{i1} - \sqrt{T_1 T_2}E_{i2}e^{i\beta}}{\frac{T_1 + T_2 + \alpha L}{2} - i\delta}. \qquad (3.12)$$

The relative throughput power in mode 1, or overall reflectivity R, is defined as $\left|\frac{E_{r1}}{E_{i1}}\right|^2$, so with $m = \frac{E_{i2}}{E_{i1}}$:

$$R_{\delta\beta} = \left|\frac{\left(\frac{T_2 - T_1 + \alpha L}{2} - i\delta\right) - \sqrt{T_1 T_2}me^{i\beta}}{\frac{T_1 + T_2 + \alpha L}{2} - i\delta}\right|^2. \qquad (3.13)$$

Note that, far off resonance $(T_n, \alpha L \ll \delta \ll 1)$, $R = 1$. The corresponding resonant $(\delta = 0)$ dip depth is $M = 1 - R$. Thus for $\beta = 0$, in the usual case where m is not too large, we have a Lorentzian dip in the signal on cavity resonance; β can be varied by translating the microresonator along the taper waist. When we have two modes incident, the dip for $\beta = 0$ can become a peak $(R > 1)$ for $\beta = \pi$ and other values of β can make the feature asymmetric. The resonant throughput power $(\delta = 0)$ can be expressed as

$$R_{0\beta} = \frac{(T_1 - T_2 - \alpha L)^2 + 4T_1 T_2 m^2 + 4(T_1 - T_2 - \alpha L)\sqrt{T_1 T_2}m\cos\beta}{(T_1 + T_2 + \alpha L)^2}. \qquad (3.14)$$

In order to compare this theoretical model with the experiment, we need to know the values of T_1, T_2, αL, and m. So we are left with an interesting question, which is how to determine T_1, T_2, αL, and m from the resonant throughput of an empty HBR (filled with solvent, if necessary, but no analyte) for $\beta = 0$ and/or $\beta = \pi$.

The probabilities of a photon from the cavity to couple to the fundamental fiber mode and the higher order fiber mode are given by T_1 and T_2 respectively and αL represents the loss due to scattering and absorption. The sum of T_1, T_2, and αL represents the total loss for a WGM. The total loss can be determined by measuring the linewidth $\Delta\upsilon$ of the mode. The quality factor Q of this WGM is given by

$$Q = \frac{4\pi^2 na}{\lambda\left(T_1 + T_2 + \alpha L\right)} = \frac{\upsilon}{\Delta\upsilon}, \tag{3.15}$$

where $L = 2\pi a$, a being the radius of the resonator and n being the refractive index of the host medium of the resonator. So the total loss can be written as

$$T_1 + T_2 + \alpha L = \frac{4\pi^2 na\Delta\upsilon}{c}. \tag{3.16}$$

When $\beta = 0$, the throughput is given by

$$R_{\delta\beta} = R_{00} = \left(\frac{T_1 - T_2 - \alpha L + 2\sqrt{T_1 T_2}\,m}{T_1 + T_2 + \alpha L}\right)^2. \tag{3.17}$$

When $\beta = \pi$, the throughput is given by

$$R_{\delta\beta} = R_{0\pi} = \left(\frac{T_1 - T_2 - \alpha L - 2\sqrt{T_1 T_2}\,m}{T_1 + T_2 + \alpha L}\right)^2. \tag{3.18}$$

So,

$$R_{00} - R_{0\pi} = \frac{8\left(T_1 - T_2 - \alpha L\right)\sqrt{T_1 T_2}\, m}{\left(T_1 + T_2 + \alpha L\right)^2}, \tag{3.19}$$

$$R_{00} + R_{0\pi} = \frac{2\left(T_1 - T_2 - \alpha L\right)^2 + 8T_1 T_2 m^2}{\left(T_1 + T_2 + \alpha L\right)^2}. \tag{3.20}$$

Now define

$$p = \frac{1}{2}\left(T_1 + T_2 + \alpha L\right)^2 \left(R_{00} - R_{0\pi}\right) = 4ab, \tag{3.21}$$

$$q = \frac{1}{2}\left(T_1 + T_2 + \alpha L\right)^2 \left(R_{00} + R_{0\pi}\right) = a^2 + 4b^2. \tag{3.22}$$

with $a = T_1 - T_2 - \alpha L$, $b = \sqrt{T_1 T_2}\, m$, $q = a^2 + 4b^2$, $q^2 - p^2 = \left(a^2 - 4b^2\right)^2$. Then $b = \frac{p}{4a}$, so Eq. (3.22) becomes

$$a^4 - qa^2 + \frac{p^2}{4} = 0. \tag{3.23}$$

Solving the above quadratic equation leads to the following result,

$$a^2 = \frac{1}{2}\left[a^2 + 4b^2 \pm \sqrt{\left(a^2 - 4b^2\right)^2}\right] = \frac{1}{2}\left[a^2 + 4b^2 \pm \left|\left(a^2 - 4b^2\right)\right|\right]. \tag{3.24}$$

To interpret this, first assume that $a^2 > 4b^2$, and hence $\left|a^2 - 4b^2\right| = a^2 - 4b^2 = \sqrt{q^2 - p^2}$,

$$\begin{aligned} a^2 &= \frac{1}{2}\left[a^2 + 4b^2 \pm \left(a^2 - 4b^2\right)\right], \\ a^2 &= \frac{1}{2}\left[q \pm \sqrt{q^2 - p^2}\right]. \end{aligned} \tag{3.25}$$

The one with the negative sign can be neglected; it says $\left(T_1 - T_2 - \alpha L\right)^2 = 4T_1T_2m^2$, but T_1, T_2, αL, and m are all independent. So,

$$T_1 - T_2 - \alpha L = \pm\frac{1}{2}\left(T_1 + T_2 + \alpha L\right)\left[\left(R_{00} + R_{0\pi}\right) + \sqrt{4R_{00}R_{0\pi}}\right]^{1/2}, \quad (3.26)$$

with the sign being the same as the sign of p or $R_{00} - R_{0\pi}$.

Now if we assume that $a^2 < 4b^2$, and hence $\left|a^2 - 4b^2\right| = 4b^2 - a^2 = \sqrt{q^2 - p^2}$. Then,

$$T_1 - T_2 - \alpha L = \pm\frac{1}{2}\left(T_1 + T_2 + \alpha L\right)\left[\left(R_{00} + R_{0\pi}\right) - \sqrt{4R_{00}R_{0\pi}}\right]^{1/2}, \quad (3.27)$$

with the sign being the same as the sign of $R_{00} - R_{0\pi}$. Since we have two equations for $T_1 - T_2 - \alpha L$, we take a detour and explain how we decide which equation needs to be used.

From Eq. (3.21) and Eq. (3.22),

$$p + q = \left(T_1 + T_2 + \alpha L\right)^2 R_{00} = \left(a + 2b\right)^2. \quad (3.28)$$

Guided by experimental observations, consider a scenario where we have a dip and peak corresponding to $\beta = 0$ and $\beta = \pi$ respectively, and the dip depth M increases as we increase αL so that $\frac{dM}{d\alpha L}$ is positive. We know that dip depth $M = 1 - R_{00}$ and hence

$$\frac{dM}{d\left(\alpha L\right)} = -\frac{dR_{00}}{d\left(\alpha L\right)}. \quad (3.29)$$

The peak at $\beta = \pi$ ensures that $R_{00} - R_{0\pi}$ is negative and hence $p = \frac{1}{2}\left(T_1 + T_2 + \alpha L\right)^2 \left(R_{00} - R_{0\pi}\right) = 4ab$ is negative. b is positive since T_1, T_2, and m are always positive. So if p needs to be negative, then a has to be negative. Using R_{00} from Eq. (3.28) in Eq. (3.29),

$$\frac{dM}{d\left(\alpha L\right)} = -\left[\frac{2\left(a+2b\right)\frac{da}{d\alpha L}\left(T_1 + T_2 + \alpha L\right) - 2\left(a+2b\right)^2}{\left(T_1 + T_2 + \alpha L\right)^3}\right]. \qquad (3.30)$$

In order to have a positive $\frac{dM}{d\alpha L}$, the term written inside the square bracket in the above equation needs to be negative. If $2\left(a+2b\right)\frac{da}{d\alpha L}\left(T_1 + T_2 + \alpha L\right) < 2\left(a+2b\right)^2$, the term in the square bracket will be negative. $T_1 + T_2 + \alpha L$ and $\left(a+2b\right)^2$ are always positive and $\frac{da}{d\left(\alpha L\right)} = \frac{d\left(T_1 - T_2 - \alpha L\right)}{d\left(\alpha L\right)}$ is always negative under the assumed conditions. This suggests that if $\left(a+2b\right)$ is positive then the term written inside the square bracket will be negative. Now $\left(a+2b\right)$ is positive when $2b > |a|$ or $a^2 < 4b^2$, so Eq. (3.27) with the minus sign is to be used for calculating $T_1 - T_2 - \alpha L$.

Since we now know $T_1 + T_2 + \alpha L$ and $T_1 - T_2 - \alpha L$, we can calculate T_1 and $T_2 + \alpha L$ by taking the sum and difference of $T_1 + T_2 + \alpha L$ and $T_1 - T_2 - \alpha L$. Since $b = \frac{p}{4a}$, or

$$\sqrt{T_1 T_2}\, m = \frac{\left(T_1 + T_2 + \alpha L\right)^2 \left(R_{00} - R_{0\pi}\right)}{8\left(T_1 - T_2 - \alpha L\right)}\ . \qquad (3.31)$$

From the above equation, we can calculate $\sqrt{T_2 m^2}$, since we know T_1. From looking at Eq. (3.14), it can be inferred that for a solvent filled microresonator, $R_{0\beta}$ can be calculated from $T_1 + T_2 + \alpha L$, $T_1 - T_2 - \alpha L$, $\sqrt{T_1 T_2}\, m$, and β. Thus we don't need to find T_2, αL, and m separately.

3. 2. Theoretical analysis of absorption sensing based on fractional change in dip depth

The sensing experiments described in this report are based on the fact that the resonance dip depth changes with the changes in intrinsic round trip loss due to the presence of the analyte. For a microresonator filled with solvent, the effective round trip loss is given by

$$\alpha L = \alpha_i L + f \alpha_s L. \tag{3.32}$$

Upon introducing analyte, the total effective intrinsic round-trip loss gets modified as

$$\alpha' L = \alpha_i L + f \alpha_s L + f \alpha_a L = \alpha L + \Delta\alpha L, \tag{3.33}$$

where α_i is the intrinsic loss coefficient of the microresonator which includes scattering, absorption, and radiation, α_s is the absorption coefficient of the solvent which contains the analyte in a typical sensing experiment, and α_a is the absorption coefficient of the analyte. For dye (SDC2072, H. W. Sands Corp.) sensing, methanol is used as the solvent. Hence for dye sensing α_a corresponds to the absorption coefficient of SDC2072 respectively. f is the evanescent (interacting) fraction of the WGM which interacts with the solvent and analyte.

By analogy with Beer's Law, the effect of analyte absorption on the resonant dip depth M is assumed to be

$$M(\alpha_a) = M(\alpha_a = 0) e^{-\alpha_a L_{eff}}, \tag{3.34}$$

where L_{eff} is the effective absorption path length which can be negative. So

$$\left|\frac{dM(\alpha_a)}{d\alpha_a}\right| = \left|L_{eff}\right| M(\alpha_a), \tag{3.35}$$

and

$$\left|L_{eff}\right| = \frac{1}{M(\alpha_a)}\left|\frac{dM(\alpha_a)}{d\alpha_a}\right|. \tag{3.36}$$

It is evident from Eq. (3.36) that $\left|\frac{dM}{M}\right| \propto d\alpha_a$ and hence there is a linear dependence for small changes in α_a.

The change in total round-trip intrinsic loss due to the change in analyte concentration is given by

$$d(\alpha L) = fLd\alpha_a. \tag{3.37}$$

Hence it follows that

$$\frac{dM}{d(\alpha L)} = \frac{1}{fL}\frac{dM}{d\alpha_a}. \tag{3.38}$$

So we can write

$$\frac{dM}{d\alpha_a} = fL\frac{dM}{d(\alpha L)}. \tag{3.39}$$

For $\beta = 0$ and for $\beta = \pi$, the dip depth M is given by $1 - R_{0\beta}$ of Eq. (3.14):

$$M = \frac{4T_1(T_2 + \alpha L) - 4T_1T_2m^2 - 4(T_1 - T_2 - \alpha L)\sqrt{T_1T_2}m\cos\beta}{(T_1 + T_2 + \alpha L)^2}. \quad (3.40)$$

If the change in dip depth is small, then

$$\frac{1}{M}\frac{dM}{d\alpha L} = \frac{T_1(T_1 - T_2 - \alpha L) + 2T_1T_2m^2 + (3T_1 - T_2 - \alpha L)\sqrt{T_1T_2}m\cos\beta}{(T_1 + T_2 + \alpha L)\{T_1(T_2 + \alpha L) - T_1T_2m^2 - (T_1 - T_2 - \alpha L)\sqrt{T_1T_2}m\cos\beta\}}, \quad (3.41)$$

and

$$\frac{dM}{M} = \left\{\frac{T_1(T_1 - T_2 - \alpha L) + 2T_1T_2m^2 + (3T_1 - T_2 - \alpha L)\sqrt{T_1T_2}m\cos\beta}{(T_1 + T_2 + \alpha L)\{T_1(T_2 + \alpha L) - T_1T_2m^2 - (T_1 - T_2 - \alpha L)\sqrt{T_1T_2}m\cos\beta\}}\right\} d\alpha L. \quad (3.42)$$

Thus, by combining Eqs. (3.39) and (3.41) an analytical expression for the change in dip depth with respect to change in analyte concentration for a WGM excited in a non-adiabatic tapered fiber coupled microresonator was derived. Ideally, in order to quantify the enhancement in sensitivity, we need to know, for the same change in analyte concentration, how the dip depth of the same WGM will change if an adiabatically tapered fiber with the same waist radius (hence same T_1 and T_2) replaces a non-adiabatic tapered fiber.

Consider a scenario where an adiabatic tapered fiber is used to couple light into and out of the resonator. Only the fundamental mode of the fiber waist is excited and gets coupled into the resonator i.e., $m \to 0$, and when the light gets coupled out, it can couple to higher order fiber modes as well as to the fundamental mode. So when $m \to 0$, Eq. (3.41) becomes

$$\left|\frac{dM}{M}\right| = \left|\frac{(T_1 - T_2 - \alpha L)}{(T_1 + T_2 + \alpha L)(T_2 + \alpha L)}\right| d\alpha L. \quad (3.43)$$

In the above equation, $\frac{dM}{M}$ would be the fractional change in dip depth with an adiabatic tapered fiber of the same waist radius being used to couple light into and out of the microresonator. In the limits of strong overcoupling $(T_1 >> T_2 + \alpha L)$, or strong undercoupling $(T_1 << T_2 + \alpha L)$, the above equation becomes

$$\left|\frac{1}{M}\frac{dM}{d\alpha L}\right| = \frac{1}{T_2 + \alpha L}. \tag{3.44}$$

Now from Eqs. (3.44) and (3.36), it follows that

$$L_{eff} = \left|\frac{1}{M}\frac{dM}{d\alpha_a}\right| = \left|\frac{1}{M} fL\frac{dM}{d\alpha L}\right| = \left|\frac{fL}{M}\frac{dM}{d\alpha L}\right|. \tag{3.45}$$

Thus in the two limiting cases of strongly overcoupled and strongly undercoupled

$$L_{eff\ \max(one\ mode)} = \frac{fL}{T_2 + \alpha L}. \tag{3.46}$$

A lower limit for the sensitivity enhancement factor $\eta_{\min}$ is therefore given by,

$$\eta_{\min} = \frac{L_{eff\,(for\ two\ mode)}}{L_{eff\ \max(one\ mode)}} = \left|\frac{\frac{fL}{M}\frac{dM}{d\alpha L}}{\frac{fL}{T_2 + \alpha L}}\right| = \left|\frac{T_2 + \alpha L}{M}\frac{dM}{d\alpha L}\right|, \tag{3.47}$$

$$\eta_{\min} = \left|\frac{(T_2 + \alpha L)\left[T_1(T_1 - T_2 - \alpha L) + 2T_1T_2m^2 + (3T_1 - T_2 - \alpha \mathrm{L})\sqrt{T_1T_2}m\cos\beta\right]}{(T_1 + T_2 + \alpha L)\left\{T_1(T_2 + \alpha L) - T_1T_2m^2 - (T_1 - T_2 - \alpha \mathrm{L})\sqrt{T_1T_2}m\cos\beta\right\}}\right|. \tag{3.48}$$

If the WGM is not strongly under or over-coupled, then the actual sensitivity enhancement factor η is given by the ratio of $\left|\frac{dM}{M}\right|$ for two modes, Eq. (3.41), to $\left|\frac{dM}{M}\right|$ for (non-ideal) one mode, Eq. (3.43).

$$\eta = \left| \frac{\left(T_2 + \alpha L\right)\left[T_1\left(T_1 - T_2 - \alpha L\right) + 2T_1T_2m^2 + \left(3T_1 - T_2 - \alpha \mathrm{L}\right)\sqrt{T_1T_2}m\cos\beta\right]}{\left(T_1 - T_2 - \alpha L\right)\left\{T_1\left(T_2 + \alpha L\right) - T_1T_2m^2 - \left(T_1 - T_2 - \alpha \mathrm{L}\right)\sqrt{T_1T_2}m\cos\beta\right\}} \right|. \quad (3.49)$$

The above analysis for $\eta_{\min}$ and η is expected to be true only when $dM << M$ (linear regime) and $d\alpha L << \alpha L.$ (The actual conditions are different, and will be discussed in the next chapter). If the fractional change in dip depth is large (nonlinear regime), then the following analysis is preferred.

The values of T_1, $T_2 + \alpha L$, and $T_1T_2m^2$ are calculated using the R_{00}, $R_{0\pi}$, and $\Delta\upsilon$ measurements made with just solvent inside the resonator. Thus for a solvent filled microresonator, the dip depth M of the WGM at $\beta = 0$ is calculated using Eq. (3.40). Upon adding analyte of known concentration, the total effective round-trip loss increases and hence αL gets modified to $\alpha' L.$ The corresponding dip depth is given by:

$$M\left(\alpha' L\right) = \frac{4T_1\left(T_2 + \alpha' L\right) - 4T_1T_2m^2 - 4\left(T_1 - T_2 - \alpha' L\right)\sqrt{T_1T_2}m}{\left(T_1 + T_2 + \alpha' L\right)^2}. \quad (3.50)$$

It is worth recalling that

$$\alpha' L = \alpha_i L + f\alpha_s L + f\alpha_a L = \alpha L + \Delta\alpha L.$$

where $\Delta\alpha L = f\alpha_a L.$ Hence Eq. (3.50) can be written as

$$M(\alpha' L) = \frac{4T_1(T_2 + \alpha L + f\alpha_a L) - 4T_1T_2m^2 - 4\left(T_1 - (T_2 + \alpha L + f\alpha_a L)\right)\sqrt{T_1T_2}m}{(T_1 + T_2 + \alpha L + f\alpha_a L)^2}. \quad (3.51)$$

From Eq. (3.51), it is evident that one can determine the evanescent (interacting) fraction f of the WGM, provided the absorption coefficient α_a of the analyte, the circumference of the resonator L, and $M(\alpha' L)$ are known.

Consequently knowing f and α_a permits one to calculate the theoretical dip depth of the mode with a change in concentration of the analyte using Eq. (3.51). Hence for the cases with significant change in dip depth,

$$\frac{\Delta M}{M} = \frac{M(\alpha' L) - M(\alpha L)}{M(\alpha L)}. \quad (3.52)$$

The sensitivity enhancement factor at $\alpha' L$ is given by the ratio of Eq. (3.52) to Eq. (3.43) assuming the one-mode response is linear.

$$\eta = \frac{\frac{\Delta M}{M}}{\frac{dM}{M}} = \frac{\frac{M(\alpha' L) - M(\alpha L)}{M(\alpha L)}}{\left|\frac{T_1 - T_2 - \alpha L}{(T_1 + T_2 + \alpha L)(T_2 + \alpha L)}\right| d\alpha L}. \quad (3.53)$$

If the one-mode response is nonlinear, $\eta(\alpha' L)$ is given by the ratio of Eq. (3.52) to the $m \to 0$ limit of Eq. (3.52).

$$\eta(\alpha' L) = \frac{\frac{M(\alpha' L) - M(\alpha L)}{M(\alpha L)}}{\frac{M_{m=0}(\alpha' L) - M_{m=0}(\alpha L)}{M_{m=0}(\alpha L)}}. \quad (3.54)$$

The actual sensitivity enhancement factor η shown in Eq. (3.49), can be expressed in terms of two parameters, namely R_{00} and $R_{0\pi}$. To see this, let us revisit the expressions for $T_1 - T_2 - \alpha L$ and $\sqrt{T_1 T_2}\, m$, Eqs. (3.27), (3.31), and express them in terms of $T_1 + T_2 + \alpha L$:

$$T_1 - T_2 - \alpha L = -\frac{1}{2}\left(T_1 + T_2 + \alpha L\right)\left[R_{00} + R_{0\pi} - 2\sqrt{R_{00}}\sqrt{R_{0\pi}}\right]^{\frac{1}{2}}.$$

In the above expression, the term inside the square root can be written as

$$\left[R_{00} + R_{0\pi} - 2\sqrt{R_{00}}\sqrt{R_{0\pi}}\right]^{\frac{1}{2}} = \left[\left(\sqrt{R_{0\pi}} - \sqrt{R_{0\pi}}\right)^2\right]^{\frac{1}{2}} = \sqrt{R_{0\pi}} - \sqrt{R_{00}} = R_1.$$

So the above expression for $T_1 - T_2 - \alpha L$ can be written as

$$T_1 - T_2 - \alpha L = -\frac{1}{2}\left(T_1 + T_2 + \alpha L\right)R_1. \tag{3.55}$$

We know that $T_1 + T_2 + \alpha L + T_1 - T_2 - \alpha L = 2T_1$ and $T_1 + T_2 + \alpha L - \left(T_1 - T_2 - \alpha L\right) = 2\left(T_2 + \alpha L\right)$. It follows that

$$T_1 = \frac{\left(T_1 + T_2 + \alpha L\right)}{2}\left[1 - \frac{1}{2}R_1\right], \tag{3.56}$$

and

$$T_2 + \alpha L = \frac{\left(T_1 + T_2 + \alpha L\right)}{2}\left[1 + \frac{1}{2}R_1\right]. \tag{3.57}$$

Previously it was shown in Eq. (3.31)

$$\sqrt{T_1 T_2}\, m = \frac{\left(T_1 + T_2 + \alpha L\right)^2\left(R_{00} - R_{0\pi}\right)}{8\left(T_1 - T_2 - \alpha L\right)},$$

So

$$\sqrt{T_1T_2}\,m=\frac{\left(T_1+T_2+\alpha L\right)^2\left(R_{00}-R_{0\pi}\right)}{8\left(-\frac{1}{2}\right)\left(T_1+T_2+\alpha L\right)R_1}=\frac{\left(T_1+T_2+\alpha L\right)\left(R_{00}-R_{0\pi}\right)}{-4R_1},$$

$$\sqrt{T_1T_2}\,m=\frac{\left(T_1+T_2+\alpha L\right)\left(\sqrt{R_{0\pi}}+\sqrt{R_{00}}\right)\left(\sqrt{R_{0\pi}}-\sqrt{R_{00}}\right)}{4\left(\sqrt{R_{0\pi}}-\sqrt{R_{00}}\right)}=\frac{\left(T_1+T_2+\alpha L\right)R_2}{4}. \quad (3.58)$$

where $R_2=\sqrt{R_{0\pi}}+\sqrt{R_{00}}$.

Now let us substitute T_1, $T_2+\alpha L$, and $\sqrt{T_1T_2}\,m$ in the $\beta=0$ expression for η $\left(\text{Eq. }(3.49)\right)$ and in the $\beta=0$ expression for $\frac{1}{M}\frac{dM}{d\alpha L}$ $\left(\text{Eq. }(3.41)\right)$.

$$\eta=\left|\frac{\frac{1}{2}+\frac{1}{4}R_1}{\frac{-R_1}{2}}\times\frac{\frac{-R_1}{4}+\frac{R_1^2}{8}+\frac{R_2^2}{8}+\frac{R_2-R_1R_2}{4}}{\frac{1}{4}-\frac{R_1^2}{16}-\frac{R_2^2}{16}+\frac{R_1R_2}{8}}\right|,$$

and

$$\frac{1}{M}\frac{dM}{d\alpha L}=\frac{1}{T_1+T_2+\alpha L}\left[\frac{\frac{-R_1}{4}+\frac{R_1^2}{8}+\frac{R_2^2}{8}+\frac{R_2-R_1R_2}{4}}{\frac{1}{4}-\frac{R_1^2}{16}-\frac{R_2^2}{16}+\frac{R_1R_2}{8}}\right].$$

Upon simplifying the expressions for η and $\frac{1}{M}\frac{dM}{d\alpha L}$ using the following relationships, $R_1^2+R_2^2-2R_1R_2=\left(R_1-R_2\right)^2=4R_{00}$, $R_2-R_1=2\sqrt{R_{00}}$, and $1-R_{00}=\left(1+\sqrt{R_{00}}\right)\left(1-\sqrt{R_{00}}\right)$ we get

$$\eta = \left| \frac{1 - \frac{1}{2}\left(\sqrt{R_{00}} - \sqrt{R_{0\pi}}\right)}{\sqrt{R_{00}} - \sqrt{R_{0\pi}}} \right| \frac{2\sqrt{R_{00}}}{1 - \sqrt{R_{00}}}, \tag{3.59}$$

and

$$\frac{1}{M}\frac{dM}{d\alpha L} = \frac{1}{T_1 + T_2 + \alpha L}\left[\frac{2\sqrt{R_{00}}}{1 - \sqrt{R_{00}}}\right]. \tag{3.60}$$

From Eq. (3.59) it is evident that the expression η consists of two factors; the first factor being $\left| \frac{1 - \frac{1}{2}\left(\sqrt{R_{00}} - \sqrt{R_{0\pi}}\right)}{\sqrt{R_{00}} - \sqrt{R_{0\pi}}} \right|$ and the second factor $\frac{2\sqrt{R_{00}}}{1 - \sqrt{R_{00}}}$. Now let us take a close look at these factors.

Using the approximations $R_{00} \approx 1,\ R_{0\pi} \approx 1,\ \sqrt{R_{00}} - \sqrt{R_{0\pi}} \approx \frac{1}{2}\left(R_{00} - R_{0\pi}\right) << 1,$ the first factor becomes

$$\frac{1 - \frac{1}{2}\left(\sqrt{R_{00}} - \sqrt{R_{0\pi}}\right)}{\sqrt{R_{00}} - \sqrt{R_{0\pi}}} \approx \frac{2}{R_{00} - R_{0\pi}}. \tag{3.61}$$

Similarly, using the same approximations the second factor becomes

$$\frac{2\sqrt{R_{00}}}{1 - \sqrt{R_{00}}} \times \frac{1 + \sqrt{R_{00}}}{1 + \sqrt{R_{00}}} = \frac{2\sqrt{R_{00}} + 2R_{00}}{1 - R_{00}} \approx \frac{4}{M_{00}}. \tag{3.62}$$

Therefore

$$\eta = \left| \frac{1 - \frac{1}{2}\left(\sqrt{R_{00}} - \sqrt{R_{0\pi}}\right)}{\sqrt{R_{00}} - \sqrt{R_{0\pi}}} \right| \frac{2\sqrt{R_{00}}}{1 - \sqrt{R_{00}}} \approx \left| \frac{2}{R_{00} - R_{0\pi}} \right| \frac{4}{M_{00}}. \tag{3.63}$$

Let's revisit the expression for $\frac{1}{M}\frac{dM}{d\alpha L}$ $\left(\text{Eq. } (3.41)\right)$. Then we can write,

$$\frac{\left(T_1 + T_2 + \alpha L\right)}{M}\frac{dM}{d\alpha L} = \frac{T_1\left(T_1 - T_2 - \alpha L\right) + 2T_1T_2m^2 + \left(3T_1 - T_2 - \alpha \mathrm{L}\right)\sqrt{T_1T_2}m\cos\beta}{\left\{T_1\left(T_2 + \alpha L\right) - T_1T_2m^2 - \left(T_1 - T_2 - \alpha \mathrm{L}\right)\sqrt{T_1T_2}m\cos\beta\right\}}.$$

Upon substituting the above expression into Eq. (3.49),

$$\eta = \left| \frac{T_2 + \alpha L}{T_1 - T_2 - \alpha L}\frac{T_1 + T_2 + \alpha L}{d\alpha L}\frac{dM}{M} \right|. \tag{3.64}$$

Now using the expressions $Q = \frac{4\pi^2 na}{\lambda\left(T_1 + T_2 + \alpha L\right)} = \frac{\upsilon}{\Delta\upsilon}$ and $T_1 + T_2 + \alpha L = \frac{4\pi^2 na}{c}\Delta\upsilon,$ we can write

$$\frac{d\Delta\upsilon}{\Delta\upsilon} = \frac{d\alpha L}{T_1 + T_2 + \alpha L}, \tag{3.65}$$

and

$$\frac{1}{\Delta\upsilon}\frac{d\Delta\upsilon}{d\alpha L} = \frac{1}{T_1 + T_2 + \alpha L} = \frac{\lambda Q}{2\pi nL} = AQ. \tag{3.66}$$

Substituting Eq. (3.65) back into Eq. (3.64),

$$\eta = \left| \frac{T_2 + \alpha L}{T_1 - T_2 - \alpha L}\frac{T_1 + T_2 + \alpha L}{d\alpha L}\frac{dM}{M} \right| = \left| \frac{T_2 + \alpha L}{T_1 - T_2 - \alpha L}\frac{\frac{dM}{M}}{\frac{d\left(\Delta\upsilon\right)}{\left(\Delta\upsilon\right)}} \right|. \tag{3.67}$$

Thus

$$\eta = \left| \frac{T_2 + \alpha L}{T_1 - T_2 - \alpha L} \frac{T_1 + T_2 + \alpha L}{d\alpha L} \frac{dM}{M} \right| = \left| \frac{T_2 + \alpha L}{T_1 - T_2 - \alpha L} \frac{\frac{dM}{M}}{\frac{d(\Delta\upsilon)}{(\Delta\upsilon)}} \right| \approx \left| \frac{2}{R_{00} - R_{0\pi}} \right| \frac{4}{M_{00}}. \quad (3.68)$$

Since $\left| \frac{T_2 + \alpha L}{T_1 - T_2 - \alpha L} \right| \approx \left| \frac{2}{R_{00} - R_{0\pi}} \right|$ and $\frac{\frac{dM}{M}}{\frac{d(\Delta\upsilon)}{(\Delta\upsilon)}} \approx \frac{4}{M_{00}}$, Eq. (3.68) provides us a way to compare the dissipative sensing signal based on the fractional dip depth change to the signal based on the linewidth change.

Now let us talk about the absolute sensitivity of an asymmetric tapered fiber coupled microresonator system with two modes incident on the microresonator and an ideal adiabatic tapered fiber ($T_2 \cong 0$, smaller waist radius means different $T_1 = T$) coupled microresonator system with a single mode incident on the microresonator. In general, the absolute sensitivity of a tapered fiber-microresonator system will depend on the evanescent fraction *f* and the quality factor *Q* of the mode. The absolute sensitivity is defined as the fractional change in dip depth as we change the analyte concentration. For an asymmetric tapered fiber coupled microresonator system, with two modes incident on the microresonator, using Eqs. (3.60), (3.62), and (3.66), the absolute sensitivity $\frac{1}{M}\frac{dM}{d\alpha L}$ is given by

$$\left(\frac{1}{M} \frac{dM}{d\alpha L} \right)_{two\ mode} = \frac{1}{T_1 + T_2 + \alpha L} \left[\frac{2\sqrt{R_{00}}}{1 - \sqrt{R_{00}}} \right] \approx AQ \frac{4}{M_{00}}. \quad (3.69)$$

For the ideal adiabatic tapered fiber coupled microresonator system with a single mode incident on the microresonator, the dip depth *M* can be written as

$$M = \frac{4y}{(1+y)^2},$$

where $y = \frac{\alpha L}{T}$. Therefore,

$$\frac{dM}{d\alpha L} = \frac{dM}{dy}\frac{dy}{d\alpha L} = \frac{4}{T}\frac{1-y}{(1+y)^3} = \frac{1}{\alpha L}\frac{4y}{(1+y)^2}\frac{1-y}{1+y} = \frac{M}{\alpha L}\left|\frac{1-x}{1+x}\right|, \qquad (3.70)$$

where $x = \frac{T}{\alpha L}$. Since $Q_i = \frac{2\pi nL}{\lambda \alpha L}$, Eq. (3.70) becomes

$$\left(\frac{1}{M}\frac{dM}{d\alpha L}\right)_{one\ mode} = \frac{1}{\alpha L}\left|\frac{1-x}{1+x}\right| = AQ_i\left|\frac{1-x}{1+x}\right|. \qquad (3.71)$$

Since we know the absolute sensitivity $\left(\frac{1}{M}\frac{dM}{d\alpha L}\right)$ with two modes input and with one mode input, let us find the condition for achieving equal sensitivity for both cases. To have equal sensitivity, both $\frac{1}{M}\frac{dM}{d\alpha L}$, with two mode input and with one mode input, need to be equal. Using Eq. (3.69) and Eq. (3.71), we can infer that for equal sensitivity,

$$Q_i \simeq \frac{4}{M_{00}}\left|\frac{1+x}{1-x}\right| Q \geq \frac{4}{M_{00}} Q. \qquad (3.72)$$

It is worth noting for Eq. (3.71) to hold true, we need same $L = 2\pi a$, same wavelength λ, same refractive index n, and same evanescent fraction (interacting fraction) f, since $d\alpha = f d\alpha_a$. In the ideal case, with one mode incident on the microresonator, to have equal absolute sensitivity as compared to the multimode case the value of Q_i needs to be approximately of the order of 10^9 which is difficult to maintain in fused silica without taking any extraordinary measures.

3. 3. Extended theory

In the model explained above, even though the waist of the asymmetric tapered fiber can support many modes to propagate, it is assumed that there are two input modes of amplitudes $E_{ij}\left(j=1 \text{ or } 2\right)$ which couple into the microresonator mode with amplitude E with coupling coefficients it_j. However with a proper design of an asymmetric tapered fiber with a non-adiabatic downtaper and adiabatic uptaper, it is possible to excite only the fundamental (HE_{11}) and the first family of higher order modes (LP_{11}) [59]. It is also assumed that light in the WGM of the microresonator couples out only to the two modes (HE_{11} and LP_{11}) with the same coupling coefficients it_j. By aptly choosing the ratio of microresonator radius to the fiber waist radius, it is possible to have light from the WGM of a microresonator coupling only to the fundamental and the first higher order mode [42,44]. Furthermore, if there is any coupling into even higher order modes, it can be considered as an extra intrinsic loss. Now the only assumption that remains is that the coupling coefficients for waist mode to resonator mode and resonator mode to waist mode are equal. This assumption is often reasonable, but it's not always true [58,60]. The effect of relaxing this assumption is explained below.

Let us take the input and output coupling coefficients to be different. Let the input coupling coefficients be $it_j\left(j=1 \text{ or } 2\right)$ and the output coupling coefficients be $i\tau_j\left(j=1 \text{ or } 2\right)$, and the r_j represent the external reflection coefficients. For the incident light,

$$T_1 = t_1^2 \; = 1 - r_1^2,$$

$$T_2 = t_2^2 \; = 1 - r_2^2.$$

where T_1 and T_2 represents the input transmissivity of mode 1 and 2, respectively.

Now let us consider the light inside the microresonator. It can undergo either an internal reflection, with an internal reflection coefficient r, or can get coupled out to the output modes of amplitudes E_{rj}, with outcoupling coefficients $i\tau_j$. Then using energy conservation,

$$1-r^2=\tau_1^2+\tau_2^2=T_1'+T_2',$$

where T_n' represents the output transmissivity for mode *n.*

The intracavity WGM amplitude E, just after the input coupling point is given by

$$E = \sum_{n=0}^{\infty}\left(it_1E_{i1} + it_2E_{i2}e^{i\beta}\right)\left(re^{-\frac{\alpha L}{2}}e^{i\delta}\right)^n,$$

where n represents the number of round trips, L represents the cavity round-trip length, αL is the intrinsic round-trip power loss, and $\delta = kL$ is the round-trip phase accumulation. The throughput mode amplitudes can be then written as

$$E_{r1} = r_1E_{i1} + i\tau_1Ee^{-\frac{\alpha L}{2}}e^{i\delta}, \tag{3.73}$$

$$E_{r2} = r_2E_{i2} + i\tau_2Ee^{-\frac{\alpha L}{2}}e^{i\delta}. \tag{3.74}$$

Since mode 2 is lost in the cladding, we neglect E_{r2}.

The throughput amplitude of mode 1 can be written as

$$E_{r1} = r_1E_{i1} + i\tau_1\frac{\left(it_1E_{i1} + it_2E_{i2}e^{i\beta}\right)e^{-\frac{\alpha L}{2}}e^{i\delta}}{1- re^{-\frac{\alpha L}{2}}e^{i\delta}}. \tag{3.75}$$

We evaluate to lowest order in the small quantities $T_n, T_n' << 1$, $\alpha L << 1$, $\delta << 1$. Thus the throughput amplitude of mode 1 becomes

$$E_{r1} = \frac{\left(\frac{T_1' + T_2' + \alpha L}{2} - i\delta - \sqrt{T_1 T_1'} \right) E_{i1} - \sqrt{T_1' T_2} E_{i2} e^{i\beta}}{\frac{T_1' + T_2' + \alpha L}{2} - i\delta}. \quad (3.76)$$

The throughput power, or overall reflectivity R, is defined as $\left| \frac{E_{r1}}{E_{i1}} \right|^2$, where $m = \frac{E_{i2}}{E_{i1}}$:

$$R = \left| \frac{\left(\frac{T_1' + T_2' + \alpha L}{2} - i\delta - \sqrt{T_1 T_1'} \right) - \sqrt{T_1' T_2} m e^{i\beta}}{\frac{T_1' + T_2' + \alpha L}{2} - i\delta} \right|^2. \quad (3.77)$$

The resonant throughput power $(\delta = 0)$ can be expressed as,

$$R_{0\beta} = \frac{\left(T_1' + T_2' + \alpha L - 2\sqrt{T_1 T_1'} \right)^2 - 4 T_1' T_2 m^2 - 4\left(T_1' + T_2' + \alpha L - 2\sqrt{T_1 T_1'} \right) \sqrt{T_1' T_2} m \cos\beta}{\left(T_1' + T_2' + \alpha L \right)^2}. \quad (3.78)$$

The above expression for resonant throughput power is once again in terms of three parameters namely $T_1' + T_2' + \alpha L$, $\sqrt{T_1' T_2} m$, and $2\sqrt{T_1 T_1'}$. It is worth noting that we get Eq. (3.14) upon making the assumptions $T_1' = T_1$ and $T_2' = T_2$.

The probabilities of a photon from the cavity to couple to the fundamental fiber mode and the higher order fiber mode are given by T_1' and T_2' respectively and αL represents the loss due to scattering and absorption. So the total loss can be written as

$$T_1' + T_2' + \alpha L = \frac{4\pi^2 na\Delta\upsilon}{c}. \tag{3.79}$$

Now define

$$p = \frac{1}{2}\left(T_1' + T_2' + \alpha L\right)^2 \left(R_{00} - R_{0\pi}\right) = 4ab, \tag{3.80}$$

$$q = \frac{1}{2}\left(T_1' + T_2' + \alpha L\right)^2 \left(R_{00} + R_{0\pi}\right) = a^2 + 4b^2, \tag{3.81}$$

With $a = -\left(T_1' + T_2' + \alpha L - 2\sqrt{T_1 T_1'}\right)$, $b = \sqrt{T_1' T_2} m$, $q = a^2 + 4b^2$, $q^2 - p^2 = \left(a^2 - 4b^2\right)^2$.

Then $b = \frac{p}{4a}$, so Eq. (3.81) becomes

$$a^4 - qa^2 + \frac{p^2}{4} = 0. \tag{3.82}$$

Solving the above quadratic equation leads to the following result,

$$-\left(T_1' + T_2' + \alpha L - 2\sqrt{T_1 T_1'}\right) = \pm\frac{1}{2}\left(T_1' + T_2' + \alpha L\right)\left[\left(R_{00} + R_{0\pi}\right) - \sqrt{4R_{00}R_{0\pi}}\right]^{1/2}. \tag{3.83}$$

Since $b = \frac{p}{4a}$, or

$$\sqrt{T_1' T_2} m = \frac{\left(T_1' + T_2' + \alpha L\right)^2 \left(R_{00} - R_{0\pi}\right)}{-8\left(T_1' + T_2' + \alpha L - 2\sqrt{T_1 T_1'}\right)}. \tag{3.84}$$

Thus knowing the linewidth $\Delta\upsilon$, R_{00}, and $R_{0\pi}$ allows us to compute $T_1' + T_2' + \alpha L$, $\sqrt{T_1' T_2} m$, and $2\sqrt{T_1 T_1'}$ and hence the resonant throughput power.

For $\beta = 0$ and for $\beta = \pi$, the dip depth M is given by $1 - R_{0\beta}$:

$$M = \frac{\left(T_1' + T_2' + \alpha L\right)^2 - \left(T_1' + T_2' + \alpha L - 2\sqrt{T_1 T_1'}\right)^2 - 4T_1' T_2 m^2 + 4\left(T_1' + T_2' + \alpha L - 2\sqrt{T_1 T_1'}\right)\sqrt{T_1' T_2}\, m \cos\beta}{\left(T_1' + T_2' + \alpha L\right)^2}.$$

(3.85)

Let $a_1 = T_1' + T_2' + \alpha L$, $b_1 = T_1' + T_2' + \alpha L - 2\sqrt{T_1 T_1'}$, $f_1^2 = 4T_1' T_2 m^2$, and $d_1 = 4\left(T_1' + T_2' + \alpha L - 2\sqrt{T_1 T_1'}\right)\sqrt{T_1' T_2}\, m \cos\beta$.

If the change in dip depth is small, then

$$\frac{1}{M}\frac{dM}{d\alpha L} = \frac{2}{a_1}\left[\frac{(b_1 - f_1)(b_1 - f_1 - a_1)}{a_1^2 - (b_1 - f_1)^2}\right]. \tag{3.86}$$

Substituting $m = 0$ in the above expression allows us to determine the fractional change in dip depth for the same additional loss that would be found using a tapered fiber of same waist radius, but with only the fundamental mode incident on the microresonator.

$$\frac{1}{M}\frac{dM}{d\alpha L} = \frac{2}{a_1}\left[\frac{b_1(b_1 - a_1)}{a_1^2 - b_1^2}\right]. \tag{3.87}$$

The sensitivity enhancement factor is found by taking the ratio of absolute value of Eq. (3.85) with arbitrary *m* to Eq. (3.86) with $m = 0$. Thus,

$$\eta = \left|\frac{\dfrac{(b_1 - f_1)(b_1 - f_1 - a_1)}{a_1^2 - (b_1 - f_1)^2}}{\dfrac{b_1(b_1 - a_1)}{a_1^2 - b_1^2}}\right|. \tag{3.88}$$

Now let us express Eq. (3.88) in terms of R_{00} and $R_{0\pi}$. We will find the same result as before, Eq. (3.63). Let us start by writing Eq. (3.83) and (3.84) in terms of R_{00} and $R_{0\pi}$.

$$b_1 = \frac{1}{2}a_1\left[\left(R_{00}+R_{0\pi}\right)-\sqrt{4R_{00}R_{0\pi}}\right]^{\frac{1}{2}} = \frac{1}{2}a_1R_1, \tag{3.89}$$

where $R_1 = \sqrt{R_{0\pi}}-\sqrt{R_{00}}$.

$$f_1 = \frac{a_1\left(R_{00}-R_{0\pi}\right)}{2R_1} = \frac{a_1R_2}{2}, \tag{3.90}$$

where $R_2 = \sqrt{R_{0\pi}}+\sqrt{R_{00}}$. Substituting Eq. (3.90) and (3.89) in Eq. (3.88), we get

$$\eta = \left|\frac{\frac{R_1^2}{4}-\frac{2R_1R_2}{4}+\frac{R_2^2}{4}+\frac{2\left(R_2-R_1\right)}{4}}{\frac{\frac{4-\left(R_1-R_2\right)^2}{4}}{\frac{\frac{R_1^2-2R_1}{4}}{\frac{4-R_1^2}{4}}}}\right|. \tag{3.91}$$

Upon simplifying the Eq. (3.91) using the following relationships, $R_1^2+R_2^2-2R_1R_2 = 4R_{00}$, $R_2-R_1 = 2\sqrt{R_{00}}$, and $1-R_{00} = \left(1+\sqrt{R_{00}}\right)\left(1-\sqrt{R_{00}}\right)$ we get

$$\eta = \left|\frac{1-\frac{1}{2}\left(\sqrt{R_{00}}-\sqrt{R_{0\pi}}\right)}{\sqrt{R_{00}}-\sqrt{R_{0\pi}}}\right|\frac{2\sqrt{R_{00}}}{1-\sqrt{R_{00}}}. \tag{3.92}$$

3. 4. Model predictions – simulated results

For the same arbitrary waist radius, the throughput spectra of non-adiabatic and adiabatic tapered fibers coupled to a microresonator are simulated using Wolfram Mathematica. The input

parameters for the model R_{00}, $R_{0\pi}$, and $\Delta\upsilon$ are obtained by making measurements on the mode of interest. For the asymmetric tapered fiber coupled microresonator system, the model calculates the throughput dip depth using Eq. (3.40) and plots the throughput spectrum. For a given set of parameters $\left(R_{00}=0.8,\ R_{0\pi}=1.20,\ \text{and}\ \Delta\upsilon=33.6\ \text{MHz}\right)$ the values of T_1, $T_2+\alpha L$, and T_2m^2 were calculated using Eq. (3.16), (3.27), and (3.31) and were found to be $T_1=5.01\times10^{-4}$, $T_2+\alpha L=6.13\times10^{-4}$, and $T_2m^2=6.13\times10^{-4}$. Using the values of T_1, $T_2+\alpha L$, and T_2m^2 the theoretical dip depth with methanol inside the resonator was calculated using Eq. (3.40) and was found to be 0.2. The corresponding throughput spectra at $\beta=0$ and π calculated are shown in Fig. 3.2 (a) and Fig. 3.2 (b). According to Eq. (3.50), the dip depth varies with the concentration of analyte solution inside the resonator. For any predetermined analyte concentration, $M\left(\alpha' L\right)$ is experimentally measured. Knowing $M\left(\alpha' L\right)$ and α_a allows us to determine f in such a way that the experimental measurement matches well with the predicted dip depth using Eq. (3.51).

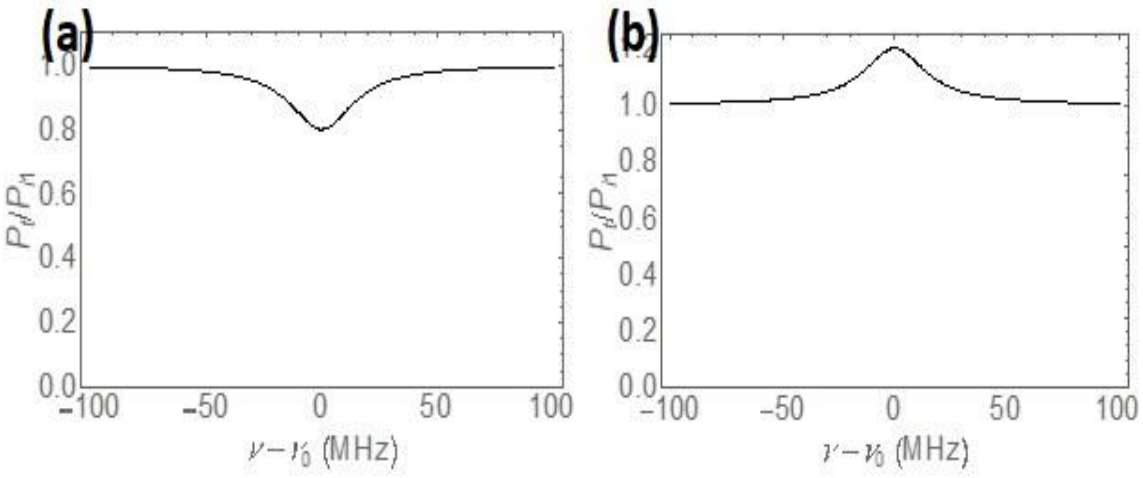

Figure 3.2. Throughput spectrum (a) at β = 0, M = 0.2 and (b) at β = π, M = -0.2. (no analyte.)

Now, with the analyte, the dip depth and throughput spectrum given by the model for a set of parameters $\left(R_{00} = 0.8,\ R_{0\pi} = 1.2,\ \alpha_a = 0.4 \text{ nM} \times 0.4 \frac{\text{m}^{-1}}{\text{nM}},\ f = 0.25 \right)$ are shown in Fig. 3.3.

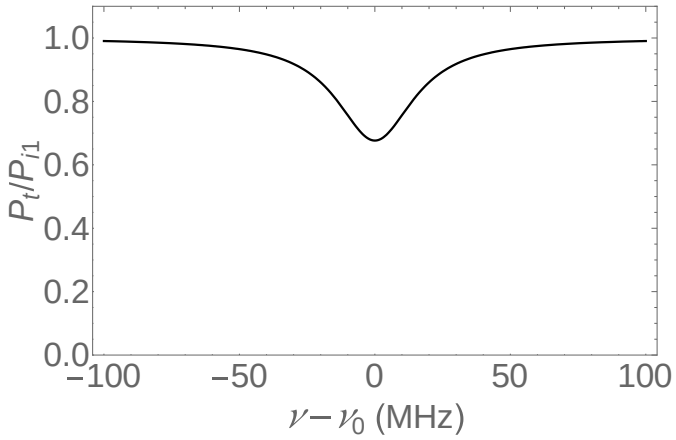

Figure 3.3. Throughput spectrum at $\beta = 0$ for 0.4 nM solution, $M(\alpha' L) = 0.323$.

From Figs. 3.2 (a) & 3.3, it is evident that dip depth changes with increasing analyte concentration for the given set of parameters. Thus

$$\frac{\Delta M}{M} = \frac{M(\alpha' L) - M(\alpha L)}{M(\alpha L)} = \frac{0.323 - 0.200}{0.200} = 0.615 = 61.5\%,$$

and using Eq. (3.42),

$$\frac{dM}{M} = 0.668 = 66.8\%.$$

Repeating a similar procedure for various predetermined analyte concentrations allows us to find the value of f by averaging the values found at different concentrations.

For a symmetric tapered fiber coupled microresonator system, with the same values of T_1, $T_2 + \alpha L$, and $T_2 m^2$, the model calculates the dip depth by substituting m and $\beta = 0$ in Eq. (3.40) and plots the throughput spectrum. The simulated throughput spectrum is shown in Fig. 3.4.

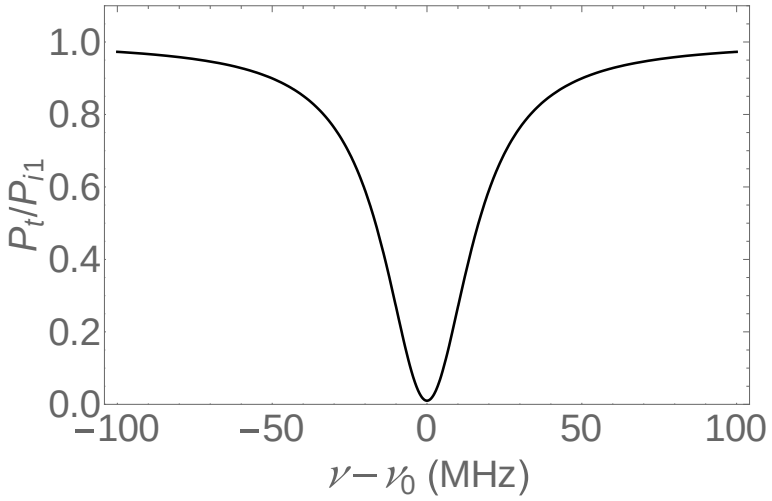

Figure 3.4. Throughput spectrum of an adiabatic tapered fiber coupled methanol filled microresonator system, $M = 0.989$.

For an analyte concentration of 0.4 nM, with $f = 0.25$ the dip depth and throughput spectrum given by the model are shown in Fig. 3.5.

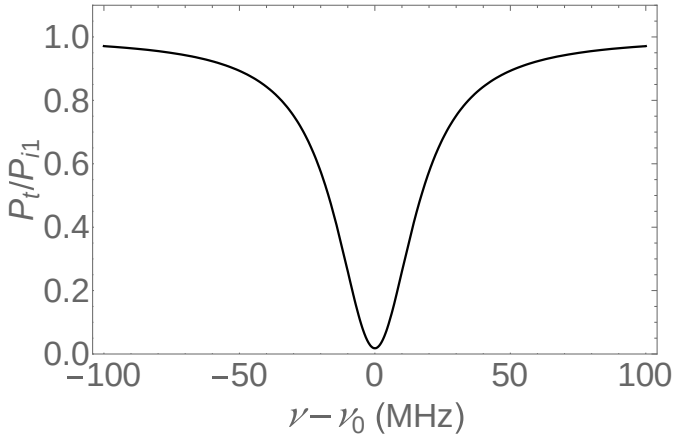

Figure 3.5. Throughput spectrum for 0.4 nM solution, $M(\alpha' L)$ = 0.981.

Thus,

$$\left|\frac{\Delta M}{M}\right| = \frac{M(\alpha L') - M(\alpha L)}{M(\alpha L)} = \left|\frac{0.981 - 0.989}{0.989}\right| = 8.1\times10^{-3},$$

and

$$\left|\frac{dM}{M}\right| = \left|\frac{(T_1 - T_2 - \alpha L)}{(T_1 + T_2 + \alpha L)(T_2 + \alpha L)}\right| d\alpha L = 7.21\times10^{-3}.$$

It is worth noting that with both asymmetric and symmetric tapered fibers being used to couple light into and out of the microresonator, as we get into the nonlinear regime, $\frac{\Delta M}{M}$ is no longer equal to $\frac{dM}{M}$. A detailed analysis of this behavior will be explained in the next chapter.

CHAPTER IV

METHODOLOGY AND RESULTS

4. 1. Introduction

This chapter validates the theoretical framework put forward in Chapter III. Specific details about the experimental setup and dip depth measurement for dye absorption sensing using asymmetric and symmetric tapered fibers are described in section IV. 2. Section IV. 3 provides details about the measurement of the absorption coefficients of methanol and dye. Preliminary results which show the agreement between the theoretical dip depth and measured dip depth are shown in section IV. 4.

In section IV. 5, detailed analysis of the experiment performed using an asymmetric (Profile 1) and symmetric tapered fiber (Profile 1) is presented. Section IV.5 is further divided into six subsections. The first subsection (IV. 5. a) explains how the interacting fraction *f* of the mode of interest is determined. Knowing the interacting fraction *f* of the mode allows us to calculate the theoretical fractional change in dip depth and thereby allows us to compare the experimental fractional change in dip depth to the theoretical prediction.

The second subsection (IV. 5. b) explains how the fractional change in dip depth varies as a function of analyte concentration when an asymmetric tapered fiber of arbitrary waist radius is used to couple light into and out of the microresonator. The theoretical and experimental values of fractional change in dip depth are plotted as a function of analyte concentration and the slopes of the curves are determined.

The third subsection (IV. 5. c) describes the fractional change in dip depth when a symmetric taper of the same arbitrary waist radius is used to couple light into and out of the microresonator. Once again, the theoretical and experimental values of fractional change in dip depth are plotted as a function of analyte concentration and the slopes of the curves are determined. The experimental enhancement factor is determined by taking the ratio of experimental slope with the asymmetric taper to the experimental slope with the symmetric taper.

In general, dissipative sensing can be studied by monitoring the change in linewidth or the change in resonant throughput dip depth. The dip depth based dissipative sensing signal is predicted to be more sensitive than linewidth based dissipative sensing by a factor which is approximately equal to $\frac{4}{M_{00}}$ where M_{00} is the methanol dip depth. In the fourth (IV. 5. d) and fifth (IV. 5. e) subsections the two dissipative sensing signals are compared. Subsection IV. 5. d explains the change in linewidth as we increase the analyte concentration when an asymmetric tapered fiber of arbitrary waist radius is used to couple light into and out of the microresonator. The theoretical and experimental values of fractional change in linewidth are plotted as a function of analyte concentration and the slopes of the curves are determined. From IV. 5. b and IV. 5. d, since we know the slope of fractional change in dip depth versus analyte concentration, and the slope of fractional change in linewidth versus analyte concentration, we can take the ratio of the slopes and then compare it to the predicted value of $\frac{4}{M_{00}}$.

Subsection IV. 5. e describes the fractional change in linewidth when a symmetric taper of the same arbitrary waist radius is used to couple light into and out of the microresonator. The linewidth and its fractional change should be the same for the symmetric taper as for the asymmetric taper. The theoretical and experimental values of fractional change in linewidth is plotted as a function of analyte concentration and the slopes of the curves are determined. Once again, the ratio of the slopes of fractional change in dip depth versus analyte concentration (from section. IV. 5. b), and fractional change in linewidth versus analyte concentration (from section. IV. 5. e) is compared to the predicted value of $\frac{4}{M_{00}}$.

In the last subsection (IV. 5. f) the absolute sensitivity of the asymmetric tapered fiber coupled microresonator system is compared with the absolute sensitivity of an ideal adiabatic tapered fiber coupled microresonator system where a single mode is incident on the microresonator. This shows that equivalent sensitivity can be achieved in the multimode input case with a WGM of much smaller *Q*.

Section 1V. 6 provides a summary of an experiment performed using an asymmetric (Profile 2) and a symmetric tapered fiber (Profile 2). This section is also further divided into six subsections.

Section 1V. 7 provides a summary of an experiment performed using an asymmetric (Profile 3) and a symmetric tapered fiber (Profile 3). Similar to sections IV. 5 and IV. 6, this section is also further divided to six subsections. A summary of all the experimental results are provided in a Table at the end of this chapter.

4. 2. Experimental setup for sensing absorption in dye

An illustration of the experimental setup for dye absorption sensing is shown in Fig. 4.1. A tunable diode laser (New Focus, model number: 6328) spanning a wavelength range from 1508 nm to 1580 nm is used as the light source. A function generator FG (Wavetek, model 395) is used to scan the laser in frequency. Before the light passes through a set of waveplates (WP), the beam passes through an anamorphic prism (AP) and an optical isolator (OI). The waveplates are used to select WGMs of one polarization. A fiber coupler (FC) is used to couple light into the tapered fiber and a fiber isolator is used to prevent any back reflections arising from the tapered fiber. The light then travels through the tapered fiber and couples in and out of the microresonator. The signal is extracted at the other end of the tapered fiber and fed into a Newport detector (model 818-IR). The power meter (Newport, model 2832-C) attached to the detector is coupled to an oscilloscope (Tektronix, model TDS 2022B) that is triggered by the synchronization output of FG. A typical off – resonant throughput power, essentially equal to the input power, was about 500 μW.

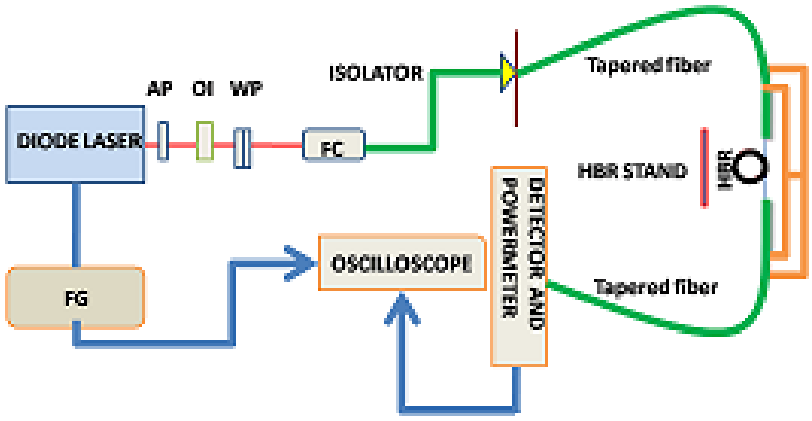

Figure 4.1. Illustration of the experimental setup for dye absorption sensing.

Initially, an asymmetric tapered fiber with a non-adiabatic downtaper and an adiabatic uptaper was used to couple light into and out of the microresonator. After the light from the asymmetric tapered fiber was coupled into a resonator filled with methanol, analyte (dye) at predetermined concentrations was added to the methanol and changes in WGM dip depths were recorded at $\beta = 0$. Then the asymmetric tapered fiber was replaced by a symmetric tapered fiber of the same waist diameter and for the same WGM, changes in dip depth with different analyte concentrations were recorded and processed.

According to our model, a huge enhancement is predicted for a WGM which changes from a small dip to a small peak upon translating the microresonator along the asymmetric tapered fiber. Hence our mode of interest in general has a dip depth less than 15%. To detect any change in dip depth of a WGM whose dip depth is less than 15% a better resolution of the signal is preferred. In our case, a better signal resolution is achieved by using the ac coupling setting on the oscilloscope. The ac coupling setting on the scope enables us to remove the dc component of the signal and helps us in improving the resolution of the signal measurements.

Based on the model, when the asymmetric tapered fiber is replaced by a symmetric tapered fiber of the same waist radius, the throughput spectrum corresponding to the mode of interest becomes very close to that of critical coupling (dip depth corresponding to 100%) and the fractional change in dip depth will be very small. In order to detect any change in the dip depth, we must be looking at the bottom of the dip and hence our oscilloscope needs to be in the most sensitive vertical (voltage) scale, which in our case is 2 mV.

In order to collect better data, the liquid inside the microresonator had to stay stationary and hence horizontal alignment of the microresonator was preferred. Both tapered fibers were mounted 90° to the HBR as shown in Fig. 4.2. A diligent effort was made to avoid tilt of the tapered fibers with respect to the equatorial plane of the HBR. A tightly capped plastic vial was

used as the reservoir for the analyte. The two ends of HBR are connected to the reservoir and the analyte inside the reservoir was pushed through the HBR using a syringe feed at the top of the analyte reservoir.

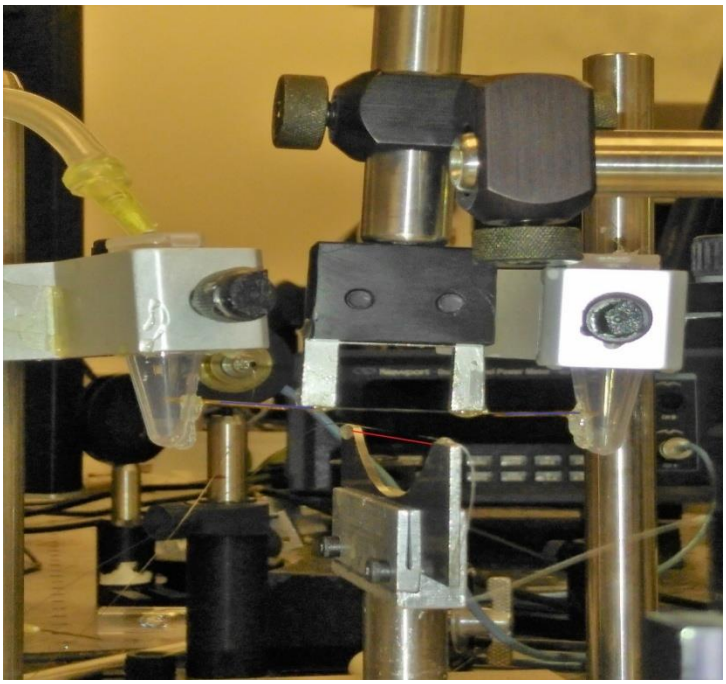

Figure 4.2. Illustrating the horizontal alignment of the resonator. The tapered fiber (marked in red) is mounted 90^{o} relative to the resonator.

4. 3. Measuring absorption coefficient of dye

In this section, detailed information about measuring the absorption coefficient of the dye is presented. The absorption coefficient of SDC 2072 dye in methanol was measured at three different wavelengths – 1550, 1530 nm, 1565 nm.

In order to find the absorption coefficient of dye (α_a) in methanol, one should know the absorption coefficient of methanol (α_s) at 1550 nm. The experimental details for determining α_s at low power is discussed below.

Light from the diode laser is coupled into a fiber-optic patch cord. The other end of the patch cord is connected to a collimator. The schematic diagram for the path of light through a cuvette filled with methanol is shown in Fig. 4.3. The optical power of collimated input light was measured to be $P_1 = 0.9540\,\mu W$ right before the cuvette. A detector is kept right after the cuvette to collect the light coming through the cuvette of 4 mm thickness. The cuvette has a wall thickness of 1 mm on both sides. Hence light travels a distance $L = 2$ mm through methanol in the cuvette. The light encounters four boundaries namely air-glass, glass-methanol, methanol-glass, glass-air before reaching the detector. At each boundary, some light will be reflected and some transmitted. Hence the transmittance at each boundary was calculated and accounted for while calculating the measured absorption coefficient of methanol. Transmittance at the air-glass boundaries is 0.9500, whereas transmittance at the glass-methanol interfaces is 0.9929. An optical output power of $P_d = 0.1471\,\mu W$ was detected.

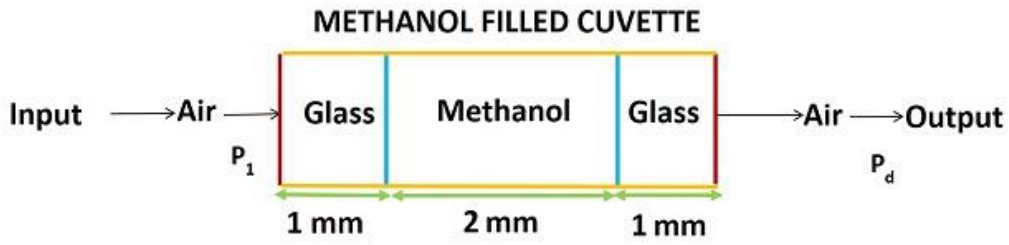

Figure 4.3. Path of light through a cuvette filled with methanol.

Using Beer-Lambert's law, we can write

$$P_4 = P_3 e^{-\alpha_s L} \tag{4.1}$$

where P_3 and P_4 represent the power before and after the methanol within the cuvette. Knowing the values of incident power P_1, transmittance at the two boundaries, and the output power P_d allows us to compute P_3 and P_4. The power after the first and the second boundary is given by $P_2 = 0.9500 P_1$ and $P_3 = 0.9929 P_2$ respectively. Since we know the detected power P_d, the power at the fourth and third boundary is given by $P_5 = \frac{P_d}{0.95}$ and $P_4 = \frac{P_5}{0.9929}$ respectively. Knowing the values of P_4, P_3, and L allows us to compute the absorption coefficient of methanol. Using Eq. (4.1) the absorption coefficient of methanol was found to be $\alpha_s = 8.7636\ \text{cm}^{-1}$ at 1550 nm. In order to determine α_a, dye solutions of predetermined concentrations were added to methanol and the corresponding optical power P_d was detected. Upon adding dye solution Beer-Lambert's law can be written as

$$P_4 = P_3 e^{-(\alpha_s + \alpha_a)L}, \tag{4.2}$$

where P_3 and P_4 represent the power before and after the methanol within the cuvette. Thus

$$\alpha_a = -\left[\alpha_s + \frac{1}{L}\ln\left(\frac{P_4}{P_3}\right)\right]. \tag{4.3}$$

A similar procedure was carried out at the other two wavelengths, where there was no measurable change in α_s, and α_a was plotted as a function of concentration of dye. A plot of α_a versus analyte concentrations at 1550 nm is shown in Fig. 4.4.

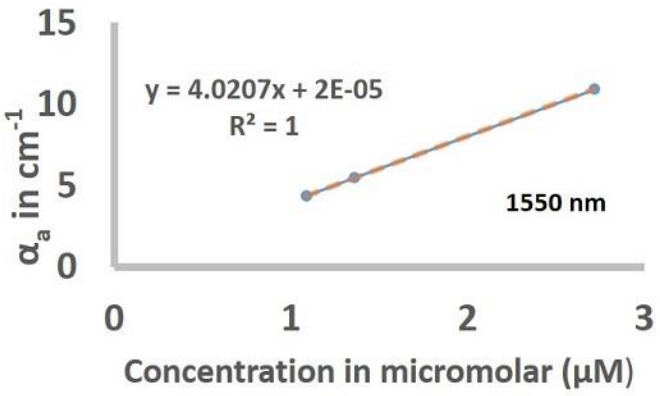

Figure 4.4. Absorption coefficient of dye versus dye concentration at 1550 nm.

It was found that for the given dye, the absorption coefficient increases linearly with concentration of dye. Hence α_a at low concentrations can be found by extrapolating the measurements made at high concentrations. The slope of the curve in Fig. 4.4 is $4.02\,\frac{\text{cm}^{-1}}{\mu\text{M}}$. The slope was found to be $4.00\,\frac{\text{cm}^{-1}}{\mu\text{M}}$ for the other wavelengths (1535 nm and 1565 nm). Therefore at low concentrations the absorption coefficient of dye α_a was found approximately to be $4\times10^{-1}\,\frac{\text{m}^{-1}}{\text{nM}}$. It is worth noting that these measurements were made at low powers and hence we are not saturating the absorption of methanol. In reality, the intensity of light inside the HBR is high and hence the methanol absorption is strongly saturated. Hence the measurement of α_s and α_a was performed at high input power (5.41 mW) and lenses were used to focus light into the cuvette and to the detector. The methanol absorption coefficient was found to be $\alpha_s = 2.2\,\text{m}^{-1}$ which suggests that the methanol absorption is getting saturated. In spite of the solvent saturation, α_a for the dye remains unchanged, showing that the analyte absorption is independent of solvent saturation, and that the analyte absorption saturation is negligible.

4. 4. Preliminary experimental results

A typical experimental setup was shown in Fig. 4.1. A thin-walled HBR with a wall thickness of 5-10 μm and outer radius of 175 μm is made and is glued to an HBR stand. The light from the tunable diode laser is frequency scanned and a mode which changes from dip to peak upon translating the microresonator along the tapered fiber is selected. Preliminary experimental results using an asymmetric tapered fiber (Profile 1) with a non-adiabatic downtaper and an adiabatic uptaper to couple light into and out of the microresonator are shown in Fig. 4.5.

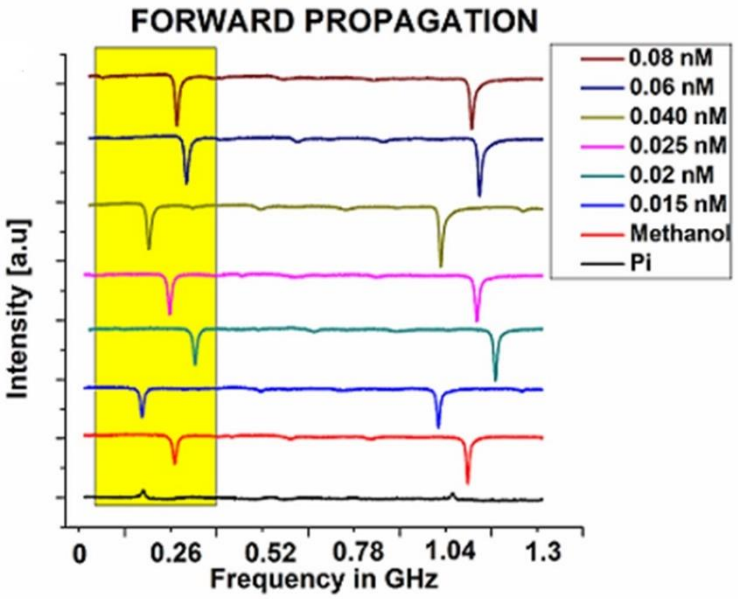

Figure 4.5. Throughput spectra corresponding to different analyte concentrations with an asymmetric tapered fiber being used to couple light into and out of the microresonator; upward shift indicates increasing analyte concentration; bottom trace for methanol only, showing a small throughput peak at $\beta = \pi$.

The mode of interest is highlighted in Fig. 4.5. It is evident from Fig 4.5 that the dip depth of the mode of interest increases with increasing analyte concentration. Initially, with methanol inside the resonator, measurements gave the following values: dip depth $M = 0.0949$, linewidth $\Delta\upsilon = 22.1\ \text{MHz}$, $R_{00} = 0.905$, and $R_{0\pi} = 1.02$. From those parameter values, T_1, $T_2 + \alpha L$, $T_2 m^2$

and dip depth were calculated. Upon introducing analyte (0.015 nM), the dip depth changes. The dip depth corresponding to each analyte concentration was recorded and fitted to the model using Eq. (3.51) with the interacting fraction *f* of the mode being the fitting parameter. The interacting fraction *f* of the mode was calculated to be 0.28 by averaging all the fitting parameters. Knowing the interacting fraction *f* allows us to calculate the corresponding theoretical dip depth for each analyte concentration using Eq. (3.51) which is then compared with the experimentally measured dip depth. It was found that the experimental dip depth agrees well with the calculated (theoretical) dip depth for the highlighted mode in Fig. 4.5. The fact that the dip depth predicted by the model agrees with the experimental dip depth allows us to be very optimistic about our model predictions even though we could not demonstrate the enhancement experimentally at this point. Hence, our results are preliminary. The results demonstrating experimental enhancement will be described in the next section. A summary of other preliminary experiments is shown in Table 6.

Table 6. Summary of preliminary experimental results.

R_{00}	$R_{0\pi}$	f	Predicted enhancement factor
0.905	1.020	0.280	686
0.890	1.030	0.070	483
0.920	1.040	0.188	798

4. 5. Profile 1: Experimental results and analysis for sensing dye absorption

Introduction

A detailed analysis of an experiment performed using an asymmetric (Profile 1) and symmetric tapered fiber (Profile 1) is presented below. The detailed analysis consists of three parts. The first part (steps a, b, and c) compares the experimental enhancement to the predicted theoretical enhancement whereas the second part (steps d and step e) compares the two dissipative sensing signals, one based on fractional change in dip depth and the other one based on the fractional change in linewidth. The third part (step f) compares the absolute sensitivity of the asymmetric tapered fiber coupled microresonator system to an ideal adiabatic tapered fiber coupled microresonator system. The steps involved in the analysis are as follows:

a. Determination of interacting fraction *f* of the mode of interest.

b. For the asymmetric tapered fiber coupled microresonator system using the interacting fraction determined in step a, the theoretical fractional change in dip depth is calculated and later compared with the experimental measurements. The theoretical and experimental values of fractional change in dip depth are plotted as a function of analyte concentration and the slopes of the curves are determined.

c. Now for the symmetric tapered fiber coupled microresonator system, the procedures followed in step b are repeated. The theoretical and experimental values of fractional change in dip depth are plotted as a function of analyte concentration and the slopes of the curves are determined. The experimental enhancement factor is calculated by taking the ratio of slopes of the experimental curves explained in steps b and c.

d. The two dissipative sensing mechanisms are compared in steps d and e: For the asymmetric tapered fiber coupled microresonator system, the theoretical fractional

change in linewidth is calculated and later compared with the experimental measurements. The theoretical and experimental values of fractional change in linewidth are plotted as a function of analyte concentration and the slopes of the curves are determined.

e. Now for the symmetric tapered fiber coupled microresonator system, the procedures followed in step d are repeated. The theoretical and experimental values of fractional change in linewidth are plotted as a function of analyte concentration and the slopes of the curves are determined.

f. Comparison of the absolute sensitivity of an asymmetric tapered fiber coupled microresonator system where multiple modes are incident on the microresonator to the absolute sensitivity of an ideal adiabatic tapered fiber coupled microresonator system where a single mode is incident on the microresonator.

4. 5. a: Determining the interacting fraction *f* of the mode of interest

In this subsection, we present detailed information regarding determining the interacting fraction *f* of the whispering gallery mode of interest. The throughput spectra of a tapered fiber coupled HBR system are shown in Fig. 4.6. A typical HBR used in the experimental results presented in this section and the following two sections has an outer radius of 90 μm and a wall thickness of 15 μm. With an asymmetric tapered fiber $\left(r_w = 1.16\ \mu\text{m}\right)$ used to couple light, WGMs which show a dip at $\beta = 0$ and peak at $\beta = \pi$, and also an increase in dip depth with increasing

analyte concentration were the modes of greater interest for these sensing experiments. A detailed analysis for the whispering gallery mode highlighted in Fig. 4.6 is given below.

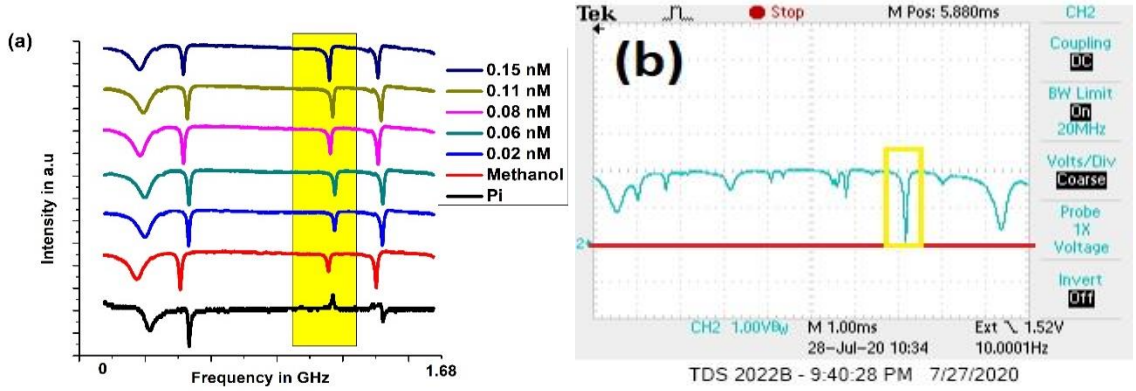

Figure 4.6. Throughput spectra with asymmetric and symmetric tapered fiber of same waist radius, r_w = 1.16 μm. (a) With asymmetic tapered fiber - upward shift indicates increasing analyte concentration; bottom trace for methanol only, $\beta = \pi$. (b) With symmetric tapered fiber – oscilloscope screenshot showing the mode of interest; the red line indicates zero voltage and the mode is very close to critical coupling.

Initially, with methanol inside the resonator, measurements gave the following values: dip depth $M_{00} = 0.035 \pm 0.002$, linewidth $\Delta\upsilon = 13.52 \pm 0.76$ MHz, $R_{00} = 0.965 \pm 0.002$, and $R_{0\pi} = 1.073 \pm 0.002$. From those parameter values, T_1, $T_2 + \alpha L$, $T_1 T_2 m^2$, and dip depth M_{00} were calculated. Values of the dip depth M_{00} and the peak height $R_{0\pi}$ that agree with the measured values were calculated by substituting the values of T_1, $T_2 + \alpha L$, and $T_2 m^2$ into Eq. (3.40) with $\beta = 0$ and $\beta = \pi$ respectively. Based on the input parameters $(R_{00}, R_{0\pi}, \Delta\upsilon)$, the enhancement in sensitivity predicted by the model using Eq. (3.63) was 2135 ± 132. Upon introducing analyte, the dip depth increased. The dip depths corresponding to different analyte concentrations were

recorded and fitted to the model using Eq. (3.51) with the interacting fraction *f* of the mode being the fitting parameter. The values of f for various concentrations which gave the best fits to the experimental data are tabulated and shown in Table 7. The interacting fraction f of the mode was calculated to be 0.062 by averaging all the fitting parameters shown in the table.

Table 7. Fitting parameter *f* for various concentrations.

Concentration in nM	Fitting parameter *f*
0.02	0.062
0.06	0.060
0.08	0.061
0.11	0.066
0.15	0.063

4. 5. b: Dip depth using asymmetric tapered fiber: Theoretical and experimental results

In this subsection, with the asymmetric tapered fiber being used to couple light into and out of the microresonator, we explain both theoretically and experimentally how the fractional change in dip depth varies as a function of analyte concentration. The theoretical and experimental fractional changes in dip depth are plotted as a function of analyte concentration and the slopes of the curves are determined.

The theoretical dip depth of the mode was calculated by substituting the interacting fraction $f = 0.062$, and $\alpha_a = 0.4 \ \frac{\text{m}^{-1}}{\text{nM}}$ in Eq. (3.51). The theoretical dip depth $M(\alpha' L)$ calculation for an analyte concentration of 0.06 nM is shown below. It is worth recalling that upon adding analyte the effective intrinsic loss increases according to the following relation:

$$\alpha' L = \alpha_i L + f\alpha_s L + f\alpha_a L = \alpha L + \Delta\alpha L.$$

For 0.06 nM $\Delta\alpha L = f\alpha_a L = \underset{f}{0.062}\times\underbrace{0.06\times 0.4}_{\alpha_a}\times\underbrace{2\times 3.14\times 90\times 10^{-6}}_{L} = 8.41\times 10^{-7}$ and the corresponding dip depth is given by the following equation,

$$M(\alpha' L) = \frac{4T_1(T_2 + \alpha' L) - 4T_1T_2m^2 - 4(T_1 - T_2 - \alpha' L)\sqrt{T_1T_2}m}{(T_1 + T_2 + \alpha' L)^2},$$

where $T_1 = 1.12 \times 10^{-4}$, $T_2 + \alpha' L = T_2 + \alpha L + f\alpha_a L = 1.18\times 10^{-4} + 8.41\times 10^{-7} = 1.19\times 10^{-4}$, and $T_1T_2m^2 = 1.51\times 10^{-8}$. Thus the theoretical value of dip depth for an analyte concentration of 0.06 nM was found to be 0.049 and the corresponding experimental value was 0.049 ± 0.002. Hence the theoretical and experimental values for fractional change in dip depth $\left(\frac{\Delta M}{M}\right)$ are given by

$$\left(\frac{\Delta M}{M}\right)_{theory} = \frac{0.049 - 0.035}{0.035} = 0.400.$$

$$\left(\frac{\Delta M}{M}\right)_{expt} = \frac{0.049 - 0.035}{0.035} = 0.400.$$

A similar analysis is done for the other dye concentrations and the results are tabulated in Table 8. The corresponding theoretical $\frac{dM}{M}$ values for various analyte concentrations are found using Eq. (3.51) and are also tabulated in Table 8. Throughout the experiment, there are uncertainties associated with every measurement. In our experiment, the main source of uncertainty comes from the finite thickness of the oscilloscope trace which arises from the noises within the system (mechanical noise + detector noise + amplifier noise).

Table 8. Summary of dip depth results. Asymmetric tapered fiber. Profile 1, $f = 0.062$.

Concentration in nM	Measured dip depth M_{expt}	Theoretical dip depth M_{theory}	Percent error $\frac{M_{expt} - M_{the}}{0.01 M_{the}}$	$\left(\frac{\Delta M}{M}\right)_{expt}$	$\left(\frac{\Delta M}{M}\right)_{theory}$	$\left(\frac{dM}{M}\right)_{theory}$
Methanol	0.035 ± 0.002 M_{00}	0.035	0	0 ± 0.065	0	0
0.02	0.039 ± 0.002	0.039	0	0.114 ± 0.081	0.135	0.135
0.06	0.049 ± 0.002	0.049	0	0.400 ± 0.084	0.402	0.406
0.08	0.053 ± 0.002	0.054	1.9	0.514 ± 0.086	0.536	0.541
0.11	0.062 ± 0.002	0.061	-1.6	0.771 ± 0.092	0.734	0.744
0.15	0.071 ± 0.002	0.070	-1.4	1.02 ± 0.099	0.996	1.01

With the asymmetric taper of waist radius 1.16 μm (Profile 1) being used to couple light into and out of the resonator, the fractional change in dip depth is plotted as a function of concentration of analyte as shown in Fig. 4.7. The three curves correspond to the last three columns of Table 8, with error bars reflecting the uncertainties in the experimental results.

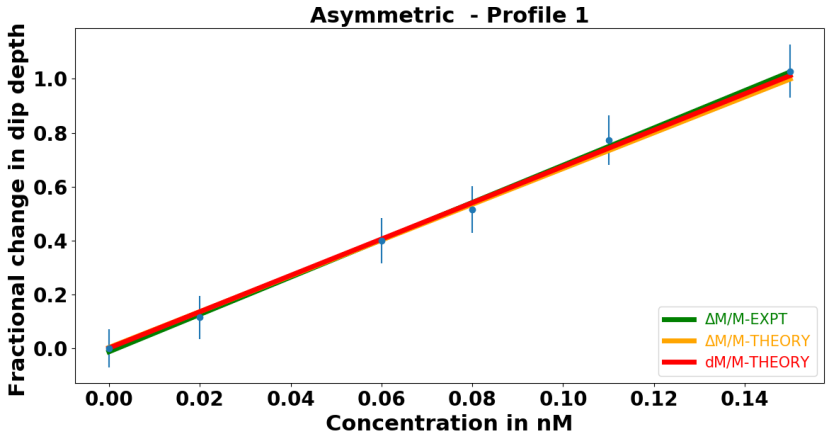

Figure 4.7. Fractional change in dip depth plotted as a function of analyte concentration with the asymmetric tapered fiber used to couple light into and out of the microresonator.

In Fig. 4.7, the green curve represents the best fit to the experimental data points whereas the orange and red curves represent the theoretical models. It is worth recalling that the dip depth, $M = 1 - R,$ is found by measuring the throughput power $(\propto R)$ which is collected on the detector. The mode of interest shown in Fig. 4.6(a) has a small dip depth $(M = 0.065)$ and hence $R = 0.935.$ As we increase the analyte concentration, note that $|\Delta R| = |\Delta M|,$ so even if $\frac{\Delta M}{M}$ is large, $\frac{\Delta R}{R}$ will be small and the experimental data $\frac{\Delta M}{M}$ will depend linearly on the concentration. The slope and *y*-intercept of the linear fit were found to be 6.92 ± 0.68 and 0.01 ± 0.05 using a Python program, which incorporates the experimental error while performing the linear fit. The orange curve $\left(\frac{\Delta M}{M} - theory\right)$ represents the theoretical fractional change in dip depth allowing for nonlinear change in dip depth as a function of concentration and the red curve $\left(\frac{dM}{M} - theory\right)$ represents the theoretical fractional change in dip depth assuming linear change in dip depth as a fucntion of

concentration. It is worth noting that $\frac{\Delta M}{M}$ and $\frac{dM}{M}$ corresponding to various analyte concentrations were calculated using Eq. (3.52) and Eq. (3.41) in Chapter III and were subsequently fitted to a linear curve. The slope of the $\frac{\Delta M}{M} - theory$ curve was found to be 6.64 ± 0.003, and the slope of the $\frac{dM}{M} - theory$ curve was found to be 6.74 ± 0.007. At low concentrations, since $\frac{\Delta M}{M} = \frac{dM}{M}$, the theoretical curves lie on top of each other whereas at higher concentrations $\frac{\Delta M}{M}$ may no longer be equal to $\frac{dM}{M}$. The experimental curve (green) lies on top of both theoretical curves well within the error limits suggesting that our experiment agrees well with the theory.

4. 5. c: Dip depth using symmetric tapered fiber: Theoretical and experimental results

In this subsection, with the symmetric tapered fiber being used to couple light into and out of the microresonator, we explain both theoretically and experimentally how the fractional change in dip depth varies as a function of analyte concentration. The theoretical and experimental fractional changes in dip depth are plotted as a function of analyte concentration and the slopes of the curves are determined. At the end of this subsection, the experimental enhancement factor is calculated and compared with the theoretical prediction (2135 ± 132).

In order to experimentally demonstrate enhancement in absorption sensing, instead of an asymmetric tapered fiber a symmetric tapered fiber of approximately the same waist radius (1. 15 μm) is used to couple light into and out of the HBR filled with methanol. When an asymmetric tapered fiber is replaced by a symmetric tapered fiber, the throughput spectrum for the same mode highlighted in Fig. 4.6 (a) becomes very close to critical coupling as shown in Fig. 4.6 (b). The linewidth of the corresponding mode is measured and found to be 13.36 ± 0.15 MHz. In order to detect any change in the dip depth, we must be looking at the bottom of the dip as we add the known

analyte concentrations to the HBR filled with methanol. While detecting the change in dip depth, the oscilloscope needs to be set on the most sensitive vertical (voltage) scale, which in our case is 2 mV as shown in Fig. 4.8.

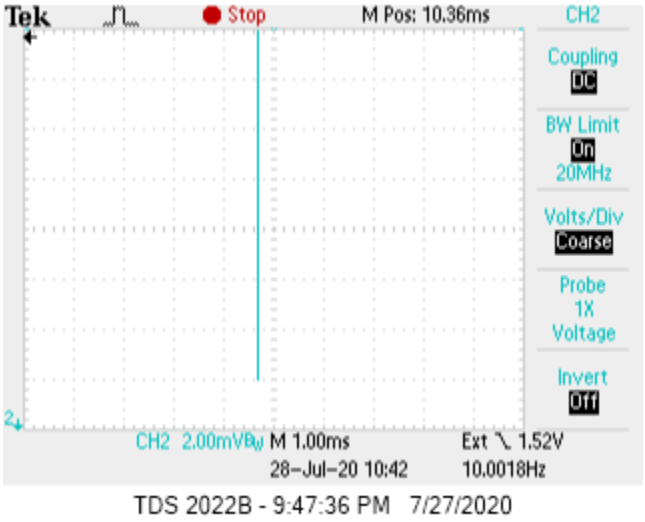

Figure 4.8. Oscilloscope screenshot showing the bottom of the dip (methanol only).

For the oscilloscope Tektronix TDS 2022B, the maximum voltage offset which can be added to the signal is 2 volts. The power of the laser beam is adjusted in such a way that the mode of interest has a dip corresponding to 2 volts. It is worth noting that in Fig. 4.6 (b), for the mode of interest the whole dip corresponds to 2 V. In order to see the bottom of the dip, an offset voltage is introduced, and the bottom of the corresponding dip is shown in Fig. 4.8.

Once the voltage offset knob was adjusted to see the bottom of the dip, analytes of known concentrations were added to the HBR and the change in voltage and hence in dip depth were recorded. Since the scope is set on the most sensitive scale, the bottom of the dip seen on the scope is prone to fluctuations due to changes in fiber-HBR coupling resulting from the air currents and vibrations. Hence, for methanol and other analyte concentrations, while measuring the change in

dip depth, a diligent effort was made to record the deepest fluctuation. After recording the deepest fluctuation for the largest analyte concentration (0.6 nM for the case under consideration), the oscilloscope was set back to its intial vertical scale where the whole dip corresponds to 2V and the linewidth corresponding to the largest analyte concentration was measured. For very low concentrations the change in dip depth (dM) is assumed to be linear with respect to change in analyte concentrations. For very low concentrations, the change in dip depth is not mesaurable. For high concentrations, the change in dip depth is nonlinear. The least measurable ΔM is 0.4 ± 0.2 mV. For 0.6 nM the change in dip depth $\frac{\Delta M}{M} = 2.8\times10^{-3} \pm 0.1\times10^{-3}$ was recorded. The results are tabulated in Table 9.

Table 9. Summary of dip depth results. Symmetric tapered fiber. Profile 1, f = 0.062.

Concentration in nM	$\left(\frac{\Delta M}{M}\right)_{expt}$	$\left(\frac{\Delta M}{M}\right)_{theory}$	$\left(\frac{dM}{M}\right)_{theory}$
0	0	0	0
0.4	$1.6\times10^{-3} \pm 0.1\times10^{-3}$	1.8×10^{-3}	1.3×10^{-3}
0.55	$2.4\times10^{-3} \pm 0.1\times10^{-3}$	2.7×10^{-3}	1.7×10^{-3}
0.6	$2.8\times10^{-3} \pm 0.1\times10^{-3}$	3.0×10^{-3}	1.9×10^{-3}

With a symmetric taper of approximately the same waist radius (1.15 μm) being used to couple light into and out of the resonator, the fractional change in dip depth from Table 9 is plotted

as a function of analyte concentration and is shown in Fig. 4.9. Again,the error bars represent the experimental uncertainties.

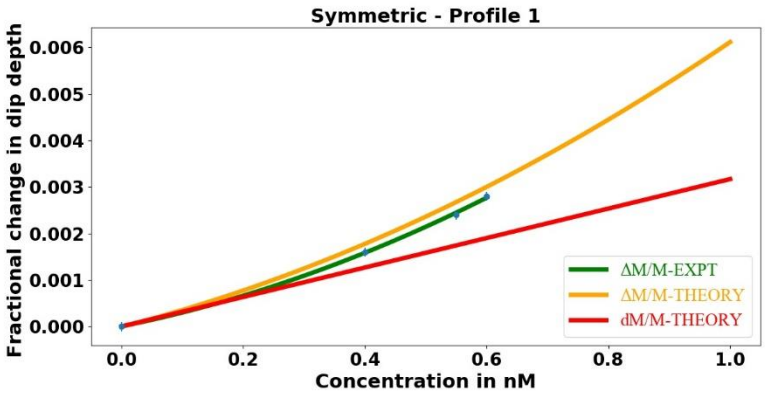

Figure 4.9. Fractional change in dip depth plotted as a function of analyte concentration with the symmetric tapered fiber used to couple light into and out of the microresonator.

In Fig. 4.9, the green curve represents the best fit to the experimental data points whereas the orange and red curves represent the theoretical curves. Once again the best fit is performed by using a Python program. As shown in Fig 4.6 (b), the mode of interest is close to critical coupling and hence has a dip depth M greater than 0.96 and hence $R < 0.04$. Upon increasing the analyte concentration, even if $\frac{\Delta M}{M}$ is small, $\frac{\Delta R}{R}$ may be large, so a quadratic fit $\left(ax^2 + bx + c\right)$ is performed where $a = 0.00327 \pm 0.00156,\ b = 0.00265 \pm 0.00092,\ c = 0.000001 \pm 0.00010.$ The orange curve $\left(\frac{\Delta M}{M} - theory\right)$ which is also a quadratic fit $\left(a = 0.00277 \pm 0.00023,\ b = 0.00336 \pm 0.00002,\ c = 0.000009 \pm 0.000003\right)$ represents the theoretical fractional change in dip depth assuming nonlinear change in dip depth as a function of concentration and the red curve $\left(\frac{dM}{M} - theory\right)$ represents the theoretical fractional change in dip

depth assuming linear change in dip depth as a fucntion of concentration. The slope and *y*-intercept of the linear fit were found to be 0.0032 ± 0.000001 and 0.00000 ± 0.000001. It is worth noting that $\frac{\Delta M}{M} - theory$ curve is calculated by using Eq. (3.52) with m = 0 and $\frac{dM}{M} - theory$ curve is calculated using Eq. (3.42). For very low concentrations, $\frac{\Delta M}{M} = \frac{dM}{M}$ and hence the theoretical curves lie on top of each other in the linear regime whereas at high concentrations $\frac{\Delta M}{M}$ is no longer equal to $\frac{dM}{M}$. At low concentrations, the experimental curve lies on top of the theoretical curves whereas at high concentration, the experimental curve follows the trend of the $\frac{\Delta M}{M} - theory$ curve. This suggests that our experiment agrees well with the theory. The next paragraph explains how the experimental enhancement factor is calculated.

Before we calculate the experimental enhancement factor let us remind ourself that the predicted enhancement factor is 2135 ± 132. In addition, from subsection 1V. 5. b, the slope of fractional change in dip depth versus analyte concentration curve (green curve in Fig. 4.7) with an asymmetric tapered fiber of waist radius 1.16 μm was found to be 6.92 ± 0.68. Also from the above paragraph, we know that at low concentrations the slope of of fractional change in dip depth versus analyte concentration (green curve in Fig. 4.9) with a symmetric tapered fiber of approximately same waist radius 1.15 μm was found to be 0.00265 ± 0.000920. At low concentrations, the experimental enhancement factor can be calculated by taking the ratio of the slopes of the green curves shown in Figs. 4.7 and 4.9. Thus the experimental enhancement is $\frac{6.92 \pm 0.68}{0.00265 \pm 0.000920} \approx 2616 \pm 945$. It is worth recollecting that the predicted enhancement is dependent on the values of R_{00} and $R_{0\pi}$. A slight error in measuring R_{00} and $R_{0\pi}$ due to the system noise will lead to an uncertainty in the predicted enhancment factor calculated by the model.

For example, if there is 0.2 % error in measuring R_{00} and $R_{0\pi}$, then the predicted enhancment will be 2135 ± 132. Once again the uncertainty in experimental enhancement factor arises from the finite thickness of the oscilloscope trace which arises from the noises within the system (mechanical noise + detector noise + amplifier noise). Thus the experimental enhancement agrees with the theoretical enhancement within the limits of uncertainty.

4. 5. d: Linewidth using asymmetric tapered fiber: Theoretical and experimental results

In this subsection, with the asymmetric tapered fiber being used to couple light into and out of the microresonator, we explain both theoretically and experimentally how the fractional change in linewidth varies as a function of analyte concentration. Knowing the slopes of the plots of fractional change in dip depth versus analyte concentration (from subsection IV. 5. b) and fractional change in linewidth versus analyte concentration (from subsection IV. 5. d), will allow us to compare the two disspative sensing mechanisms, i.e, dip depth sensing to linewidth sensing. It is worth remembering that from Eq. (3.68),

$$\eta = \left| \frac{T_2 + \alpha L}{T_1 - T_2 - \alpha L} \frac{\frac{dM}{M}}{\frac{d(\Delta\upsilon)}{(\Delta\upsilon)}} \right| \approx \left| \frac{2}{R_{00} - R_{0\pi}} \right| \frac{4}{M_{00}},$$

where $\left| \frac{T_2 + \alpha L}{T_1 - T_2 - \alpha L} \right| \approx \left| \frac{2}{R_{00} - R_{0\pi}} \right|$ and $\frac{\frac{dM}{M}}{\frac{d(\Delta\upsilon)}{(\Delta\upsilon)}} \approx \frac{4}{M_{00}}$. Since the initial dip depth of the mode of interest (just filled with methanol) $M_{00} = 0.035 \pm 0.002$, the predicted value of $\frac{4}{M_{00}} = 114.3 \pm 6.5$.

Thus for the same analyte concentration, the fractional change in dip depth is predicted to be approximately two orders of magnitude more sensitive than the fractional change in linewidth.

With the asymmetric tapered fiber being used to couple light into and out of the methanol-filled microresonator, the linewidth $\Delta\upsilon$ was found to be 13.52 ± 0.76 MHz. Using Eq. (3.16),

$$\Delta\upsilon = \frac{c}{4\pi^2 na} \times \left(T_1 + T_2 + \alpha L\right).$$

Since the linewidth is linearly proportional to the total loss, as we increase the analyte concentration the effective intrinsic loss αL increases which in turn increases the total loss and the linewidth. It is worth recalling that upon adding analyte the effective intrinsic loss increases according to the following relation:

$$\alpha' L = \alpha_i L + f\alpha_s L + f\alpha_a L = \alpha L + \Delta\alpha L,$$

where $\Delta\alpha L = f\alpha_a L$. Knowing the interacting fraction *f* and the absorption coefficient of the dye α_a allows us to determine the theoretical linewidth. The theoretical linewidth is calculated using the following procedure.

For 0.02 nM $f\alpha_a L = \underset{f}{0.062} \times \underbrace{0.02 \times 0.4}_{\alpha_a} \times \underbrace{2 \times 3.14 \times 90 \times 10^{-6}}_{L} = 2.80 \times 10^{-7}$ and the corresponding theoretical linewidth is given by

$$\Delta\upsilon\left(\alpha' L\right) = \frac{c}{4\pi^2 na} \times \left(T_1 + T_2 + \alpha' L\right), \tag{4.1}$$

where $T_1 = 1.12 \times 10^{-4}$, $T_2 + \alpha' L = T_2 + \alpha L + \left(f\alpha_a L\right) = 1.18 \times 10^{-4} + 2.80 \times 10^{-7} = 1.183 \times 10^{-4}$, $c = 3 \times 10^8 \ \frac{\text{m}}{\text{s}}$, $n = 1.44$, and $a = 90 \times 10^{-6}$ m. Thus the theoretical value of linewidth for an analyte concentration of 0.02 nM was found to be 13.54 MHz and the corresponding experimental

value was 13.65 ± 0.69 MHz. Hence the theoretical and experimental value for fractional change in dip depth $\left(\frac{d\Delta\upsilon}{\Delta\upsilon}\right)$ are given by,

$$\left(\frac{d\Delta\upsilon}{\Delta\upsilon}\right)_{theory} = \frac{13.54 - 13.52}{13.52} = 1.48 \times 10^{-3}.$$

$$\left(\frac{d\Delta\upsilon}{\Delta\upsilon}\right)_{expt} = \frac{13.65 - 13.52}{13.52} = 9.62 \times 10^{-3}.$$

A similar analysis is done for the other dye concentrations and the results are tabulated in Table 10.

Table 10. Summary of linewidth results. Asymmetric tapered fiber. Profile 1, $f = 0.062$.

Concentration in nM	Measured linewidth in MHz $\Delta\upsilon_{\exp t}$	Theoretical linewidth in MHz $\Delta\upsilon_{theory}$	Percent error $\frac{\Delta\upsilon_{\exp t} - \Delta\upsilon_{the}}{\Delta\upsilon_{the}} \times 100$	$\left(\frac{d\Delta\upsilon}{\Delta\upsilon}\right)_{\exp t}$	$\left(\frac{d\Delta\upsilon}{\Delta\upsilon}\right)_{theory}$
Methanol M	13.52 ± 0.76	13.52	0	$0 \pm 7.9\times10^{-2}$	0
0.02	13.65 ± 0.69	13.53	0.88	$9.6\times10^{-3} \pm 7.6\times10^{-2}$	7.3×10^{-4}
0.06	13.73 ± 0.48	13.57	1.17	$1.6\times10^{-3} \pm 6.6\times10^{-2}$	3.6×10^{-3}
0.08	13.76 ± 0.54	13.59	1.25	$1.8\times10^{-2} \pm 6.9\times10^{-2}$	5.2×10^{-3}
0.11	13.81 ± 0.48	13.69	1.47	$2.1\times10^{-2} \pm 6.6\times10^{-2}$	6.6×10^{-3}
0.15	13.95 ± 0.30	13.64	2.27	$3.1\times10^{-2} \pm 6.0\times10^{-2}$	8.8×10^{-3}

With the asymmetric taper of waist radius 1.16 μm (Profile 1) being used to couple light into and out of the resonator, the fractional change in linewidth is plotted as a function of concentration of analyte and is shown in Fig. 4.10. The two curves in Fig. 4.10 correspond to the last 2 columns of Table 10, with the error bars reflecting the uncertainties.

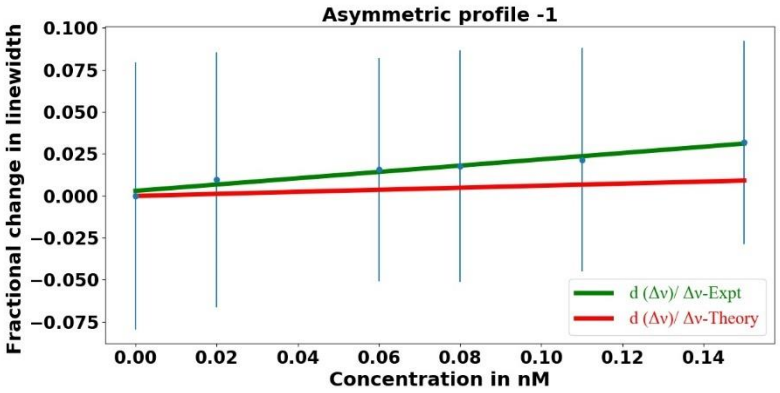

Figure 4.10. Fractional change in linewidth plotted as a function of analyte concentration with the asymmetric tapered fiber used to couple light into and out of the microresonator.

In Fig. 4.10, the green curve represents the best fit to the experimental data points whereas the red curve represents the theoretical curve. The theoretical curve is calculated by using Eq. (4.1). Since the linewidth is linearly proportional to the total loss a linear fit is performed to the experimental data points and theoretical values . For the green curve, the slope and *y*-intercept of the fit were found to be 0.188 ± 0.553 and 0.003 ± 0.052. whereas for the red curve the slope and *y*-intercept were found to be 0.061 ± 0.019 and 0.00009 ± 0.0019. The huge uncertainty in experimental slope arises from the uncertainty in measuring the linewidth which in turn arises from the system noise. The experimental points agree well with the theoretical values with in the error limit. The best fit (linear fit) is performed by using a Python program, which incorporates the experimental error while performing the linear fit. It is also worth noting that throughout the analysis, proper error propagation is followed. For example, the initial linewidth was measured to be 13.52 ± 0.76 MHz and for a concentration of 0.02 nM, the linewidth was measured to be 13.65 ± 0.69 MHz. Upon following proper error propagation, the fractional change in linewidth $\frac{d\Delta\upsilon}{\Delta\upsilon} = 0.0096 \pm 0.0759$. A similar procedure is followed for other analyte concentrations and the results are tabulated in Table 10.

With the asymmetric taper being used to couple light into and out of the microresonator, since we know the slope of the experimental fractional change in dip depth versus analyte concentration from Fig. 4.7 (6.92 ± 0.68), and the slope of experimental fractional change in linewidth versus analyte concentration from Fig. 4.10 (0.188 ± 0.553), we can take the ratio of the slopes and thereby compare the dip depth sensing signal to the linewidth sensing signal experimentally as shown below. The ratio of the slopes is

$$\frac{\frac{dM}{M}}{\frac{d(\Delta\upsilon)}{(\Delta\upsilon)}} = \frac{6.92 \pm 0.68}{0.188 \pm 0.553} = 36.9 \pm 109.$$

It is worth recollecting that the theoretical prediction for $\frac{\frac{dM}{M}}{\frac{d(\Delta\upsilon)}{\Delta\upsilon}} \approx \frac{4}{M_{00}} = 114.3 \pm 6.5$. Thus the experimental results agree with the theoretical results within the limits of uncertainty.

4. 5. e: Linewidth using symmetric tapered fiber: Theoretical and experimental results

In this subsection, with the symmetric tapered fiber being used to couple light into and out of the microresonator, we study the fractional change in linewidth as a function of analyte concentration. Irrespective of whether we use an asymmetric or symmetric tapered fiber of the same waist radius, the predicted change in linewidth of the mode of interest will be the same for the same change in analyte concentration. It is worth remembering that with the symmetric taper being used to couple light into and out of the microresonator, we measure the linewidth only twice, once with zero analyte concentration (just with methanol inside microresonator) and again at the highest concentration which is 0.6 nM for the case under consideration. Knowing the slope of the plot of fractional change in dip depth versus analyte concentration with the asymmetric taper of waist radius 1.16 μm being used to couple light into and out of the microresonator (from subsection

IV. 5. b) and the slope of linewidth versus analyte concentration with a symmetric tapered fiber of approximately the same waist radius (from subsection IV. 5. e) will allow us to compare the two dissipative sensing mechanisms.

With the symmetric taper being used to couple light into and out of the methanol – filled microresonator, the initial linewidth of the mode was found to be 13.36 ± 0.15 MHz. Ideally one would expect the linewidth to be the same as with the asymmetric taper. But in reality up to a 10% difference in linewidth is acceptable since we can't be sure that the asymmetric and symmetric tapers fabricated in our taper puller system have exactly the same waist radius. For an analyte concentration of 0.6 nM, the linewidth of the mode was found to be 13.93 ± 0.21 MHz.

A plot of fractional change in linewidth $\frac{d(\Delta\upsilon)}{\Delta\upsilon}$ as a function of analyte concentration with the symmetric taper being used to couple light into and out of the microresonator is shown in Fig. 4.11.

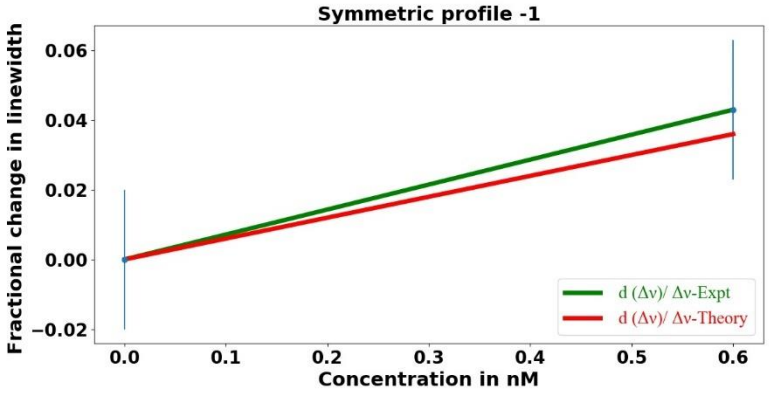

Figure 4.11. Fractional change in linewidth plotted as a function of analyte concentration with the symmetric tapered fiber used to couple light into and out of the microresonator.

In Fig 4.11, the green curve represents the best fit to the experimental data points whereas the red curve represents the theoretical model. For the green curve, the slope and *y*-intercept of the best fit are given by 0.072 ± 0.033 and 0.000 ± 0.033. For the red curve, the slope and *y*-intercept are given by 0.06 and 0.00.

With the asymmetric taper being used to couple light into and out of the microresonator, since we know the slope of the experimental fractional change in dip depth versus analyte concentration from Fig. 4.7 (6.92 ± 0.68), and the slope of experimental fractional change in linewidth versus analyte concentration from Fig. 4.11 (0.072 ± 0.033), we can take the ratio of the slopes and thereby compare the dip depth sensing signal to the linewidth sensing signal experimentally as shown below:

$$\frac{\frac{dM}{M}}{\frac{d(\Delta\upsilon)}{\Delta\upsilon}} = \frac{6.92 \pm 0.68}{0.072 \pm 0.033} = 97 \pm 46.$$

It is worth recollecting that the theoretical prediction for $\frac{\frac{dM}{M}}{\frac{d(\Delta\upsilon)}{\Delta\upsilon}} \approx \frac{4}{M_{00}} = 114.3 \pm 6.5$. As shown in subsection IV. 5. d, with the asymmetric tapered fiber being used, $\frac{\frac{dM}{M}}{\frac{d\Delta\upsilon}{\Delta\upsilon}}$ was found to be 36.9 ± 109 and with the symmetric taper being used, $\frac{\frac{dM}{M}}{\frac{d\Delta\upsilon}{\Delta\upsilon}}$ was found to be 97 ± 46. It is worth noting that for the range of concentrations (0 – 0.15 nM) shown in Table 10, with the asymmetric taper being used to couple light into and out of the microresonator, the measured fractional change in linewidth is smaller than the uncertainty in measuring the fractional change in linewidth and this

accounts for the large uncertainty (±109). With the symmetric tapered fiber being used to couple light into and out of the microresonator, since the linewidth is measured at higher concentration (0 and 0.6 nM), the measured fractional change in linewidth is smaller than the uncertainty in measuring fractional change in linewidth and this accounts for the smaller uncertainty (±46). In both cases, the experimental value found for $\frac{\frac{dM}{M}}{\frac{d(\Delta\upsilon)}{\Delta\upsilon}}$ with asymmetric and symmetric tapered fiber agrees well with the theory within the error limits. In addition, it is worth noting that there can be some uncertainty in the concentration. But this uncertainty is more of a scale factor and arises from the uncertainty in making the intial dye solution.

4. 5. f: Absolute sensitivity

In this subsection, instead of dip depth sensitivity *enhancement* we will compare the *absolute* senstivity of an asymmetric tapered fiber microresonator system with multiple modes incident on the microresonator to an ideal adiabatic tapered fiber coupled microresonator system where a single mode is incident on the microresonator. It is worth remembering that "ideal" refers to a fiber waist radius that is not equal to that in the multimode case, but is chosen in such a way that Q can be as large as possible. As discussed before in Chapter III, for the two tapered fiber coupled microresonator systems (asymmetric tapered fiber coupled and ideal adiabatic tapered fiber coupled),for equal absolute sensitivity,

$$Q_i \simeq \frac{4}{M_{00}}\left|\frac{1+x}{1-x}\right| Q \geq \frac{4}{M_{00}} Q,$$

where Q_i refers to the intrinsic quality factor and x refers to the ratio of outcoupling loss to effective intrinsic loss. When the mode excited with a single mode input is strongly undercoupled or overcoupled, then Eq. (3.72) becomes

$$(Q_i)_{\min} \simeq \frac{4}{M_{00}} Q. \tag{4.2}$$

Since $\frac{4}{M_{00}} = \frac{4}{0.035} = 114.3$ and $Q = 1.43 \times 10^7$, then using Eq. (4.2), $(Q_i)_{\min} = 1.43 \times 10^7 \times 114.3 = 1.64 \times 10^9$. An intrinsic quality factor of the order of 10^9 is near the limit of what can be achieved in fused silica without taking extraordinary measures. It is worth noting that, if the mode excited using ideal adiabatic tapered fiber is not strongly undercoupled or overcoupled, then for absolute sensitivity to be equal, the value of Q_i needs to be greater than 1.64×10^9 for the case under consideration.

A summary of a set of experiments (like the one described above) performed using Profile 1, which validate our model predictions, is provided at the end of this chapter in Table 11. The next two sections provide a brief summary of similar experiments performed using Profile 2 and Profile 3.

4. 6. Profile 2: Summary of experimental results and analysis for sensing dye absorption

Introduction

The summary of an experiment performed using an asymmetric (Profile 2) and symmetric tapered fiber (Profile 2) is presented below. Similar to section IV. 5, this section is divided into six subsections. Even though the steps described in the introduction part of section IV. 5 are followed while performing the analysis in section IV. 6 and IV. 7, we provide only minimum relevant information (such as the values of $R_{00}, R_{0\pi}, M_{00}, \Delta\upsilon$ and the slopes of the experimental curves) for comparing the experimental and theoretical enhancement factors, the two dissipative sensing signals, and the absolute sensitivity with the model predictions.

4. 6. a: Determining the interacting fraction *f* of the mode of interest

In this subsection, we present the values of the input parameters for our model, the initial dip depth and linewidth of the mode of interest, and the interacting fraction *f* of the whispering gallery mode of interest. The throughput spectra of asymmetric and symmetric tapered fiber coupled HBR systems are shown in Fig. 4.12 (a) and Fig. 4.12 (b). Initially, with methanol inside the resonator, measurements gave the following values: dip depth $M_{00} = 0.073 \pm 0.002$, linewidth $\Delta\upsilon = 21.55 \pm 0.62$ MHz, $R_{00} = 0.927$, and $R_{0\pi} = 1.030$. Based on the input parameters $(R_{00}, R_{0\pi})$, the enhancement in sensitivity predicted by the model was 1020 ± 38. The dip depth corresponding to each analyte concentration was recorded and fitted to the model with the interacting fraction *f* of the mode being the fitting parameter. The interacting fraction *f* of the mode was calculated to be 0.110 by averaging all the fitting parameters.

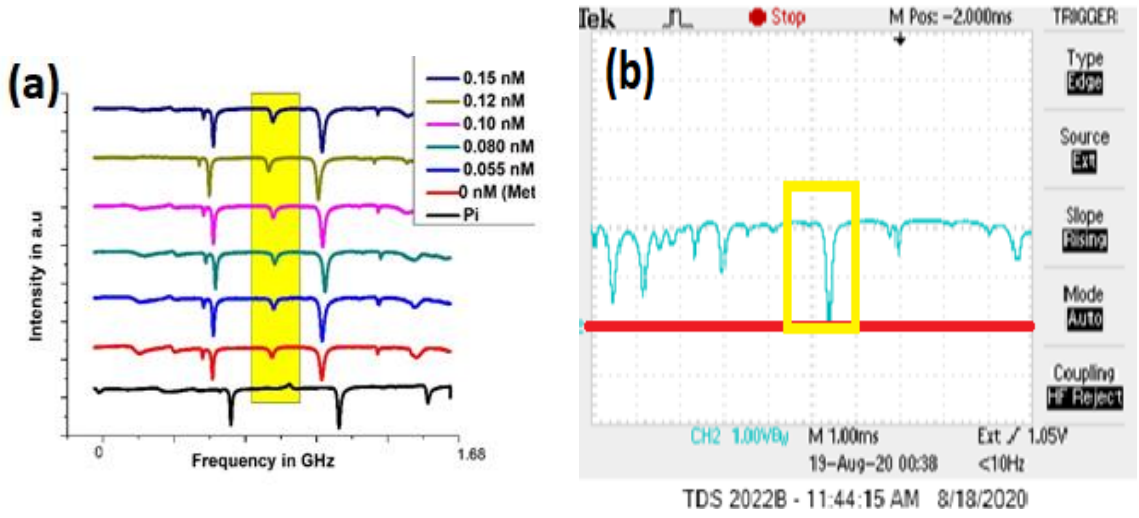

Figure 4.12. Throughput spectra with asymmetric and symmetric tapered fiber of same waist radius, r_w = 1.47 µm. (a) With asymmetic tapered fiber – upward shift indicates increasing analyte concentration; bottom trace for methanol only, $\beta = \pi$. (b) With symmetric tapered fiber – oscilloscope screenshot showing the mode of interest; the red line indicates zero voltage and the mode is very close to critical coupling.

4. 6. b: Fractional change in dip depth using asymmetric tapered fiber

In this subsection, with the asymmetric tapered fiber being used to couple light into and out of the microresonator, the slope of fractional change in dip depth versus analyte concentration is determined. With the asymmetric taper of waist radius 1.47 μm being used to couple light into and out of the resonator, the relative change in dip depth is plotted as a function of analyte concentration and is shown in Fig. 4.13. In Fig. 4.13, the green curve represents the best fit to the experimental data points whereas the orange and red curves represent the theoretical model. The slope of the best fit performed by using a Python program was found to be 3.16 ± 0.51.

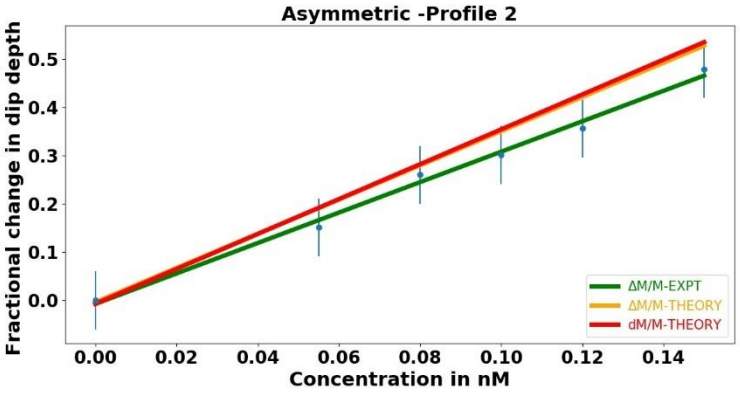

Figure 4.13. Fractional change in dip depth plotted as a function of analyte concentration with the asymmetric tapered fiber used to couple light into and out of the microresonator.

4. 6. c: Fractional change in dip depth using symmetric tapered fiber

In this subsection, with the symmetric tapered fiber being used to couple light into and out of the microresonator, the slope of fractional change in dip depth versus analyte concentration is determined. At the end of this subsection, the experimental enhancement factor is calculated and compared with the model prediction (1020 ± 38). With the symmetric taper of the same waist

radius 1.47 μm being used to couple light into and out of the resonator, the fractional change in dip depth is plotted as a function of analyte concentration and is shown in Fig. 4.14.

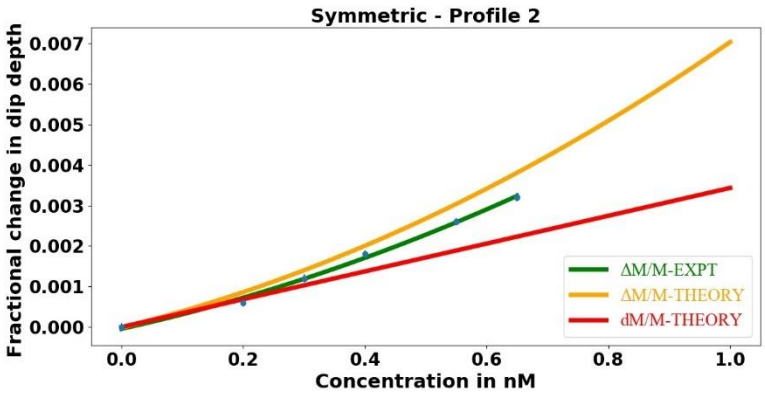

Figure 4.14. Fractional change in dip depth plotted as a function of analyte concentration with the symmetric tapered fiber used to couple light into and out of the microresonator.

In Fig. 4.14, the green curve represents the best fit to the experimental data points whereas the orange and red curves represent the theoretical model. A quadratic fit is performed to the experimental data points using a python program. The parameters of the quadratic fit are given by

$$a = 0.002681 \pm 0.000924, \quad b = 0.003302 \pm 0.000638, \quad c = 0.000043 \pm 0.000096.$$

It is worth recalling that the enhancement in sensitivity predicted by the model was 1020 ± 38. At low concentrations, the experimental enhancement factor can be calculated by taking the ratios of slopes of Fig. 4.13 and Fig. 4.14. Thus the experimental enhancement is $\frac{3.16 \pm 0.51}{0.003302 \pm 0.000638} \approx 956 \pm 240$. Once again, the uncertainty in experimental enhancement factor arises from the finite thickness of the oscilloscope trace which arises from the noises within the system (mechanical noise + detector noise + amplifier noise). The experimental enhancement agrees with the theoretical enhancement within the limits of uncertainty.

4. 6. d: Fractional change in linewidth using asymmetric tapered fiber

In this subsection, with the asymmetric tapered fiber being used to couple light into and out of the microresonator, the slope of fractional change in linewidth versus analyte concentration is determined and the two dissipative sensing signals are compared. Since the initial dip depth of the mode of interest (just filled with methanol) $M_{00} = 0.073 \pm 0.002$, the predicted value of $\frac{4}{M_{00}}$ which is approximately the ratio of fractional change in dip depth to the fractional change in linewidth is equal to 54.8 ± 1.5. Thus for the same analyte concentration, the fractional change in dip depth is predicted to be more than one order of magnitude more sensitive than the fractional change in linewidth for the case under consideration.

With the asymmetric taper of waist radius 1.47 μm being used to couple light into and out of the resonator, the fractional change in linewidth is plotted as a function of analyte concentration and is shown in Fig. 4.15.

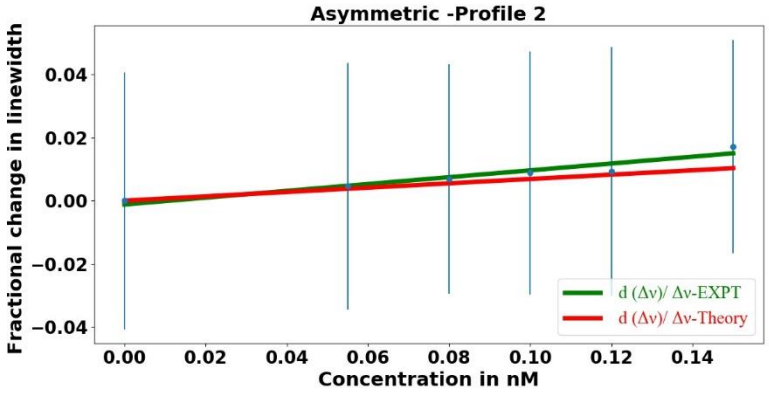

Figure 4.15. Fractional change in linewidth plotted as a function of analyte concentration with the asymmetric tapered fiber used to couple light into and out of the microresonator.

In Fig. 4.15, the green curve represents the best fit to the experimental data points whereas the red curve represents the theoretical curve. A linear fit is performed to the experimental data points using a python program. The slope of the fit was found to be 0.108 ± 0.323. Knowing the slopes of the experimental curves shown in Fig. 4.13 and Fig. 4.15 with the asymmetric taper being used to couple light into and out of the microresonator, allows us to compare the two sensing mechanisms. Therefore,

$$\frac{\frac{dM}{M}}{\frac{d(\Delta\upsilon)}{(\Delta\upsilon)}} = \frac{3.16 \pm 0.51}{0.108 \pm 0.323} = 29.1 \pm 87.2.$$

Since the theoretical prediction for $\frac{\frac{dM}{M}}{\frac{d(\Delta\upsilon)}{\Delta\upsilon}} \approx \frac{4}{M_{00}} = 54.8 \pm 1.5$, the experimental results agrees with the theoretical results within the limits of uncertainty.

4. 6. e: Fractional change in linewidth using symmetric tapered fiber

In this subsection, with the symmetric tapered fiber being used to couple light into and out of the microresonator, the slope of fractional change in linewidth versus analyte concentration is determined and the two dissipative sensing signals are compared.

A plot of fractional change in linewidth $\frac{d(\Delta\upsilon)}{\Delta\upsilon}$ as a function of analyte concentration with the symmetric taper being used to couple light into and out of the microresonator is shown in Fig. 4.16. The slope of the best fit is given by 0.073 ± 0.050. Hence $\frac{\frac{dM}{M}}{\frac{d(\Delta\upsilon)}{\Delta\upsilon}} = \frac{3.16 \pm 0.51}{0.073 \pm 0.050} = 43.1 \pm 30.1$. It is worth recalling that the theoretical prediction for $\frac{4}{M_{00}}$

is 54.8 ± 1.5. Thus the experimental value found for $\frac{\frac{dM}{M}}{\frac{d(\Delta\upsilon)}{\Delta\upsilon}}$ with symmetric tapered fiber agrees well with the theory within the error limits. In both cases (with asymmetric and symmetric taperd fiber of approximately same waist radius), the experimental value found for $\frac{\frac{dM}{M}}{\frac{d(\Delta\upsilon)}{\Delta\upsilon}}$ with asymmetric and symmetric tapered fiber agrees well with the theory within the error limits.

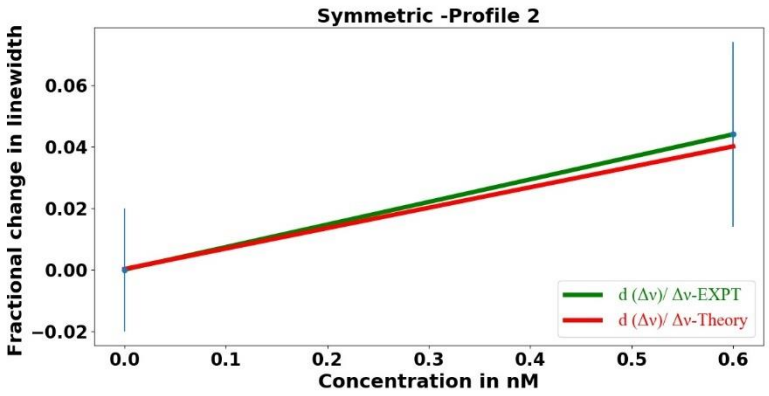

Figure 4.16. Fractional change in linewidth plotted as a function of analyte concentration with the symmetric tapered fiber used to couple light into and out of the microresonator.

4. 6. f: Absolute sensitivity

In this subsection, instead of dip depth sensitivity *enhancement* we will compare the *absolute* senstivity of an asymmetric tapered fiber microresonator system with multiple modes incident on the microresonator to an ideal adiabatic tapered fiber coupled microresonator system where a single mode is incident on the microresonator.

Since the initial linewidth of the mode was 21.55 ± 0.62 MHz, the quality factor Q is equal to 9.0×10^{6}. Thus using Eq. (3.71), for equal absolute sensitivity, the minimum intrinsic quality factor of an ideal adiabatic tapered fiber coupled microresonator system is given by

$$\left(Q_i\right)_{\min} = Q \times \frac{4}{M_{00}} = 9.0 \times 10^6 \times 54.8 = 4.9 \times 10^8.$$

It is worth remembering that an intrinsic quality factor of the order of 10^9 is near the limit of what can be achieved in fused silica without taking extraordinary measures.

A summary of a set of experiments (like the one described above) performed using Profile 2, which validate our model predictions, is provided at the end of this chapter in Table 11. The next section provides a brief summary of similar experiments performed using Profile 3.

4. 7. Profile 3: Summary of experimental results and analysis for sensing dye absorption

Introduction

The summary of an experiment performed using an asymmetric (Profile 3) and symmetric tapered fiber (Profile 3) is presented below. Similar to section IV. 5 and IV. 6, this section is divided into six subsections.

4. 7. a: Determining the interacting fraction *f* of the mode of interest

In this subsection, we present the values of the input parameters for our model, the initial dip depth and linewidth of the mode of interest, and the interacting fraction *f* of the whispering gallery mode of interest. The throughput spectra of an asymmetric and symmetric tapered fiber coupled HBR system are shown in Fig. 4.17 (a) and Fig. 4.17 (b). Initially, with methanol inside the resonator, measurements gave the following values: dip depth $M_{00} = 0.064 \pm 0.002,$ linewidth $\Delta\upsilon = 17.42 \pm 0.56$ MHz, $R_{00} = 0.936,$ and $R_{0\pi} = 1.040.$ Based on the input parameters $\left(R_{00}, R_{0\pi}\right),$ the enhancement in sensitivity predicted by the model was 1166 ± 47. The dip depth corresponding to each analyte concentration was recorded and fitted to the model with the

interacting fraction *f* of the mode being the fitting parameter. The interacting fraction *f* of the mode was calculated to be 0.077 by averaging all the fitting parameters.

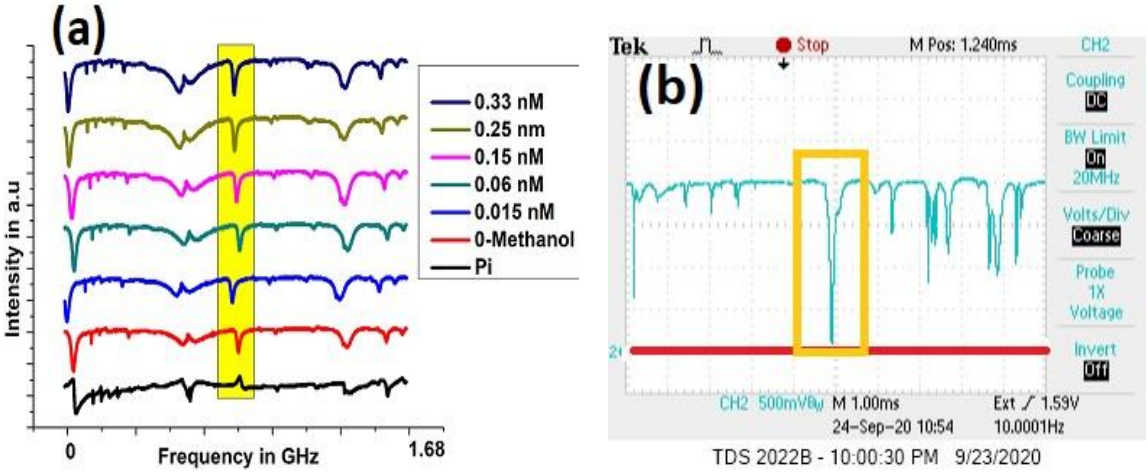

Figure 4.17. Throughput spectra with asymmetric and symmetric tapered fiber of same waist radius, r_w = 1.16 µm. (a) With asymmetic tapered fiber – upward shift indicates increasing analyte concentration; bottom trace for methanol only, $\beta = \pi$. (b) With symmetric tapered fiber – oscilloscope screenshot showing the mode of interest; the red line indicates zero voltage and the mode is very close to critical coupling.

4. 7. b: Fractional change in dip depth using asymmetric tapered fiber

In this subsection, with the asymmetric tapered fiber being used to couple light into and out of the microresonator, the slope of fractional change in dip depth versus analyte concentration is determined. With the asymmetric taper of waist radius 1.16 µm being used to couple light into and out of the resonator, the relative change in dip depth is plotted as a function of analyte concentration and is shown in Fig. 4.18.

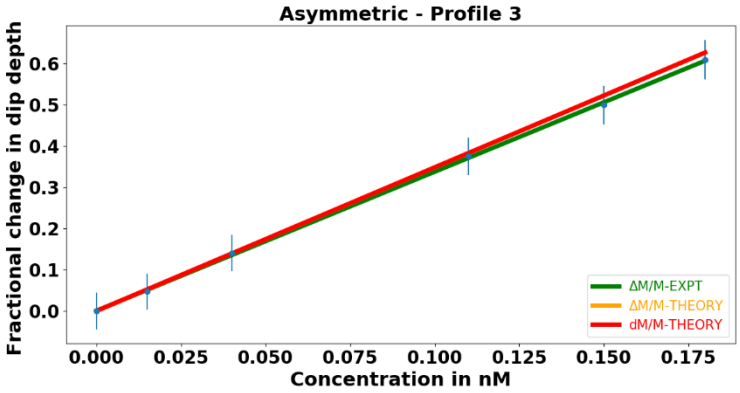

Figure 4.18. Fractional change in dip depth plotted as a function of analyte concentration with the asymmetric tapered fiber used to couple light into and out of the microresonator.

In Fig. 4.18, the green curve represents the best fit to the experimental data points whereas the orange and red curves represent the theoretical model. The slope of the best fit performed by using a Python program was found to be 3.37 ± 0.28.

4. 7. c: Fractional change in dip depth using symmetric tapered fiber

In this subsection, with the symmetric tapered fiber being used to couple light into and out of the microresonator, the slope of fractional change in dip depth versus analyte concentration is determined. At the end of this subsection, the experimental enhancement factor is calculated and compared with the model prediction (1166 ± 47). With the symmetric taper of the same waist radius 1.16 μm being used to couple light into and out of the resonator, the fractional change in dip depth is plotted as a function of analyte concentration and is shown in Fig. 4.19. In Fig. 4.19, the

green curve represents the best fit to the experimental data points whereas the orange and red curves represent the theoretical model. A quadratic fit is performed to the experimental data points using a python program. The parameters of the quadratic fit are given by $a = 0.001779 \pm 0.001740,\ b = 0.003081 \pm 0.000898,\ c = 0.000022 \pm 0.000096.$

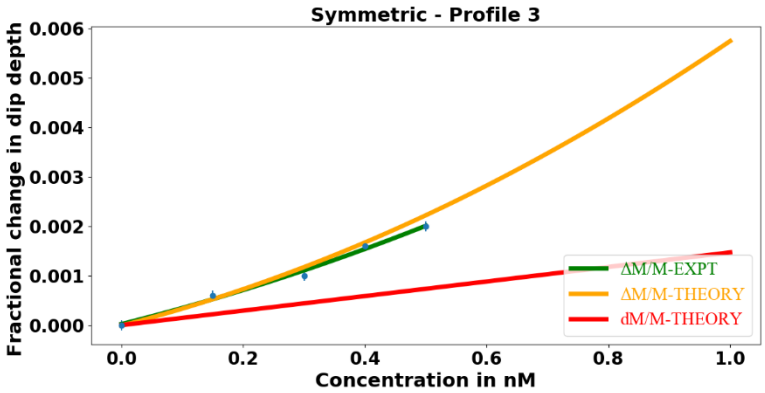

Figure 4.19. Fractional change in dip depth plotted as a function of analyte concentration with the symmetric tapered fiber used to couple light into and out of the microresonator.

It is worth recalling that the enhancement in sensitivity predicted by the model was 1166 ± 47. At low concentrations, the experimental enhancement factor can be calculated by taking the ratios of slopes of Fig. 4.18 and Fig. 4.19. Thus the experimental enhancement is $\frac{3.37 \pm 0.28}{0.003081 \pm 0.000898} \approx 1094 \pm 331.$ The experimental enhancement agrees with the theoretical enhancement within the limits of uncertainty.

4. 7. d: Fractional change in linewidth using asymmetric tapered fiber

In this subsection, with the asymmetric tapered fiber being used to couple light into and out of the microresonator, the slope of fractional change in linewidth versus analyte concentration is determined and the two dissipative sensing signals are compared. Since the initial dip depth of

mode of interest (just filled with methanol) $M_{00} = 0.064 \pm 0.002$, the predicted value of $\frac{4}{M_{00}}$ which is approximately the ratio of fractional change in dip depth to the fractional change in linewidth is equal to 62.5 ± 2. With the asymmetric taper of waist radius 1.16 µm being used to couple light into and out of the resonator, the fractional change in linewidth is plotted as a function of analyte concentration and is shown in Fig. 4.20.

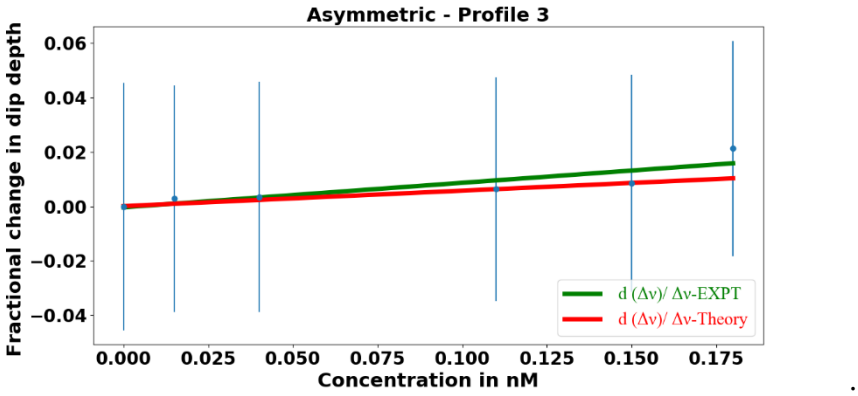

Figure 4.20. Fractional change in linewidth plotted as a function of analyte concentration with the asymmetric tapered fiber used to couple light into and out of the microresonator.

In Fig. 4.20, the green curve represents the best fit to the experimental data points whereas the red curve represents the theoretical curve. A linear fit is performed to the experimental data points using a python program. The slope of the fit was found to be 0.089 ± 0.248.

Knowing the slopes of experimental curves shown in Fig. 4.18 and Fig. 4.20 with the asymmetric taper being used to couple light into and out of the microresonator, allows us to compare the two sensing mechanisms. Therefore,

$$\frac{\frac{dM}{M}}{\frac{d(\Delta\upsilon)}{(\Delta\upsilon)}} = \frac{3.37 \pm 0.28}{0.089 \pm 0.248} = 37.5 \pm 103.4.$$

It is worth recollecting that the theoretical prediction for $\frac{\frac{dM}{M}}{\frac{d(\Delta\upsilon)}{\Delta\upsilon}} \approx \frac{4}{M_{00}} = 62.5 \pm 2.$ Thus the experimental results agrees with the theoretical results within the limits of uncertainty.

4. 7. e: Fractional change in linewidth using symmetric tapered fiber

In this subsection, with the symmetric tapered fiber being used to couple light into and out of the microresonator, the slope of fractional change in linewidth versus analyte concentration curve is determined and the two dissipative sensing signals are compared.

A plot of fractional change in linewidth $\frac{d(\Delta\upsilon)}{\Delta\upsilon}$ as a function of analyte concentration with the symmetric taper being used to couple light into and out of the microresonator is shown in Fig. 4.21.

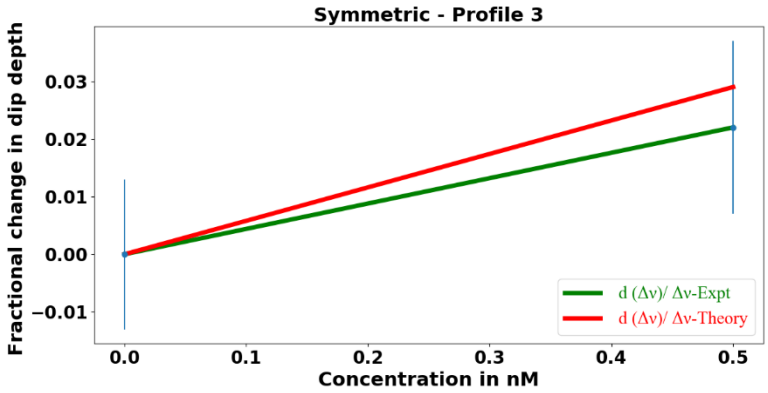

Figure 4.21. Fractional change in linewidth plotted as a function of analyte concentration with the symmetric tapered fiber used to couple light into and out of the microresonator.

The slope of the best fit is given by 0.044 ± 0.030. Hence $\frac{\frac{dM}{M}}{\frac{d(\Delta\upsilon)}{\Delta\upsilon}} = \frac{3.37 \pm 0.28}{0.044 \pm 0.030} = 76.6 \pm 52.6$. It is worth recalling that the theoretical prediction for $\frac{4}{M_{00}}$ is 62.5 ± 2. Thus the experimental value found for $\frac{\frac{dM}{M}}{\frac{d(\Delta\upsilon)}{\Delta\upsilon}}$ with both asymmetric and symmetric tapered fiber agrees well with the theory within the error limits. In both cases (with asymmetric and symmetric tapered fiber of approximately the same waist radius), the experimental value found for $\frac{\frac{dM}{M}}{\frac{d(\Delta\upsilon)}{\Delta\upsilon}}$ with asymmetric and symmetric tapered fiber agrees well with the theory within the error limits.

4. 7. f: Absolute sensitivity

In this subsection, instead of dip depth sensitivity *enhancement* we will compare the *absolute* senstivity of an asymmetric tapered fiber microresonator system with multiple modes incident on the microresonator to an ideal adiabatic tapered fiber coupled microresonator system where a single mode is incident on the microresonator.

Comparing the absolute sensitivity using Eq. (3.71), the minimum intrinsic quality factor is given by

$$\left(Q_i\right)_{\min} = Q \times \frac{4}{M_{00}} = 1.1 \times 10^7 \times 62.5 = 6.96 \times 10^8.$$

Once again, it is worth noticing that the absolute sensitivity which can be obtained by a mode with an intrinsic quality factor of the order of 10^9 in an ideal adiabatic tapered fiber coupled microresonator system, can be easily achieved by a mode of quality factor of the order of 10^7 in an asymmetric tapered fiber coupled microresonator system. In addition, it is much easier to fabricate a mode of quality factor 10^7 than a mode of intrinsic quality factor 10^9 in a fused silica microresonator.

A summary of another experiment performed using Profile 3, which validates the enhancement predicted by the model is provided at the end of this chapter in Table 11.

Table 11. Summary of results – Comparison of theory and experiment

		Enhancement		Comparison of dissipative sensing mechanisms			Comparison of absolute sensitvity	
Taper Profile	f	Theory	Exp	$\frac{\left(\frac{\Delta M}{M}\right)_{asy}}{\left(\frac{d\Delta\upsilon}{\Delta\upsilon}\right)_{asy}}$ Exp	$\frac{\left(\frac{\Delta M}{M}\right)_{asy}}{\left(\frac{d\Delta\upsilon}{\Delta\upsilon}\right)_{sym}}$ Exp	$\frac{4}{M_{00}}$ Theory	Q	$(Q_i)_{\min}$
1	0.062	2135 ± 132	2616 ± 945	36.9 ± 109	97 ± 46	114.3 ± 6.5	1.43×10^7	1.64×10^9
1	0.070	5548 ± 500	4286 ± 1467	42.3 ± 274	171 ± 71	149 ± 11	1.29×10^7	1.92×10^9
1	0.052	1398 ± 62	2258 ± 931	35 ± 161	49 ± 12	45 ± 1	1.62×10^7	7.3×10^8
1	0.070	1298 ± 55	1476 ± 416	18 ± 30	NA	67 ± 2	1.28×10^7	8.58×10^8
1	0.195	948 ± 34	1285 ± 359	7 ± 11	NA	49 ± 1.2	1.45×10^7	7.1×10^8
1	0.19	398 ± 9	417 ± 231	10.8 ± 25	NA	30.6 ± 0.5	3.59×10^6	1.09×10^8
2	0.110	1020 ± 38	956 ± 240	29.1 ± 87.2	43.1 ± 30.1	54.8 ± 1.5	9.0×10^6	4.9×10^8
2	0.128	639 ± 19	735 ± 159	29.1 ± 87.2	43.4 ± 36	44.9 ± 1.0	1.15×10^7	5.2×10^8
2	0.156	729 ± 23	886 ± 247	20.4 ± 22	45 ± 36	43.5 ± 0.94	8.5×10^6	3.7×10^8
3	0.077	1166 ± 47	1094 ± 331	37.5 ± 103.4	76.6 ± 52.6	62.5 ± 2	1.1×10^7	6.96×10^8
3	0.053	509 ± 33.4	545 ± 151	15 ± 25	37 ± 13	38 ± 0.70	2.5×10^7	9.5×10^8

For three different taper profiles, based on column 3 and 4 of Table 11, we can say that the experimental enhancement factor agrees with the theoretical enhancement factor well within the error limits. As mentioned before, the uncertainty in experimental enhancement factor arises from the noises within the system. For all the 11 cases, the interacting fraction (evanescent fraction) of the WGM was calculated and is shown in column 2. Based on the agreement between experimental and theoretical enhancement factor for all the cases, we can say that a novel sensing technique for enhancing the sensitivity of dip depth based dissipative sensing has been developed and an enhancement by three orders of magnitude is demonstrated.

Based on the results shown in columns 5, 6, and 7 we can compare the two dissipative sensing mechanisms. Theoretically, for the same change in analyte concentration, the ratio of fractional change in dip depth to the fractional change in linewidth was found to be approximately equal to $\frac{4}{M_{00}}$. In most of the cases shown in Table 11, the ratio of fractional change in dip depth to fractional change in linewidth with both asymmetric and symmetric taper being used to couple light into and out of the microresonator agrees well with the theoretical prediction $\left(\frac{4}{M_{00}}\right)$ within the error limits. Out of 11 cases shown in Table 11, 9 cases agree with the theoretical prediction and hence we can say that dip depth based dissipative sensing is more sensitive than linewidth based dissipative sensing by more than one order of magnitude.

In columns 8 and 9, we compare the absolute sensitivity of an asymmetric tapered fiber coupled microresonator system with multimode input to the absolute sensitivity of an ideal adiabatic tapered fiber coupled microresonator system where a single fiber mode is incident on the microresonator. The absolute sensitivity of an asymmetric tapered fiber coupled microresonator system with a quality factor (Q~10^7) was found to be comparable to the to the absolute sensitivity

of an ideal adiabatic tapered fiber coupled microresonator system with a Q approximately equal to 10^9.

CHAPTER V

CONCLUSIONS AND FUTURE WORK

5.1. Summary

A n**o**vel technique for enhancing the sensitivity of dip-depth based dissipative sensing is presented in this dissertation. The enhancement demonstrated in this dissertation is achieved by having multiple fiber modes incident on the microresonator using an asymmetric tapered fiber. Having multimode input produces an enhancement of approximately three orders of magnitude in the sensitivity of dissipative dip-depth based sensing compared to the sensitivity achieved using single-mode input from a coupling fiber with the same waist radius. The highlights of this technique are as follows:

i. The enhancement is independent of the quality factor *Q* of the mode.

ii. The enhancement does not depend on the input and output couplings being equal or the wavelength or the refractive index or the size of the microresonator.

iii. The dissipative sensing signal based on dip-depth change is significantly (approximately two orders of magnitude) more sensitive than the dissipative sensing signal based on the change in linewidth.

iv. An absolute sensitivity comparable to that achievable by using a high Q mode (10^9) of an ideal adiabatic tapered fiber coupled microresonator system can be achieved by using an asymmetric tapered fiber microresonator system with multiple modes incident on the resonator with a much more easily produced value of Q (~10^7).

v. The ability to determine the interacting fraction f of the WGM of interest.

As mentioned before, an enhancement in sensitivity was achieved by using an asymmetric tapered fiber with a non-adiabatic downtaper and adiabatic uptaper. In chapter II, a precise fabrication and careful characterization of asymmetric tapered fibers with non-adiabatic downtaper and adiabatic uptaper was presented. A model for predicting the radius of the waist of an asymmetric tapered fiber with a non-adiabatic downtaper and an adiabatic uptaper was developed. Usually, the delineation curve determines whether a taper transition is adiabatic or non-adiabatic. The usual criterion for adiabaticity of a taper transition is that the slope of the taper at any point should be less than the radius at that point divided by 2π and multiplied by the difference of propagation constants of the fundamental HE_{11} mode and the higher-order mode most likely to be excited. Since the taper waist is multimode, there can multiple delineation curves depending on the choice of the higher-order mode which leads to a conundrum regarding the "correct" delineation curve. The asymmetric tapered fiber model and the beat length measurements for various taper profiles suggest that

i. The modes responsible for beating are HE_{11} and LP_{11} and hence the delineation curve which determines the adiabaticity of a taper transition is determined by the propagation constants of the HE_{11} and LP_{11} modes.

ii. The radii predicted by the asymmetric fiber model for the three different profiles were very close to the estimated radii from the beat length measurements.

The asymmetric tapered fibers of different taper profiles were used in dye absorption sensing experiments. The sensitivities they provided were compared to the sensitivities found using symmetric tapered fibers having the same waist radii, and the results were shown in Table 11.

5. 2. Future work

In this dissertation, we have demonstrated chemical (dye -SDC 2072) absorption sensing. The method can be extended to investigations involving other chemicals. Another possible direction that can be pursued is to detect gas absorption. Hollow bottle resonators along with an asymmetric tapered fiber can be used to detect near infrared active gases such as CO_2, CH_3, NH_3, CH_3Cl and so on. The detection limit can be further improved by means of lock-in amplification, phase sensitive detection, or by using quantum cascade lasers to excite the fundamental vibrational modes of the gases. Detecting the atmospheric concentrations of various gases can be extremely important for environmental monitoring.

In chapter II, the design of asymmetric tapered fibers and the adiabaticity criteria were discussed in detail based on the delineation curve defined by the difference in propagation constants of the HE_{11} and LP_{11} modes. For the three different taper profiles discussed in this dissertation, the taper angle versus inverse taper ratio plot for the non-adiabatic taper transition was well above the delineation curves defined by HE_{11} and LP_{11}. In fact, for the non-adiabatic taper transitions, the taper angle versus inverse taper ratio plot was well above the delineation curve defined by the difference in propagation constants of HE_{11} and HE_{12} mode and HE_{11} and HE_{41} mode. Ideally, for the non-adiabatic taper transition, we would like to have the taper angle versus inverse taper ratio plot to be just above the delineation curve defined by HE_{11} and LP_{11}, and below the delineation curves defined by HE_{11} and HE_{12}, and HE_{11} and HE_{41}. Even though the presence of modes other than LP_{11} may be only an extra intrinsic loss, we would like to eliminate those. Hence, in future, we would like to design a new asymmetric tapered fiber for which the taper angle versus inverse

taper ratio plot for the non-adiabatic taper transition is just above the delineation curve defined by HE_{11} and LP_{11}, and below the delineation curves defined by HE_{11} and HE_{12}, and HE_{11} and HE_{41} modes.

Cross polarization coupling in microresonators can lead to effects such as coupled-mode induced transparency or coupled-mode induced attenuation. These effects can produce slow or fast light i.e., pulse delay or advancement. Using an asymmetric tapered fiber instead of a symmetric tapered fiber may lead to enhanced delay or advancement. Hence a model will be developed to study the conditions for enhanced delay or advancement before being explored experimentally.

REFERENCES

[1] J. W. Strutt (Lord Rayleigh), *The Theory of Sound* (Dover, New York, 1945).

[2] P. Debye, “Der lichtdruck auf kugeln von beliebigem material,” Ann. Phys. **30**, 57–136, (1909).

[3] R. D. Richtmyer, "Dielectric Resonators," J. Appl. Phys. **10**, 391 (1939).

[4] C. G. Garrett, W. Kaiser, and W. L. Bond, "Stimulated emission into optical whispering modes of spheres," Phys. Rev. **1**, 1807-1809 (1961).

[5] V. B. Braginsky, M. L. Gorodetsky, and V. S. Ilchenko, “Quality factor and nonlinear properties of optical whispering-gallery modes,” Phys. Lett. A **137**, 393–397 (1989).

[6] K. D. Heylman, K. A. Knapper, E. H. Horak, M. T. Rea, S. K. Vanga, R. H. Goldsmith,” Optical microresonators for sensing and transduction: A materials perspective,” Adv. Mater. **29**, 1700037, (2017).

.

[7] J. M. Ward, N. Dhasmana, and S. Nic Chormaic, "Hollow core, whispering gallery resonator sensors," Eur. Phys. J. Special Topics **223**, 1917-1935 (2014).

[8] G. S. Murugan, M. N. Petrovich, Y. Jung, J. S. Wilkinson, and M. N. Zervas, "Hollow-bottle optical microresonators," Opt. Express **19**, 20773-20784 (2011).

[9] R.-I. Stoian, K. V. Bui, and A. T. Rosenberger, "Silica hollow bottle resonators for use as whispering gallery mode based chemical sensors," J. Opt. **17**, 125011 (2015).

[10] Y. Xu, P. Lu, L. Chen, and X. Bao, "Recent Developments in Micro-Structured Fiber Optic Sensors," Fibers **5**, 3, (2017).

[11] W. M. Henry and J. D. Love, "Spot size variation in non-adiabatic single mode fiber tapers," IEE Proc. **136**, 219-224 (1989).

[12] J. D. Love, W. M. Henry, W. J. Stewart, R. J. Black, S. Lacroix, and F. Gonthier, "Tapered single-mode fibres and devices Part 1: Adiabaticity criteria," IEE Proc.-J: Optoelectron. **138**, 343-354 (1991).

[13] R. J. Black, S. Lacroix, F. Gonthier, and J. D. Love, "Tapered single-mode fibers and devices Part 2: Experimental and theoretical quantification," IEE Proc.-J: Optoelectron. **138**, 355-364 (1991).

[14] T. A. Birks and Y. W. Li, "The Shape of Fiber Tapers," J. Lightwave Technol. **10**, 432-438 (1992).

[15] J. P. Rezac, *Properties and Applications of Whispering-Gallery Mode Resonances in Fused Silica Microspheres*, PhD Diss., Physics Dept., Oklahoma State University (2002).

[16] S. Fan, W. Suh, and J. D. Joannopoulos, “Temporal coupled-mode theory for the Fano resonance in optical resonators,” J. Opt. Soc. Am. A **20**, 569-572 (2003).

[17] A. Chiba, H. Fujiwara, J. Hotta, S. Takeuchi, and K. Sasaki, “Fano resonance in a multimode tapered fiber coupled with a microspherical cavity,” Appl. Phys. Lett. **86**, 261106 (2005).

[18] A. C. Ruege and R. M. Reano, “Multimode Waveguides Coupled to Single Mode Ring Resonators,” J. Lightwave Technol. **27**, 2035-2043 (2009).

[19] A. C. Ruege and R. M. Reano, “Multimode waveguide-cavity sensor based on fringe visibility detection,” Opt. Express **17**, 4295-4305 (2009).

[20] D. Ding, M. J. A. de Dood, J. F. Bauters, M. J. R. Heck, J. E. Bowers, and D. Bouwmeester, “Fano resonances in a multimode waveguide coupled to a high-Q silicon nitride ring resonator,” Opt. Express **22**, 6778-6790 (2014).

[21] K. Zhang, Y. Wang, and Y.-H. Wu, “Enhanced Fano resonance in a non-adiabatic tapered fiber coupled with a microresonator,” Opt. Express **42**, 2956-2959 (2017).

[22] L. Cai, J. Pan, Y. Zhao, J. Wang, and S. Xiao, “Whispering Gallery Mode Optical Microresonators: Structures and Sensing Applications,” Phys. Status Solidi A, **217**, 1900825, (2020).

[23] X. Jiang, A. J. Qavi, S. H. Huang, and L. Yang, “Whispering-Gallery Sensors,” Matter **3**, 371-392, (2020).

[24] M. R. Foreman, J. D. Swaim, and F. Vollmer, "Whispering gallery mode sensors," Adv. Opt. Photon. **7**, 168-240 (2015).

[25] N. M. Hanumegowda, C. J. Stica, B. C. Patel, I. White, and X. Fan, “Refractometric sensors based on microsphere resonators,” Appl. Phys. Lett. **87**, 201107 (2005).

[26] V. Zamora, A. Díez, M. V. Andrés, and B. Gimeno, "Refractometric sensor based on whispering-gallery modes of thin capillaries," Opt. Express **15**, 12011-12016 (2007).

[27] I. M. White, H. Oveys, and X. Fan, "Liquid-core optical ring-resonator sensors," Opt. Lett. **31**, 1319-1321 (2006).

[28] R.-I. Stoian, B. K. Lavine, and A.T. Rosenberger, “pH sensing using whispering gallery modes of a silica hollow bottle resonator,” Talanta. **194**, 585-590, (2019).

[29] A. M. Armani and K. J. Vahala, “Heavy water detection using ultra-high-Q microcavities,” Opt. Lett. **31**, 1896-1898 (2006)

[30] L. Shao, X.-F. Jiang, X.-C. Yu, B.-B. Li, W. R. Clements, F. Vollmer, W. Wang, Y.-F. Xiao, and Q. Gong, “Detection of single nanoparticles and lentiviruses using microcavity resonance broadening,” Adv. Mater. **25**, 5616 (2013).

[31] B.-Q. Shen, X.-C. Yu, Y. Zhi, L. Wang, D. Kim, Q. Gong, and Y.-F. Xiao, “Detection of single nanoparticles using the dissipative interaction in a high-Q microcavity,” Phys. Rev. Appl. **5**, 024011 (2016).

[32] G. Farca, S. I. Shopova, and A. T. Rosenberger, “Cavity-enhanced laser absorption spectroscopy using microresonator whispering-gallery modes,” Opt. Express **15**, 17443-17448 (2007).

[33] Y.-L. Chen, W.-L. Jin, Y.-F. Xiao, and X. Zhang,“Measuring the charge of a single dielectric nanoparticle using a high-Q optical microresonator,” Phys. Rev. Applied **6**, 044021, 2016.

[34] A. T. Rosenberger, “Analysis of whispering-gallery microcavity-enhanced chemical absorption sensors,” Opt. Express **15**, 12959-12964 (2007).

[35] N. Acharyya and G. Kozyreff, “Multiple critical couplings and sensing in a microresonator-waveguide system,” Phys. Rev. Appl. **8**, 034029, (2017).

[36] H. Ren, C. -L. Zou, J. Lu, L.-L. Xue, S. Guo, Y. Qin, and W. Hu, “Highly Sensitive Intensity Detection by a Self-Interference Micro-Ring Resonator,” IEEE Photonics Tech. Lett. **28**, 1469-1472 (2016).

[37] S. Wan, R. Niu, H. -L. Ren, C.-L. Zou, G.-C. Guo, and C.-H. Dong, “Experimental demonstration of dissipative sensing in a self-interference microring resonator,” Photon. Res. **6**, 681-685 (2018).

[38] H. Ren, C. -L. Zou, J. Lu, Z. Le, Y. Qin, S. Guo, and W. Hu, “Dissipative sensing with low detection limit in a self-interference microring resonator,” J. Opt. Soc. Am. B **36**, 942 (2019).

[39] M. Li, Y. Wang, X. Jiang, F. Bo, Y. Ruan, and Y. Tan, “Free-space self-interference microresonator with tunable coupling regimes,” Appl. Phys. Lett. **117**, 031106 (2020).

[40] A. T. Rosenberger, E. B. Dale, K. V. Bui, E. K. Gonzales, D. Ganta, L. Ke, and S. R. Rajagopal, "Cross-polarization coupling of whispering-gallery modes due to the spin–orbit interaction of light," Opt. Lett. **44**, 4163-4166 (2019).

[41] A. Yariv, *Optical Electronics in Modern Communications* (Oxford, New York, 1997).

[42] M. J. Humphrey, E. Dale, A. T. Rosenberger, and D. K. Bandy, “Calculation of optimal fiber radius and whispering gallery mode spectra for a fiber-coupled microsphere,” Opt. Commun. **271**, 124-131 (2007).

[43] S. W. Harun, K. S. Lim, C. K. Tio, K. Dimyati, and H. Ahmad, “Theoretical analysis and fabrication of tapered fibers,” Optik. **124**, 538-543 (2013).

[44] M. J. Humphrey, *Calculation of Coupling Between Tapered Fiber Modes and Whispering-Gallery Modes of a Spherical Microlaser*, PhD Diss., Physics Dept., Oklahoma State University (2004).

[45] C. Baker and M. Rochette, “A generalized heat-brush approach for precise control of the waist profile in fiber tapers,” Opt. Mater. Express **1**, 1065-1076 (2011).

[46] A. Felipe, G. Espindola, H. J. Kalinowski, J. A. S. Lima, and A. S. Paterno, “Stepwise fabrication of arbitrary fiber optic tapers,” Opt. Express **20**, 19893-19904 (2012).

[47] F. Orucevic, V. Lefèvre-Seguin, and J. Hare, “Transmittance and near-field characterization of sub-wavelength tapered optical fibers,” Opt. Express **15**, 13624-13629 (2007).

[48] M. C. Frawley, A. Petcu-Colan, V. G. Truong, and S. Nic Chormaic, “Higher order mode propagation in an optical nanofiber,” Opt. Commun. **285**, 4648–4654 (2012).

[49] S. Ravets, J. E. Hoffman, L. A. Orozco, S. L. Rolston, G. Beadie, and F. K. Fatemi, “A low-loss photonic silica nanofiber for higher-order modes,” Opt. Express **21**, 18325-18335 (2013).

[50] S. Ravets, J. E. Hoffman, P. R. Kordell, J. D. Wong-Campos, S. L. Rolston, and L. A. Orozco, “Intermodal energy transfer in a tapered optical fiber: optimizing transmission,” J. Opt. Soc. Am. A **30**, 2361-2371 (2013).

[51] Y.-H. Lai, K. Y. Yang, M.-G. Suh, and K. J. Vahala, “Fiber taper characterization by optical backscattering reflectometry,” Opt. Express **25**, 22312-22327 (2017).

[52] George Farca, *Cavity Enhanced evanescent wave chemical sensing using microresonators*, PhD dissertation, Oklahoma State University, 2006.

[53] P. Ghasemi and S. S.-H. Yam, "Analytical and experimental study on a bent abrupt taper," Opt. Express **29**, 82-94 (2021).

[54] M. I. Zibaii, H. Latifi, M. Karami, M. Gholami, S. M. Hosseini, and M. H.Ghezelayagh, "Non-adiabatic tapered optical fiber sensor for measuring the interaction between α-amino acids in aqueous carbohydrate solution," Meas. Sci. Technol. **21,** 105801 (2010).

[55] H. Latifi, M. I. Zibaii, S. M. Hosseini, and Jorge, P., "Nonadiabatic Tapered Optical Fiber for Biosensor Applications," Photonic Sensors **2**, 340–356 (2012).

[56] M. Z. Muhammad, A. A. Jasim, H. Ahmad, H. Arof, and S. W. Harun, "Non-adiabatic silica microfiber for strain and temperature sensors," Sensors and Actuators A **192**, 130-132 (2013).

[57] L. Luo, S. Pu, J. Tang, X. Zeng, and M. Lahoubi, "Reflective all-fiber magnetic field sensor based on microfiber and magnetic fluid," Opt. Express **23**, 18133-18142 (2015).

[58] A. T. Rosenberger and S. R. Rajagopal, "Enhanced dissipative sensing in a microresonator with multimode input (theory)," in *Optical, Opto-Atomic, and Entanglement-Enhanced Precision Metrology II*, Proc. SPIE **11296**, 112963D (2020).

[59] S. R. Rajagopal and A. T. Rosenberger, "Enhanced dissipative sensing in a microresonator with multimode input (experiment)," in *Optical, Opto-Atomic, and Entanglement-Enhanced Precision Metrology II*, Proc. SPIE **11296**, 112963Q (2020).

[60] S. B. Gorajoobi, G. S. Murugan, and M. N. Zervas, Efficient excitation and phase matching of fiber-coupled degenerate whispering gallery modes, J. Opt. Soc. Am. B **36**, 2452 (2019).

VITA

Sreekul Raj Rajagopal

Candidate for the Degree of

Doctor of Philosophy

Dissertation: MULTIMODE INPUT FOR ENHANCED DISSIPATIVE SENSING IN WHISPERING-GALLERY MICRORESONATORS.

Major Field: Photonics

Biographical:

Education:

Completed the requirements for the Doctor of Philosophy in Photonics at Oklahoma State University, Stillwater, Oklahoma in May, 2021.

Completed the requirements for the Master of Science in Physics at Oklahoma State University, Stillwater, Oklahoma in July, 2020.

Completed the requirements for the Bachelor of Science in Physics at Kannur University/ Mahatma Gandhi College, Kannur, Kerala, India May 2010.

Experience:
Microresonator optics.
Lasers and Spectroscopy

Professional Memberships:
Optical Society of America (student member)
SPIE (student member)